THE ROLE OF *FRIZZLED3* IN MOUSE NEURAL DEVELOPMENT

by

Zhong Hua

A dissertation submitted to The Johns Hopkins University in conformity with the requirements for the degree of Doctor of Philosophy

Baltimore, Maryland

May 2014

Abstract

The development of the nervous system requires the spatiotemporal specification of correct numbers and types of neurons and the establishment of precise synaptic connections between neurons and their targets. The latter aspect involves axon growth along stereotypic trajectories guided by extracellular cues. Recently it has been shown that targeted mutation of *Frizzled3* (*Fz3*) leads to axon guidance and growth defects in major fiber tracts in the rostral brain, including the anterior commissure, and the corticothalamic, thalamocortical, and nigrostriatal tracts, yet a systematic examination of the role of *Fz3* in the development of the nervous system has not been made. Here we took advantage of various immunohistochemical methods and found that *Fz3* is required for the development of multiple fiber tracts in the central nervous system and distinct cranial and spinal motor nerves in the periphery.

In the central nervous system, *Fz3* loss-of-function results in a nearly complete absence of three early axon tracts in the brain by embryonic day 11.5, axon guidance defects in catecholaminergic and serotonergic neurons in the brain, and pathfinding and central targeting defects in optic tract axons. Although development and target innervation of sensory neurons are largely unaffected in $Fz3^{-/-}$ mice, somatosensory information cannot be conveyed from the spinal cord to the brain due to loss of ascending spinal sensory fibers. In the periphery, loss of *Fz3* leads to axon growth defects in the VIIth and XIIth cranial motor nerves, the phrenic nerve, and dorsal motor nerves in the forelimb and hindlimb. As a secondary effect of axon growth defects, affected motor

neurons undergo apoptosis two days prior to the normal wave of developmental cell death. In the hindlimb, loss of *Fz3* results in abrupt stalling of the dorsal nerve at a precise location in the nerve plexus, which subsequently leads to complete atrophy of muscles within the anterior compartment of the lower limb. Overall, this study reveals a novel aspect of motor axon growth controlled by a central component of the planar cell polarity signaling pathway and represents a comprehensive examination of the role of *Fz3* in mouse neural development.

Readers:

Jeremy Nathans, MD, PhD (thesis advisor)

Professor of Molecular Biology and Genetics, Neuroscience, Ophthalmology

Johns Hopkins University School of Medicine

Shan Sockanathan, PhD (reader)

Associate Professor of Neuroscience

Johns Hopkins University School of Medicine

Acknowledgments

The past six years witnessed my growth in personal wisdom as well as scientific insights. The collegial environment of Hopkins has been tremendously supportive, and I have been helped by so many people that I cannot possibly name all of them here.

I owe my deepest gratitude to my advisor, Dr. Jeremy Nathans, for his continuous and generous support. He mentors students based on their own aptitude and personality. Since the first day I joined the lab, he has been extremely supportive and has given me the space and time to allow me to explore my own research interests and develop projects at my own pace. From his training, I learned how to conceive ideas, conduct experiments, and prepare manuscripts. From his strong dedication to science, I grasped the glamour of basic biomedical research. It has been a tremendous honor and privilege to work with and learn from him, a true scientist and a great mentor.

Special thanks to the members of my thesis committee, Drs. Alex Kolodkin, Shan Sockanathan, Michael Caterina, and Michael Deans, for their guidance on my research over the course of my study and for their expertise in axon guidance, motor neuron development, mouse behavior tests, and planar cell polarity signaling, which constitute the core of my research; again to Dr. Shan Sockanathan for reading this thesis and getting back to me promptly; to Dr. David Ginty for his advice on my projects and comments on my first manuscript; and to Drs. Duojia Pan and Geraldine Seydoux for giving me the opportunity to rotate in their labs, where the research broadened my horizons and the lab

members helped me adapt to the new environment here. I also want to thank the Biochemistry, Cellular and Molecular Biology graduate program, Dr. Carolyn Machamer, Sharon Root, Margie Policastri, Dr. Lesley Brown, Arhonda Gogos, Jessica Rexroad, and the Department of Molecular Biology and Genetics for making every transition smooth and pleasant.

I am extremely grateful to the wonderful current and former members of the Nathans Laboratory: Dr. Hao Wu demonstrates genuine leadership by helping others selflessly; Dr. Hao Chang possesses great scientific insights and a fabulous sense of humor; Dr. Yanshu Wang is truly a helping big sister to all of us; Phil Smallwood is a guru of making constructs and mice; John Williams is the lubricant to keep our lab running smoothly; Alisa Mo is the perfect combination of intelligence and self-motivation; Drs. Xin Ye, Tudor Badea, Huimin Yu, and Hugh Cahill helped me during my rotation and early phase in the lab; and Drs. Max Tischfield and Amir Rattner gave me valuable comments on my manuscripts. I would also like to thank Drs. Jiangyang Zhang, Sangmin Jeon, Siyi Huang, Ye Yan, Liang Han, and Lu Sun for advice and assistance.

I am forever indebted to my parents, sisters, and other family members. Everything would be impossible without their unconditioned encouragement, support, and love.

Table of Contents

List of Figures

Chapter I: Introduction

A. Axon growth and guidance

The ability of mammals to perceive, act, learn and memorize lies in the nervous system, which contains millions of neurons in a mouse and over a trillion in an adult human being. Mammalian nervous systems exhibit great complexity in the manner which information is relayed, integrated, and processed. At the cellular level, such complex yet accurate functions are achieved through the spatiotemporal differentiation of correct numbers and types of neurons followed by the establishment of precise synaptic connections between neurons and their targets. The latter aspect relies on the ability of axons to navigate along specific pathways to recognize their synaptic partners (Dickson, 2002).

Starting from the early 1990s, several gene families that control axon growth and guidance have been discovered. The advance in this field owes a great deal to invertebrate organisms, including the fruitfly *Drosophila melanogaster* and the nematode *Caenorhabditis elegans*, due to their relatively simple nervous systems – for example, *C. elegans* only has 302 neurons and the development of genetic screening and analysis techniques. Mutagenesis screens unearthed many genes essential for axon growth and guidance. For example, mutations in *Unc-6*, which encodes a secreted ligand in *C. elegans*, result in failure of the D neurons to extend away from the ventral nerve cord and the PDE and HSN neurons to extend to the ventral nerve cord. Unc-6 can function simultaneously as a chemoattractant and chemorepellent when perceived by its receptors

Unc-40 and Unc-5, respectively (Araujo and Tear, 2003; Hedgecock et al., 1990; Ishii et al., 1992).

More recent studies showed that several axon guidance mechanisms are highly conserved in all animals. For example, the ortholog of *Unc-6* in mouse is the *Netrin* family, which also exhibits similar roles in guiding spinal commissural axons and several forebrain commissures (Serafini et al., 1996). By far, the most well studied axon guidance mechanisms involve molecules that are conserved to a remarkable degree, including ephrins and Eph receptors, Netrins and their receptors, Semaphorins, and Slit proteins and their Robo receptors (Chisholm and Tessier-Lavigne, 1999). From these studies, a central theme regarding the molecular mechanisms underlying axon growth and guidance emerged. Receptors localized at neuronal growth cones can perceive attractive or repulsive cues, which are either diffusible or attached to cell surface. The activation of these receptors further engages downstream cytoskeletal regulation and eventually promotes growth cone extension or collapse (Bashaw and Klein, 2010).

B. Axon growth and guidance in the mouse brain and motor system

Study of axon growth and guidance has proven to be very challenging in mouse, which is the most extensively studied mammal and the nervous system of which represents a miniature of the human's, due to several reasons. First, single axon guidance molecules in *C. elegans* and *Drosophila* have multiple orthologs in mammals. For example, in contrast to the single Eph receptor in *C. elegans*, there are 14 Eph receptors in mammals. The presence of such gene families adds complexity in interpreting the role

of individual genes due to potential redundancy among their family members. Second, the mouse nervous system comprises millions of neurons of different types in various orders, which integrate multiple axon guidance mechanisms to navigate over long distances. Last but not least, the large size of the mouse nervous system also imposes technical challenges for unambiguously tracing individual axons.

The mammalian brain interprets the physical world and environmental stimuli and controls all aspects of bodily functions. During early embryonic stages, a few longitudinal tracts, including the tract of the postoptic commissure, the medial longitudinal fasciculus, and the descending root of the mesencephalic nucleus of the trigeminal nerve, form first and serve as the scaffold for later growing axons (Chedotal and Richards, 2010). During late embryonic development, the brain becomes wired in a complicated stereotypic manner by commissural and longitudinal fiber tracts connecting different contralateral and ipsilateral regions based on functional specificity. One of the most prominent axon guidance systems within the brain is the reciprocal connection between the cerebral cortex and the thalamus. Corticothalamic axons originating from cortical pyramidal neurons and thalamocortical axons originating from dorsal thalamic neurons have to cross several boundary zones, including the pallial-subpallial and the diencephalic-telencephalic boundaries, and be guided by guidepost cells and various cues to reach their final targets (Molnar et al., 2012). Multiple classic axon guidance molecules, including Netrin-1 and ephrin-A5, play critical roles in the development of thalamocortical axons, and loss-of-function mutations in multiple transcription factors also lead to abnormal thalamocortical projection (Lopez-Bendito and Molnar, 2003).

Motor neurons represent an attractive system to study axon growth and guidance, as their axons navigate through stereotypical pathways over long distances toward their targets in the periphery. The cell bodies of cranial motor neurons reside in the brainstem, and they extend axons through cranial nerves to control muscles involved in eye, neck and head movements, feeding, and facial expression. Cranial nerves, including motor and sensory nerves, are numbered from I^{st} to XII^{th} according to their anatomical location along the anterior-posterior body axis. The patterning and identity of cranial motor neurons are largely controlled by *Hox* genes. Cranial motor axons are guided by diffusible cues, and classic axon guidance molecules also play significant roles in this process. For example, *Netrin-1* and *Slit* are highly expressed in the brainstem floor plate and are suggested to act as repellents (Guthrie, 2007).

Motor neurons in the spinal cord comprise multiple pools, each of which is arranged in a longitudinal column along the rostrocaudal and ventrodorsal axes of the spinal cord and innervates distinct peripheral targets (Bonanomi and Pfaff, 2010). Motor neurons that innervate limbs are located within the lateral motor column (LMC), which is only present at brachial and lumbar levels and is further partitioned into lateral (LMC_L) and medial (LMC_M) divisions. LMC axons grow in tight fascicles extending to the plexus regions, where LMC_L motor neurons send their axons to the dorsal limb and LMC_M motor neurons innervate the ventral limb. Several signaling pathways have been discovered as players guiding motor axons to their peripheral targets, including Cxcl12:Cxcr4, GDNF:Ret, and epherin-A:EphA4 pathways (Kramer et al., 2006;

Lieberam et al., 2005). In the long navigation process to reach their distant targets, motor axons are continuously guided by multiple relaying signals. For example, initially ventral motor neurons (vMNs) require the Cxcl12:Cxcr4 signaling to extend axons through the ventral neural tube. Then medial motor column (MMC) neurons turn their axons dorsally toward axial muscles by repulsive epherin-A ligands in the dorsal root ganglia (DRG) and ventral mesenchyme and attractive fibroblast growth factors (FGFs) in the demomyotome, and hypaxial motor column (HMC) and LMC neurons continue to project ventrally to innervate body wall and limb muscles, respectively. Finally, LMC_L and LMC_M axons integrate a hierarchical signaling network mediated by Ret, GDNF, epherin-A, and EphA to segregate at the base of the limb (Bonanomi et al., 2012). At present, the identity of molecules underlying the distal branching of motor nerves and nerve-muscle recognition is largely unknown.

C. Planar cell polarity signaling

Wnt signaling has been extensively studied since the discovery of the first *Wnt* gene, mouse *Wnt1* in 1982 (Nusse and Varmus, 1992). The role of Wnt signaling has been implicated in many processes in development and disease (Logan and Nusse, 2004). The principal receptors for Wnt proteins have also been identified and are referred to as Frizzleds, which are seven-pass transmembrane proteins (Logan and Nusse, 2004; Wang et al., 1996).

Wnt-Frizzled interaction leads to several signaling cascades: the canonical or β-catenin pathway and the non-canonical pathways, which include the calcium pathway and

planar cell polarity (PCP) pathway. In the canonical Wnt pathway, Wnt proteins bind to Frizzled receptors and a co-receptor the low-density lipoprotein receptor-related protein (LRP-5/6), and then activated receptors transduce a signal to several intracellular proteins, including Dishevelled (Dvl), glycogen synthase kinase-3β (GSK-3β), Axin, and adenomatous polyposis coli (APC). Canonical Wnt signaling stabilizes β-catenin, which subsequently translocates to the nucleus and associates with transcription factors of the TCF/LEF family to activate target gene transcription. The non-canonical calcium pathway, which activates protein kinase C (PKC) and induces intracellular calcium mobilization and Ca^{2+}/calmodulin-dependent kinase (CaMK) I activation, came from research on early zebrafish development and mammalian cell culture.

PCP signaling was first discovered in *Drosophila* by Gubb and Garcia-Bellido based on their observation that a group of genes control the polarity of cuticular hairs and bristles (Gubb and Garcia-Bellido, 1982). These genes, including *Frizzled*, *Dishevelled*, *Van Gogh*/*strabismus*, *Prickle*, *Flamingo*/*starry night*, and *Diego*, are referred to as core PCP genes and are conserved from the fruitfly to all vertebrates. Targeted disruption of homologues for each *Drosophila* PCP gene in mice has revealed multiple developmental processes and anatomical structures that require PCP signaling for their correct orientations, including hair follicles and their associated structures, stereocilia on the apical faces of inner ear sensory hair cells, and motile cilia in the trachea (Chang and Nathans, 2013; Guo et al., 2004; Vladar et al., 2012; Wang et al., 2006a).

Core PCP genes encode either transmembrane or membrane-associated proteins.

In epithelia, where PCP has been most extensively studied, current evidence suggests that PCP proteins form asymmetric cell-surface complexes that organize the underlying cytoskeleton. Flamingo/Celsr proteins are present symmetrically on both proximal and distal sides of the cell and form homophilic adhesion, whereas Frizzled and Van Gogh proteins are exclusively localized at the distal and proximal side, respectively. The current view on PCP signaling is that the asymmetric localization of surface membrane complexes in a spatial context is required for the development of correct planar polarity.

D. The role of *Frizzled3* in the development of the mouse nervous system

Extensive evidence suggested that several Frizzled receptors in mice, including Frizzled3 (Fz3), and Fz6, function in the PCP signaling pathway (Goodrich and Strutt, 2011). Targeted loss-of-function in the mouse revealed that one of the ten *Frizzled* genes found in vertebrates, *Fz3*, plays a central role in several developmental events in the nervous system. *Fz3* is required for the development of several fiber tracts in the central nervous system (CNS), including the anterior commissure, the corpus callosum, the thalamocortical, corticothalamic, and nigrostriatal tracts, commissural sensory axons in the spinal cord, and monoaminergic axons in the brainstem (Fenstermaker et al., 2010; Lyuksyutova et al., 2003; Wang et al., 2002). *Fz3*$^{-/-}$ mice also exhibit defects in the development of sympathetic chain ganglia and sympathetic innervation of peripheral targets (Armstrong et al., 2011). In addition, *Fz3* also regulates caudal tangential migration of facial branchiomotor (FBM) neurons (Qu et al., 2010). In summary, previous studies demonstrated that *Fz3* controls axon guidance, target innervation, and neuronal migration in various contexts in the mouse nervous system.

E. Summary of experiments

Fz3 is widely expressed in the mouse CNS (Wang et al., 1996), therefore it is likely that *Fz3* is required for the development of neuronal populations other than those mentioned above. To test this hypothesis, we systematically examined $Fz3^{-/-}$ phenotypes in the mouse nervous system by adopting Neurofilament (NF) immunostaining of whole-mount tissues (i.e. embryos, limbs, and thick vibratome sections), developing alkaline phosphatase histochemistry strategies to label neurons and axons in a cell-type- or region-specific manner, and using the *Hb9-EGFP* transgene to visualize spinal motor nerves and a subset of cranial motor nerves. We further generated a conditional *Fz3* allele and ablated *Fz3* expression in a region-specific manner and in distinct neuronal populations by crossing to various *Cre* lines to address the requirement of *Fz3* expression in the development of relevant axon tracts and nerves. Finally we studied the functional consequence of $Fz3^{-/-}$ spinal cord phenotypes in adult mice.

Chapter II: Materials and Methods

A. Mouse lines

The conditional *Fz3* allele ($Fz3^{CKO}$) was generated by homologous recombination in mouse embryonic stem cells using standard techniques. The targeting construct contains the third exon of *Fz3* with 3.4 kb 5' and 6.4 kb 3' flanking sequences, and a HA epitope inserted to replace the linker region in this exon followed by the *neomycin phosphotransferase* selection marker with two flanking *frp* sites. *LoxP* sites were placed upstream of the third exon and downstream of the *neomycin phosphotransferase* expression cassette. The targeting construct was electroporated into R1 mouse embryonic stem cells, and colonies were grown in medium containing G418 and gancyclovir. Colonies were then picked and screened by Southern blot hybridization, and positive clones with a normal karyotype were injected into C57BL/6 blastocysts to generate chimeric founders. Germline transmission was later confirmed by Southern blot hybridization. Mice carrying the $Fz3^{CKO}$ allele were further crossed to germline Flippase mice to get rid of the *neomycin phosphotransferase* cassette (Rodriguez et al., 2000).

The following mouse lines were also used: $Bax^{-/-}$ (Knudson et al., 1995), $Brn3a^{CKOAP/CKOAP}$ (Badea et al., 2009a), $Brn3b^{CKOAP/CKOAP}$ (Badea et al., 2009a), *Cdx1-Cre* (Hierholzer and Kemler, 2009), $Fz3^{+/-}$ (Wang et al., 2002), $Fz3^{CKO/CKO}$ (Hua et al., 2013), *Calb2-IRES-Cre* (Taniguchi et al., 2011), *ChAT-IRES-Cre* (JAX #006410), *DAT1-Cre* (Zhuang et al., 2005), *Dbx1-IRES-Cre* (MMRRC #031751-MU), *Dlx5/6-Cre* (Stenman et al., 2003), *Emx1-IRES-Cre* (Gorski et al., 2002), *Foxg1-Cre* (Hebert and

McConnell, 2000), *Hb9-EGFP* (Wichterle et al., 2002), *Olig2-Cre* (Dessaud et al., 2007), *Pax6α-Cre* (Marquardt et al., 2001), *RORα-IRES-Cre* (Wu et al., 2010), *Rosa26iAP* (Badea et al., 2009b), *Sox2-Cre* (Hayashi and McMahon, 2002), and *Wnt1-Cre* (Danielian et al., 1998). Mice were handled and housed in accordance with the approved Institutional Animal Care and Use Committee guidelines of the Johns Hopkins Medical Institutions.

B. Alkaline phosphatase histochemistry

Throughout this work, the day of finding a copulation plug was counted as embryonic day 0.5 (E0.5), and the day when mice were born was counted as postnatal day 0 (P0). Alkaline phosphatase (AP) staining was performed on vibratome sections from (1) E18.5 heads: skinned heads were immersion fixed in 4% paraformaldehyde (PFA) [w/v, dissolved in phosphate buffered saline (PBS), pH 7.4] at 4°C overnight with gentle shaking, washed three times in PBS, and then decalcified in 50 mM ethylenediaminetetraacetic acid (EDTA), pH 7.0 at 4°C for one week; (2) E18.5 brains: brains were dissected out and immersion fixed in 4% PFA at 4°C overnight; and (3) E13.5 and E15.5 embryos: embryos were immersion fixed in 4% PFA at 4°C overnight. Samples were washed in PBS three times and embedded in 3% low melting point agarose (w/v, dissolved in PBS) and sectioned at 200 μm or 250 μm on a vibratome. AP histochemistry was performed essentially as previously described (Badea et al., 2003; Hua et al., 2013). Vibratome sections in PBS containing 2 mM $MgCl_2$ were heated in a water bath at 69°C for 90 minutes, and then equilibrated in AP staining buffer (0.1 M Tris, 0.1 M NaCl, 50 mM $MgCl_2$, pH 9.5) overnight at room temperature. AP

histochemistry was carried out in AP staining buffer containing 0.34 μg/ml 4-nitro blue tetrazolium chloride (NBT) and 0.175 μg/ml 5-bromo-4-chloro-3-indolyl-phosphate (BCIP) (Roche Applied Science; Indianapolis, IN), for 1 hour to overnight at room temperature with gentle horizontal shaking. Before imaging, sections were dehydrated through an ethanol series and cleared with BBBA [2:1 benzyl benzoate (BB)/benzyl alcohol (BA)] (Sigma-Aldrich; St. Louis, MO).

C. Immunohistochemistry

The following primary antibodies were used: rabbit anti-Brn3a (MAB1585; Millipore; Billerica, MA), rabbit anti-Calbindin D28k (CB38; Swant; Marly 1, Switzerland), rabbit anti-Calretinin (7699/4; Swant), rabbit anti-cleaved Caspase3 (9661; Cell Signaling Technology; Danvers, MA), goat anti-Choline acetyltransferase (ChAT) (AB144P; Millipore), rabbit anti-Ebf1 (a gift from Dr. Randell Reed; Johns Hopkins University School of Medicine, Baltimore, MD), rabbit anti-Foxp1 (ab16645; Abcam; Cambridge, England), mouse anti-Glutamic acid decarboxylase [GAD-6; Developmental Studies Hybridoma Bank (DSHB); Iowa City, IA], rabbit anti-Glial fibrillary acidic protein (GFAP) (RB-087-A; Thermo Scientific; Waltham, MA), rabbit anti-Green fluorescent protein (GFP) (A11122; Invitrogen; Grand Island, NY), mouse anti-Islet1 (39.3F7; DSHB), mouse anti-Islet1/2 (39.4D5; DSHB), mouse anti-Neurofilament (165 kDa, NF) (2H3; DSHB), rabbit anti-human Placental alkaline phosphatase (hPLAP) (AHP537; AbD Serotec; Raleigh, NC), rabbit anti-Serotonin (20080; Immunostar; Hudson, WI), goat anti-Sox10 (SC-17342; Santa Cruz Biotechnology; Dallas, TX), and rabbit anti-Tyrosine hydroxylase (TH) (AB152; Millipore). Alexa Fluor 647 α-

Bungarotoxin (B35450; Invitrogen) was used to label acetylcholine receptors. Secondary antibodies were Alexa Fluor 488, 594, or 647 conjugated, donkey anti-goat, goat anti-mouse, or goat anti-rabbit IgG antibodies (Invitrogen).

Immunostaining was performed on (1) 14 μm-thick vertical retina cryosections: the eye was enucleated from a mouse and immersion fixed in 4% PFA for 30 minutes at 4^0C, and then cornea and lens were carefully removed. The remaining eye cup was immersion fixed in 4% PFA at 4°C overnight, washed three times in PBS, equilibrated in 30% sucrose (w/v, dissolved in PBS), embedded in Optimal Cutting Temperature (OCT) compound (Sakura Finetek; Torrance, CA), frozen, and sectioned at 14 μm on a cryostat; (2) 14 μm-thick spinal cord cryosections: embryos were immersion fixed in 4% PFA at 4^0C for 1 hour, washed three times in PBS, equilibrated in 30% sucrose, embedded in OCT compound, frozen, and sectioned at 14 μm on a cryostat; (3) 120 μm-thick vibratome sections: embryos and brains were immersion fixed in 4% PFA at 4°C overnight, washed three times in PBS, embedded in 3% low melting point agarose, and sectioned at 120 μm on a vibratome; and (4) whole-mount E11.5 embryos, E12.5 heads, and E13.5 limbs: samples were immersion fixed in 4% PFA at 4°C for 2 hours and washed three times in PBS.

For immunostaining of 14 μm-thick cryosections and 120 μm-thick vibratome sections, sections were blocked in blocking solution [PBS containing 0.3% Triton X-100 and 5% normal goat serum (NGS) or normal donkey serum (NDS)] at room temperature for 1 hour, and incubated with primary antibody in blocking solution at 4°C overnight.

Sections were then washed five times in PBST (PBS containing 0.3% Triton X-100), and incubated with secondary antibody in blocking solution at room temperature for 1 hour (cryosections) or at 4°C overnight (vibratome sections). Finally sections were washed five times in PBST and mounted with Fluoromount-G (Southern Biotech; Birmingham, AL).

For immunostaining of whole-mount embryos, heads, and limbs, samples were first incubated in Dent's Bleach [10% H_2O_2, 13.3% dimethyl sulfoxide (DMSO), 53.3% methanol] at 4°C for 24 hours, washed with methanol five times, and fixed in Dent's Fix (20% DMSO, 80% methanol) at 4°C overnight. Samples were washed in PBS three times, incubated with primary antibody in blocking solution (20% DMSO, 75% PBST, 5% NGS, 0.025% sodium azide) at room temperature for 5 days to one week with gentle end-over-end rotation, and then washed five times in PBST. Samples were incubated with secondary antibody in blocking solution at room temperature for 2 days with gentle end-over-end rotation and then washed five times in PBST. Finally samples were dehydrated in 50% methanol/PBS and then 100% methanol, and cleared in BBBA.

D. Microscopy and image analysis

Samples processed for AP histochemistry were imaged using a Zeiss Stemi V11 microscope with a color Axiocam CCD in combination with Openlab software. Immunostained samples were imaged using a Zeiss LSM700 confocal microscope with Zen software. Images of whole-mounts were acquired with a 10× air objective at 10 μm intervals in the *Z* dimension, and the entire *Z* stack was either collapsed using maximum

intensity projection or color-coded based on *Z*-dimension depth. BBBA-cleared embryos and heads were positioned in custom-built metal holders consisted of a shallow triangular trough (sides: 2 cm × 2 cm × 1 cm; and depths: 1, 2, 3, or 4 mm). The trough was filled with BBBA and coverslipped during imaging.

E. Magnetic resonance imaging of mouse limbs

P70 *Cdx1-Cre;Fz3*$^{CKO/-}$ mice and control littermates were fixed by cardial perfusion. Then hindlimbs were harvested for magnetic resonance imaging (MRI), which was performed essentially as previously described (Zhang et al., 2008).

F. Two-texture and two-temperature preference assays

Experiments were conducted as previous described (Huang et al., 2011). A rectangular plexiglass chamber with a floor consisting of four thermally isolated aluminum blocks (for two-temperature preference assay, in this study, 32^{0}C and 38^{0}C) or four thin aluminum blocks (for two-texture preference assay, each glued with a piece of sandpaper, in this study, 60 grain vs. 400 grain) was positioned in the center of a rectangular frame containing infrared sensors. Each diagonally opposed block pair was maintained at the same temperature or glued with the same type of sandpaper. The configuration of temperature or texture assignment to the blocks was reversed every 2 to 3 mice. The infrared sensors were hooked up together and then to the computer, and the software OptoMax collected data from the sensors. Mouse whiskers were trimmed off before two-texture preference assay. Mice were acclimated in a plexiglass cylinder for 1

hour before test and the occupancy of each block during a 1-hour test period was collected for analysis.

G. Quantification of motor neurons, measurement of nerve diameter, and statistical analysis

The number of motor neurons on each cryosection was manually quantified in ImageJ. To measure the diameter of limb motor nerves, a line perpendicular to and fully cross the nerve at designated sites was drawn in Adobe Illustrator and the length of this line was then measured. Statistical comparisons were performed in either GraphPad Prism 5 or Microsoft Excel.

Chapter III: Role of *Fz3* in the Mouse Central Nervous System

A. Multiple fiber tracts in the brain are disrupted by loss of *Fz3*

In light of previous demonstration that *Fz3* is required for axon guidance of major fiber tracts in the mouse forebrain, including the anterior commissure, and the corticothalamic, thalamocortical, and nigrostriatal tracts (Wang et al., 2002), we asked whether *Fz3* plays similar roles in the development of other fiber tracts in the mouse CNS. As $Fz3^{-/-}$ mice die shortly after birth, we first performed NF immunostaining on consecutive E18.5 brain sections aiming to maximally capture axonal development defects as a result of *Fz3* loss-of-function in the brain.

As shown in Figure 1, NF immunostaining reveals a complete absence of the anterior commissure and a nearly complete loss of fibers in the cortical intermediate zone and the striatum in the $Fz3^{-/-}$ brain. In the mutant striatum, aberrant fibers circle around the globus pallidus (Figure 1A-B'). In the $Fz3^{-/-}$ brain, cholinergic axons in the basal forebrain form aberrant tracts surrounding the globus pallidus (Hua et al., 2013). Therefore at least a portion of the aberrant fibers seen here are cholinergic axons. In addition, NF immunostaining also shows some aberrant fibers within the external capsule, which appear to have originated from cortical neurons and are not present in wildtype (*WT*, including $Fz3^{+/+}$ and $Fz3^{+/-}$) brains (Figure 1B and B').

In the $Fz3^{-/-}$ thalamus, instead of entering the internal capsule and eventually the cerebral cortex, the majority of thalamocortical axons descend ventrally, and some

thalamocortical axons ascend dorsally toward the superior colliculus (SC). Some of the descending axons form a U-shaped axonal tract along with their counterparts from the contralateral thalamus, and the rest of them turn laterally and enter the cortical marginal zone (Figure 1C-D'). To unambiguously trace thalamocortical axons, we generated *WT* and *Fz3*$^{-/-}$ embryos carrying a *RORα-IRES-Cre* knock-in allele and a Cre-controlled alkaline phosphatase (AP) reporter, *R26iAP* (Badea et al., 2009b; Wu et al., 2010). In prenatal mouse brain *RORα* is expressed in the dorsal thalamus (Nakagawa and O'Leary, 2003), and activation of the human placental alkaline phosphatase (hPLAP) by the *RORα-IRES-Cre* robustly labels thalamocortical fibers. AP staining on *RORα-IRES-Cre;R26iAP;Fz3*$^{+/-}$ and *RORα-IRES-Cre;R26iAP;Fz3*$^{-/-}$ brain sections fully confirms guidance defects of thalamocortical axons as demonstrated by NF immunostaining (Figure 1H-N').

NF immunostaining also shows that in the *Fz3*$^{-/-}$ brain the corticospinal tract is diminutive, the medial lemniscus and the mammillothalamic tract are nearly completely absent, and the fasciculus retroflexus is poorly fasciculated (Figure 1E and E'). In addition, the organization of axon bundles in the reticular formation is disrupted upon *Fz3* knockout. Many longitudinal fibers in the mutant hindbrain, instead of forming a well-organized matrix as seen in *WT* mice, are reduced in caliber and arranged erratically (Figure 1F-G').

Figure 1. Multiple fiber tracts in the brain are affected by loss of *Fz3*

(A-G') NF immunostaining of E18.5 coronal brain sections showing defects in major fiber tracts in the *Fz3*$^{-/-}$ brain (arrows vs. arrowheads), including the absence of the anterior commissure (B and B'); mis-routing of thalamocortical axons (C-D'), nearly complete absence of the corticospinal tract, the medial lemniscus, and the mammillothalamic tract; and poor fasciculation of the fasciculus retroflexus (E and E'). G and G' are enlarged view of boxed regions in F and F', respectively. GP, globus pallidus. Scale bars: E', 1 mm; G', 200 μm.

(H-N') Thalamocortical axons are labelled by AP staining of consecutive coronal sections from E18.5 *RORα-IRES-Cre;R26iAP;Fz3*$^{+/-}$ and *RORα-IRES-Cre;R26iAP;Fz3*$^{-/-}$ brains. In the *Fz3*$^{-/-}$ brain, most thalamocortical axons descend ventrally and then either course through midline forming U-shaped fiber tracts or project laterally entering the cortical marginal zone. Scale bar, 1 mm.

(O and P) Planes of sections in A-N'.

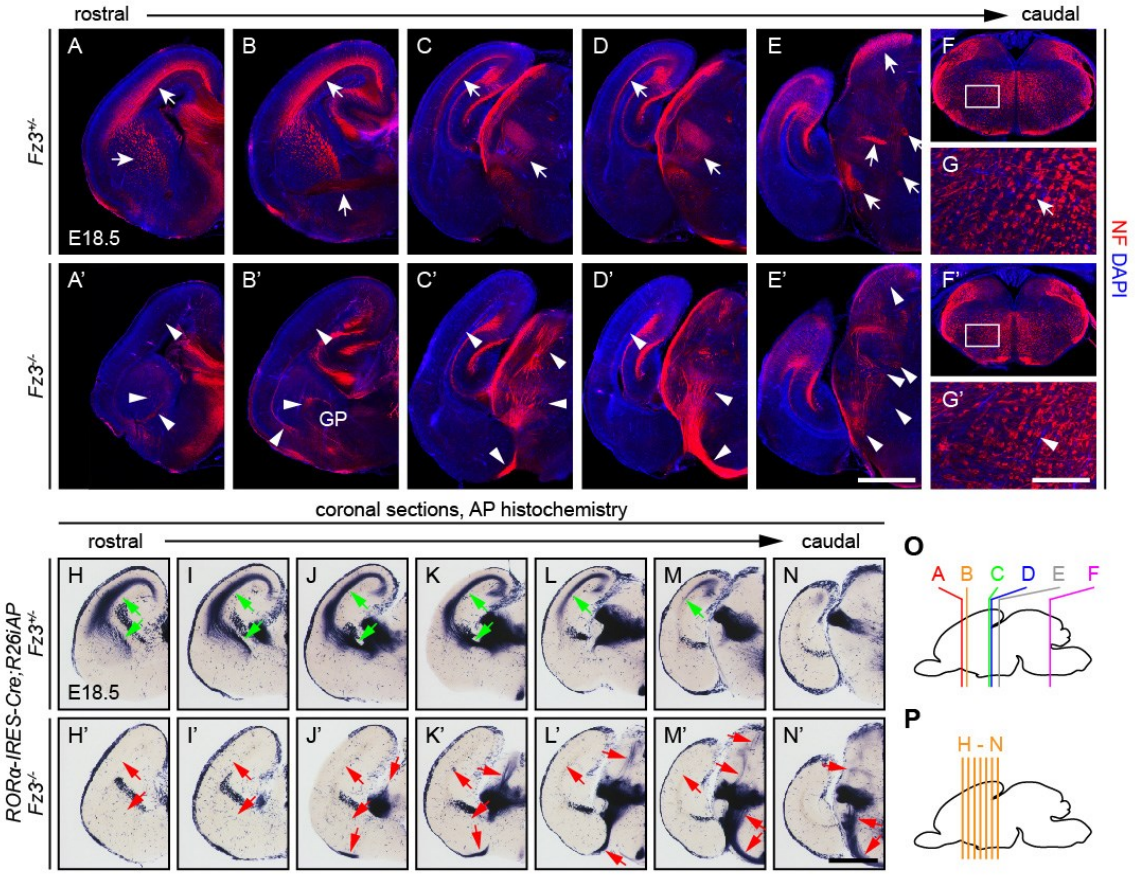
rostral
caudal
A
B
C
D
E
F
G
E18.5
A'
B'
C'
D'
E'
F'
G'
GP
Fz3+/-
Fz3-/-
NF DAPI
coronal sections, AP histochemistry
rostral
caudal
H
I
J
K
L
M
N
H'
I'
J'
K'
L'
M'
N'
E18.5
RORα-IRES-Cre;R26iAP
Fz3+/-
Fz3-/-
O
A B C D E F
P
H - N

B. *Fz3* expression is required in ventral telencephalic neurons for the development of the corticothalamic, corticospinal, and thalamocortical axons

Major fiber tracts in the mouse brain, including those affected by loss of *Fz3*, grow over long distances and pass through multiple regions via guidance by extracellular molecules, guidepost cells, and pre-existing fibers (Chedotal and Richards, 2010). *Fz3* is widely expressed in the developing mouse brain and is essential for the development of multiple fiber tracts (Wang et al., 2002), yet it remains elusive how Fz3 functions to control axon guidance and growth. As a first step to probe this question, we asked whether *Fz3* expression is required autonomously in cortical pyramidal neurons and thalamic neurons for the development of the anterior commissure, and the corticothalamic, corticospinal, and thalamocortical tracts. We therefore generated a conditional *Fz3* allele [$Fz3^{CKO}$; Hua et al. (2013)], and used several *Cre* lines to inactivate *Fz3* in specific brain regions by generating $Cre;Fz3^{CKO/-}$ mice from crossing $Cre;Fz3^{+/-}$ males with $Fz3^{CKO/CKO}$ females.

When *Fz3* is inactivated in the telencephalon by the *Foxg1-Cre* (Hebert and McConnell, 2000), the $Foxg1\text{-}Cre;Fz3^{CKO/-}$ mouse appears to exhibit the complete spectrum of axonal development defects seen in the $Fz3^{-/-}$ forebrain (Figure 2B-B''). Consistent with this finding is that, when *Fz3* is depleted in the dorsal thalamus by *RORα-IRES-Cre* or in the midbrain and hindbrain by *Dbx1-IRES-Cre* (NIH Neuroscience Blueprint Cre Driver Network, 2009; Wu et al., 2010), axon tracts affected in the $Fz3^{-/-}$ brain appear intact (Figure 2E-F''). These results suggest that *Fz3* expression is required in the telencephalon – essentially the cerebral cortex and the striatum – for the

development of the anterior commissure, and the corticothalamic, corticospinal, and thalamocortical tracts.

When *Fz3* expression is ablated in the cerebral cortex by *Emx1-IRES-Cre*, which expresses the Cre recombinase specifically in the cerebral cortex (Gorski et al., 2002), the posterior anterior commissure is completely missing and abberant fibers appear within the external capsule (Figure 2C-C''). Given that other fiber tracts appear completely normal in the *Emx1-IRES-Cre;Fz3*$^{CKO/-}$ brain, it is very likely that axons destined to form the posterior anterior commissure have pathfinding defects and eventually appear as these abberant fibers within the external capsule (Figure 2C'). Together, these observations indicate that *Fz3* signaling is autonomously required in temporal cortical neurons to form the posterior part of the anterior commissure, and in contrast, *Fz3* is not autonomously required in cortical and thalamic neurons for the development of the corticothalamic, corticospinal, and thalamocortical tracts.

The above results suggest that *Fz3* expression in striatal neurons might be critical for corticothalamic, corticospinal, and thalamocortical axon tracts. We then tested this possibility by taking advantage of the *Dlx5/6-Cre* transgene to eliminate *Fz3* in the ventral telencephalon (Stenman et al., 2003). In *Dlx5/6-Cre;Fz3*$^{CKO/-}$ brains, the corticothalamic, corticospinal, and thalamocortical tracts show defects to various extents, with the most severe exhibiting a complete disconnection between the cerebral cortex and the thalamus (Figure 3A and B). In most cases, *Dlx5/6-Cre;Fz3*$^{CKO/-}$ brains show partial defects – abberant axons surround the globus pallidus, axon bundles appear within the

internal capsule, a portion of thalamocortical axons descend ventrally, and the corticospinal tract is diminutive (Figure 2D-D''). *Dlx5/6-Cre;Fz3*$^{CKO/-}$ mice are able to survive to adulthood and are signicantly smaller than their littermates (data not shown). In the adult *Dlx5/6-Cre;Fz3*$^{CKO/-}$ brain, lateral ventricles are markedly enlarged, and in the striatum axon fibers are closely bundled together and massive astrocytes are activated (Figure 2C-D'). Given that cell proliferation and differentiation are normal in the *Fz3*$^{-/-}$ forebrain and the *Fz3*$^{-/-}$ striatum exhibits increased cell death at E18.5 (Wang et al., 2002), it is likely that striatal neurons continue to die in postnatal *Dlx5/6-Cre;Fz3*$^{CKO/-}$ mice. Taken together, results from various *Cre;Fz3*$^{CKO/-}$ mice indicate that *Fz3* expression in Dlx5/6^{+} ventral telencephalic neurons is required for the development of the corticothalamic, corticospinal, and thalamocortical tracts.

It has been shown that corridor cells, a neuronal population derived from the lateral ganglionic eminence (LGE), migrate tangentially to the medial ganglionic eminence (MGE) to form a permissive bridge for the growth of thalamocortical axons (Lopez-Bendito et al., 2006). The location of corridor cells in the striatum intrigued a question in the context of *Fz3* – whether *Fz3* loss-of-function affects this neuronal population. By immunostaining to detect the expression of Ebf1 – a transcription factor marker for corridor cells, we found that in the *Fz3*$^{-/-}$ brain corridor cells are generated and are able to migrate from LGE to MGE (Figure 3E-F''). Interestingly, while in the *WT* brain the medioventral edge of the globus pallidus is devoid of corridor cells, the globus pallidus is fully encircled by Ebf1^{+} cells in the *Fz3*$^{-/-}$ brain (Figure 3E' and F'). However, it is not known whether the presence of Ebf1^{+} cells in the medioventral edge of the

globus pallidus is a causal factor or a secondary effect or unrelated to the mis-rounting thalamocortical axons in the *Fz3*$^{-/-}$ brain.

Figure 2. Development of major fiber tracts in brains with region-specific inactivation of *Fz3*

(A-F'') NF immunostaining of E18.5 coronal sections from brains with *Fz3* inactivated in the entire forebrain (*Foxg1-Cre*, B-B''), in the cerebral cortex (*Emx1-IRES-Cre*, C-C''), in the ventral telencephalon (*Dlx5/6-Cre*, D-D''), in the midbrain and hindbrain (*Dbx1-IRES-Cre*, E-E''), and in the dorsal thalamus (*RORα-IRES-Cre*, F-F''). Panels A-F showing the anterior commissure and panels A'-F'' showing thalamocortical axons. Scale bar, 1 mm.

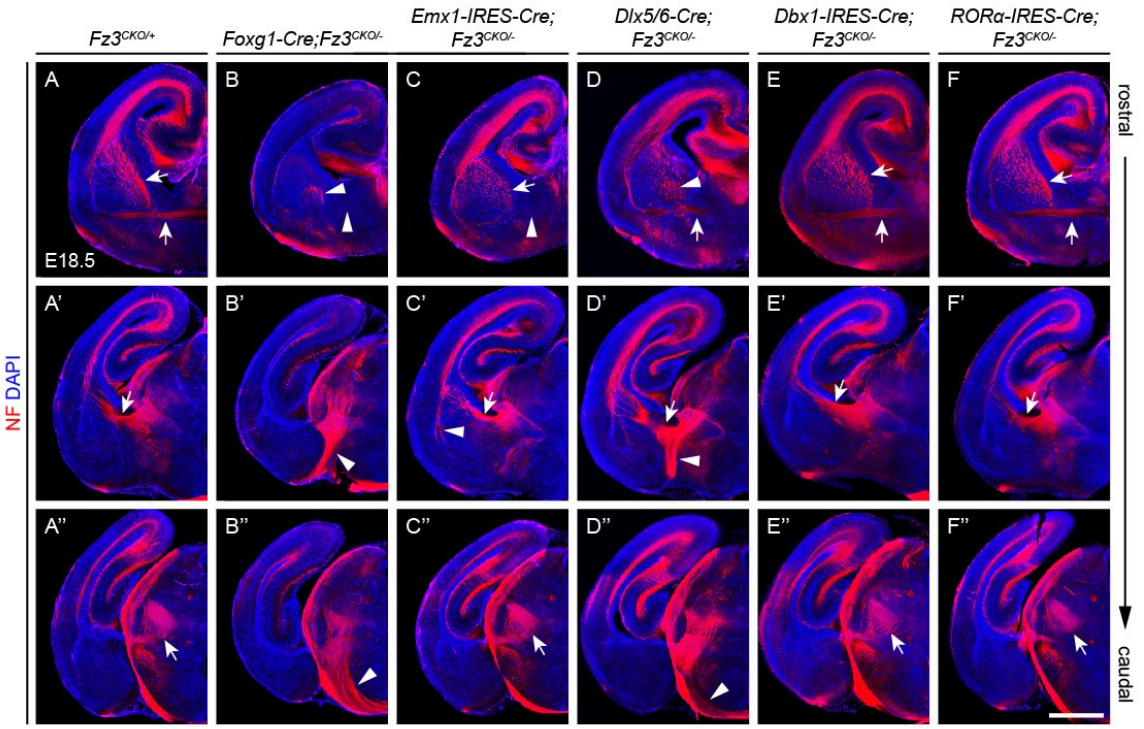

Figure 3. Defects in embryonic and adult *Dlx5/6-Cre;Fz3*$^{CKO/-}$ brains and the effect of *Fz3* loss-of-function on corridor cells

(A and B) In one E13.5 *Dlx5/6-Cre;Fz3*$^{CKO/-}$ brain, the cerebral cortex and the thalamus are completely disconnected (arrow vs. arrowhead) – representing the most severe phenotype seen in *Dlx5/6-Cre;Fz3*$^{CKO/-}$ brains. Scale bar, 500 μm.

(C-D') NF and GFAP co-immunostaining of P16 coronal brain sections showing enlarged lateral ventricle (arrowhead in D), and closely bundled axons (right arrowhead in D') and activated astrocytes (left arrowhead in D') in the striatum, in the *Dlx5/6-Cre;Fz3*$^{CKO/-}$ brain. Dashed lines delineate the edge of half brains (C and D), continuous white line encircles the lateral ventricle (D), and C' and D' are magnified view of boxed regions in C and D, respectively. Scale bars: D, 1 mm; D', 500 μm.

(E-F'') NF and Ebf1 co-immunostaining of E13.5 brain sections showing that Ebf1^{+} corridor cells fully encircle the globus pallidus in the *Fz3*$^{-/-}$ brain (arrow vs. arrowhead in E' and F'). Scale bar, 500 μm.

(G and H) Planes of sections in A, B, E, and F.

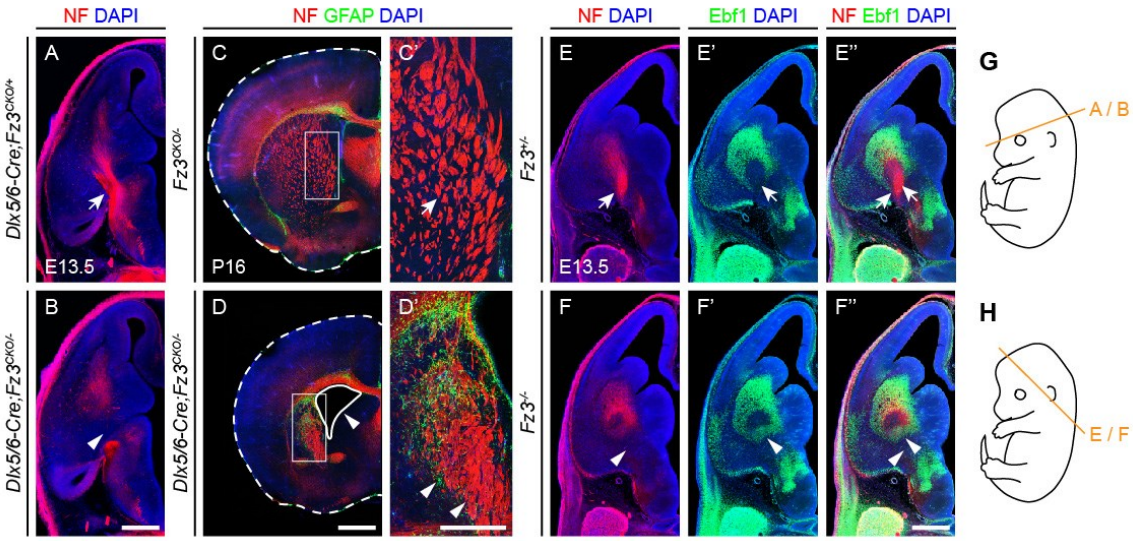

C. *Fz3* is required for the development of early axon tracts in the mouse brain

In all vertebrate species, the first axon tracts are developed in a stereotyped spatiotemporal pattern and serve as scaffolds for later growing axons (Chedotal and Richards, 2010). In light of the essential role of *Fz3* in axonal development in various contexts, we asked whether *Fz3* plays any role in the development of early axon tracts. To address this question while circumventing any inconvenience in tracing axons through serial sections and avoiding potential artifacts caused by sectioning, we first performed NF immunostaining on whole-mount E12.5 heads. Although fiber tracts in the brain are not strongly labelled as peripheral nerves, they could be clearly identified along the entire trajectory and by the relative position within the brain. In the $Fz3^{-/-}$ brain, three major fiber tracts are arrested, greatly reduced in intensity, or absent. In addition, the ventral branch of the trigeminal V3 nerve is either markedly thinned or completely missing in $Fz3^{-/-}$ embryos (Figure 4A and A').

To further understand the identities of these fiber tracts, we then performed Calretinin or Calbindin – two calcium-binding proteins expressed in early embryonic mouse CNS (Jacobowitz and Abbott, 1998) – and NF co-immunostaining on E11.5-E13.5 brain sections. NF and Calretinin co-immunostaining on E11.5 brain sections shows that generation and distribution of $Calretinin^{+}$ neurons are largely normal in the $Fz3^{-/-}$ brain (Figure 4E-I' and 5A-L'). However, the $Calretinin^{+}$ fiber tract in the thalamic eminence is completely missing in the $Fz3^{-/-}$ midbrain (Abbott and Jacobowitz, 1999) (Figure 4E-G' and 5A-D'). This result is further confirmed by AP histochemistry on the *Calb2-IRES-Cre;R26iAP;*$Fz3^{-/-}$ brain, in which the recombination at the *R26iAP* locus by *Calb2-*

IRES-Cre leads to sufficient accumulation of the AP protein for clear visualization of Calretinin^{+} neurons and axons at E13.5 (Figure 6A-F'). Later by E13.5 Calretinin^{+} thalamocortical axons fail to enter the internal capsule in the *Fz3*$^{-/-}$ brain (Figure 4I and I'), consistent with previous descriptions (Figure 1). In addition, the medial forebrain bundle projecting rostrally from the midbrain to the basal forebrain is diminutive upon loss of *Fz3* (Figure 4E-G' and 5E-L').

NF and Calbindin co-immunostaining on E12.5 brain sections does not reveal any abnormality in the generation and distribution pattern of Calbindin^{+} neurons in the *Fz3*$^{-/-}$ brain (Figure 4J-R'). In addition to the defects described above in E11.5 brains, this immunostaining also shows that in the *Fz3*$^{-/-}$ brain a major fiber tract originated from the brainstem fails to project rostrally toward the midbrain (Figure 4P-R'). Taken together, these data demonstrate that *Fz3* is essential for the development of early axon tracts in the mouse brain.

Figure 4. Early axon tracts are disrupted in the *Fz3*$^{-/-}$ brain

(A and A') NF immunostaining of whole-mount E12.5 heads showing complete absence of three fiber tracts in the brain (top three arrows vs. arrowheads) and the ventral branch of the trigeminal V3 nerve (lower arrows vs. arrowhead) in *Fz3*$^{-/-}$ embryos. The red to blue color code represents depth within the *Z*-stack, oriented bilaterally here from the top side to the bottom side. Scale bar, 500 μm.

(B-D) Diagrams showing planes of sections in E-R' (top) and comparing axon tracts in *WT* (drawn in black) and *Fz3*$^{-/-}$ brains (drawn in grey) (bottom). Green dot in B and green arrow in D represent the Calretinin^{+} fiber tract in the thalamic eminence; blue arrows in B and D represent the medial forebrain bundle; the red arrow in D represents ascending fiber tracts from the brainstem; and the orange arrow in C represents Calretinin^{+} thalamocortical axons. Dot in grey and dashed arrows in grey indicate that the fiber tract is missing in the *Fz3*$^{-/-}$ brain.

(E-H') NF and Calretinin co-immunostaining of consecutive E11.5 brain sections showing absence of the Calretinin^{+} fiber tract in the thalamic eminence (top arrows vs. arrowheads in E-G') and the diminutive medial forebrain bundle (lower arrows vs. arrowheads in E-H') in the *Fz3*$^{-/-}$ brain. Scale bar, 500 μm.

(I and I') Early Calretinin^{+} thalamocortical axons fail to enter the internal capsule in the *Fz3*$^{-/-}$ brain (arrow vs. arrowhead), revealed by Calretinin immunostaining of coronal brain sections at E13.5. Scale bar, 500 μm.

(J-R') NF and Calbindin co-immunostaining of E12.5 brain sections showing that in the *Fz3*$^{-/-}$ brain distribution of Calbindin^{+} neurons is normal, the fiber tract in the thalamic eminence is absent (top arrows vs. arrowheads in K-M'), the medial forebrain bundle is

diminutive (lower arrows vs. arrowheads in J-M'), and fiber tracts in the brainstem fail to ascend to the midbrain (arrows vs. arrowheads in P-R'). Scale bar, 500 μm.

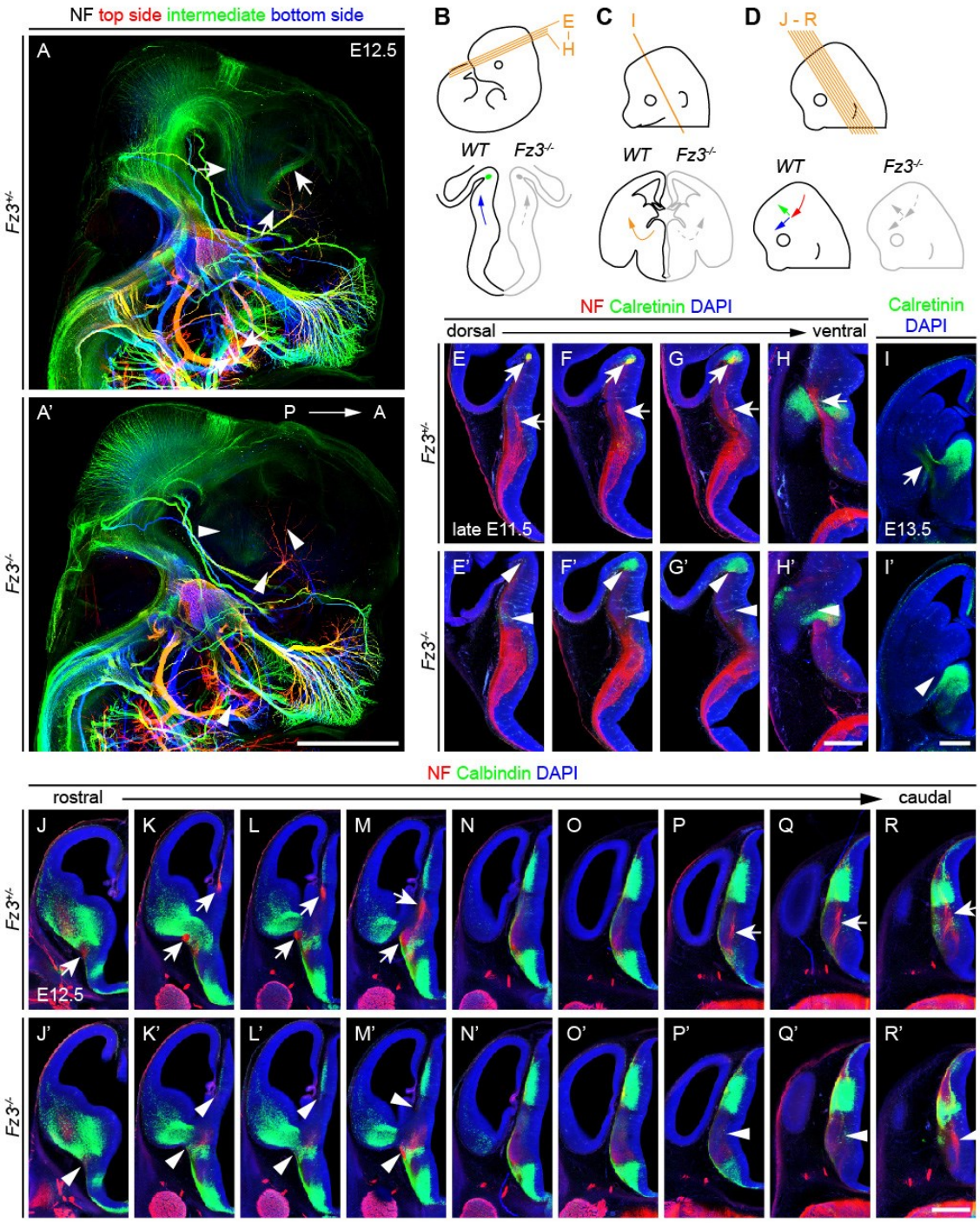

Figure 5. Calretinin^{+} fiber tract in the thalamic eminence and the medial forebrain bundle are missing in the *Fz3*$^{-/-}$ brain

(A-D') NF and Calretinin co-immunostaining of consecutive E11.5 brain sections showing the absence of the Calretinin^{+} fiber tract in the *Fz3*$^{-/-}$ midbrain (arrows vs. arrowheads). Scale bar, 500 μm.

(E-L') The medial forebrain bundle in the *Fz3*$^{-/-}$ brain is diminutive (arrows vs. arrowheads), revealed by NF and Calretinin co-immunostaining of consecutive E11.5 brain sections. E'-L' are enlarged view of boxed regions in E-L. Scale bars: L, 500 μm; L', 250 μm.

(M and N) Planes of sections in A-L (left) and summarizing defects seen in the *Fz3*$^{-/-}$ brain (right).

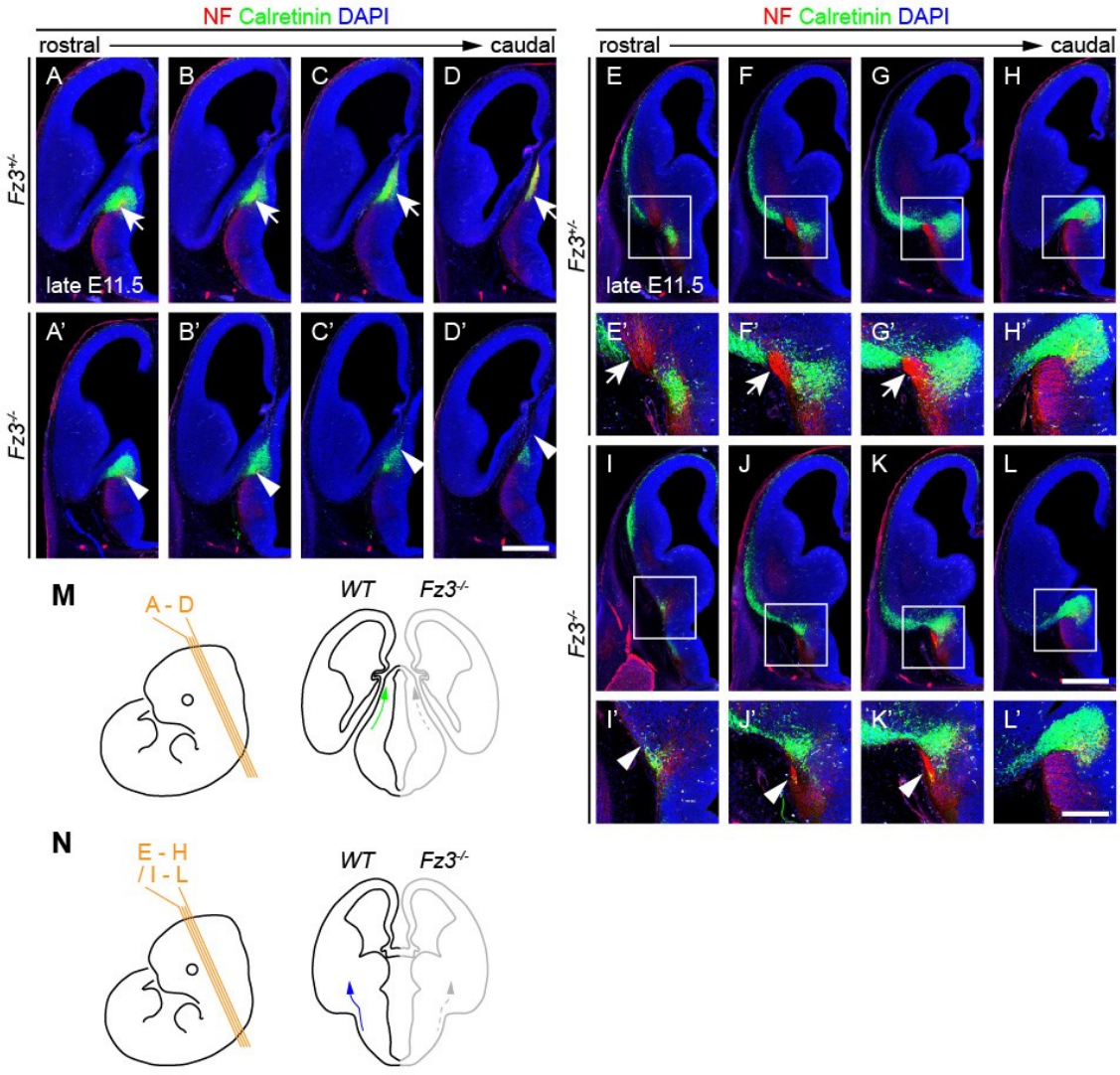
NF Calretinin DAPI
rostral
caudal
A
B
C
D
late E11.5
A'
B'
C'
D'
Fz3+/-
Fz3-/-
NF Calretinin DAPI
rostral
caudal
E
F
G
H
late E11.5
E'
F'
G'
H'
I
J
K
L
I'
J'
K'
L'
Fz3+/-
Fz3-/-
M
A - D
WT
Fz3-/-
N
E - H
/ I - L
WT
Fz3-/-

Figure 6. Loss of Calretinin^{+} fiber tract in the thalamic eminence in the *Fz3*$^{-/-}$ brain revealed by AP histochemistry

(A-F') Recombination of the *R26iAP* reporter by *Calb2-IRES-Cre* followed by AP histochemistry strongly labels Calretinin^{+} cell bodies and axons in E13.5 brains and shows the absence of the Calretinin^{+} fiber tract in the thalamic eminence in the *Fz3*$^{-/-}$ brain (green vs. red arrows). Scale bar, 1 mm.

(G) Planes of sections in A-F' (left) and depicting the loss of the Calretinin^{+} fiber tract in the *Fz3*$^{-/-}$ brain (right).

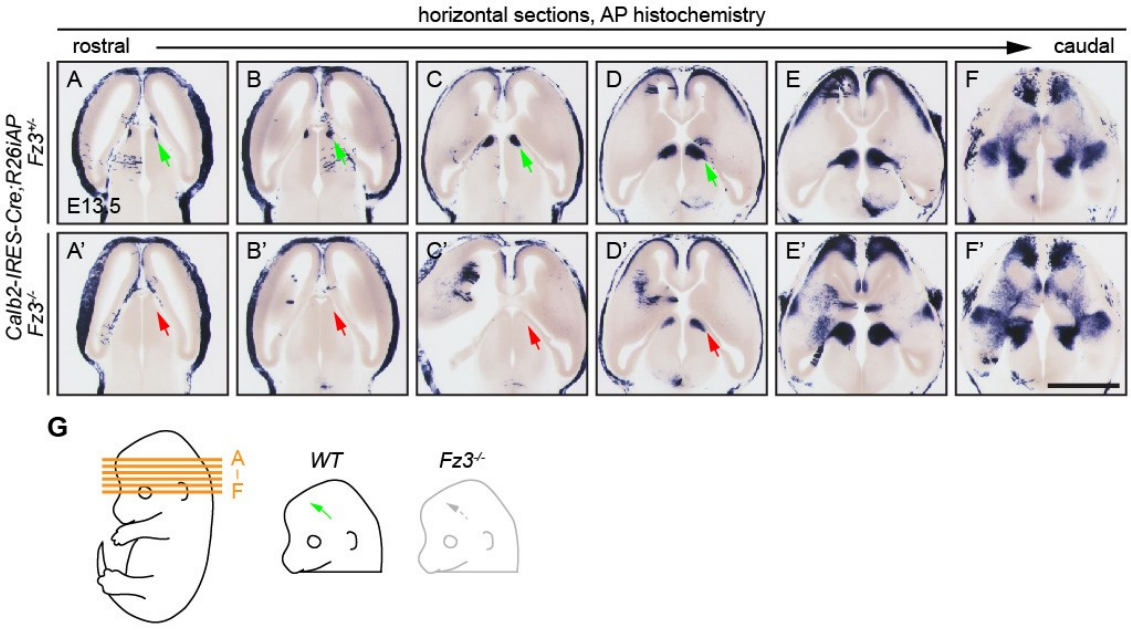

D. *Fz3* knockout results in defects in axon pathfinding and central projection of retinal ganglion cells

Fz3 is expressed in the mouse retina (Wang et al., 2002), yet it is not known whether *Fz3* plays any role in the development of the retina. Given the well-established role of *Fz3* in axon guidance and growth (Hua et al., 2013; Wang et al., 2002; Wang et al., 2006b), we focused on the optic tract – axons originated from retina ganglion cells (RGCs). We took advantage of the $Brn3b^{CKOAP}$ mouse, in which a hPLAP expression cassette is inserted immediately downstream of the 3' of the Brn3b coding region and is expressed upon Cre-mediated recombination (Badea et al., 2009a), and visualized the axonal projection of *Brn3b*-expressing RGCs by crossing $Brn3b^{CKOAP}$ and the retina-specific *Pax6α-Cre* transgene to *WT* and $Fz3^{-/-}$ mice (Marquardt et al., 2001).

The major optic tract innervates diverse central targets that are essential for visual perception, including the lateral geniculate nucleus (LGN), the olivary pretectal nucleus (OPN), the pretectal area (PA), and the SC, while the inferior fasciculus of the accessory optic tract diverges from the major optic tract at the optic chiasm and innervates the medial terminal nucleus (MTN). Careful examination of consecutive head sections revealed that the overall projection of *Pax6α-Cre;*$Brn3b^{CKOAP/+}$*;*$Fz3^{-/-}$ RGC axons from the retina to the optic chiasm is intact (data not shown). However, at the optic chiasm a portion of these axons abnormally diverge from the major optic tract and enter the dorsal thalamus instead of proceeding to their central targets (Figures 7A-D'). In addition, in $Fz3^{-/-}$ mice the inferior fasciculus of the accessory optic tract is absent and the MTN is not innervated (Figure 7E and E').

In the *Fz3*$^{-/-}$ brain, mis-routed thalamocortical axons form a U-shaped fiber bundle that courses adjacent to the optic tract along the ventral and lateral edge of the thalamus (Wang et al., 2006a). The close anatomical localization of the mis-routed thalamocortical axons and the optic tract axons in *Fz3*$^{-/-}$ brains raised the possibility that these tracts might inappropriately co-fasciculate with each other. To assess this possibility, we performed AP and NF co-immunostaining on coronal sections from *Pax6α-Cre;Brn3b*$^{CKOAP/+}$*;Fz3*$^{+/-}$ and *Pax6α-Cre;Brn3b*$^{CKOAP/+}$*;Fz3*$^{-/-}$ brains, in which AP decorates RGC fibers and NF labels all axons. As shown in Figures 7L-N, some RGC axons in the *Pax6α-Cre;Brn3b*$^{CKOAP/+}$*;Fz3*$^{-/-}$ brain indeed fasciculate with descending thalamocortical axons in the thalamus.

The above observations suggest that *Fz3* plays an important role in the pathfinding and central targeting of the optic tract. One obvious question that stemmed from these results was whether defective pathfinding and targeting of *Fz3*$^{-/-}$ RGC axons reflect autonomous requirement of Fz3 function in RGCs. To probe this question, we generated *Pax6α-Cre;Brn3b*$^{CKOAP/+}$*;Fz3*$^{CKO/-}$ embryos in which *Fz3* is only depleted in AP-labelled RGCs and fiber tracts in the brain are unaffected. In these mice, the major optic tract does not show any pathfinding defect, suggesting that in the *Fz3*$^{-/-}$ brain mis-routed thalamocortical axons guide the navigation of a small portion of RGC axons by co-fasciculating with them (Figure 7F-K'). On the contrary, the inferior fasciculus of the accessory optic tract is diminutive, indicating that *Fz3* is autonomously required in this RGC population for the axons to branch from the major optic tract and innervate the

MTN. In sum, the above data show differential requirement of Fz3 signaling in the pathfinding and central targeting of RGC axons.

We next asked whether *Fz3* is involved in retinal lamination, which represents one of the major neural circuitry organizations in the vertebrate retina. We collected retinas from adult *Six3-Cre;Fz3*$^{CKO/-}$ mice and performed immunostainings with primary antibodies detecting specific cell types on vertical retina sections. *Six3-Cre* was used because this transgene expresses *Cre* recombinase widely in the retina at very early stage (Furuta et al., 2000) and *Six3-Cre;Fz3*$^{CKO/-}$ mice are viable into adulthood. As shown in Figure 8, GABAergic amacrine cells, dopaminergic amacrine cells, cholinergic amacrine cells, Calbindin^{+} cells, and Calretinin^{+} cells stratify within the correct lamina in both *Six3-Cre;Fz3*$^{CKO/-}$ and *WT* littermate control retinas. These results demonstrate that Fz3 signaling is not involved in inner retinal neurite arborization.

Figure 7. Pathfinding and central targeting defects in *Fz3*$^{-/-}$ RGC axons

(A-E') RGC axons are labelled by AP histochemistry – *hPLAP* is expressed in RGCs at the *Brn3b* locus after recombination mediated by the *Pax6α*-driven Cre recombinase. In the *Fz3*$^{-/-}$ brain, a portion of RGC axons diverge from the major optic tract and enter the thalamus (red arrows in A'-D'), and the MTN is not innervated (black vs. red arrows in E and E'). Scale bar, 500 μm.

(F-K') RGCs with *Fz3* inactivation are selectively labelled by AP histochemistry. In *Pax6α-Cre;Brn3b*$^{CKOAP/+}$*;Fz3*$^{CKO/-}$ mice, central targeting of RGCs is normal, yet the inferior fasciculus of the accessory optic tract is diminutive (green vs. red arrows in I-K'). Scale bar, 1 mm.

(L-N) NF and AP co-immunostaining of coronal sections from the *Pax6α-Cre;Brn3b*$^{CKOAP/+}$*;Fz3*$^{-/-}$ brain showing that mis-routed RGC axons (AP^+/NF^+) co-fasciculate with ventrally descending thalamocortical axons (NF^+/AP^-) (arrowheads in N). N is enlarged view of the boxed region in M''. Scale bars: M'', 200 μm; N, 100 μm.

(O) Planes of sections in A-K'.

(P) Diagram showing the location of sections in L and M. Green arrow represents the major optic tract innervating central targets in *WT* mice, and red arrow shows the mis-routed RGC axons in the *Fz3*$^{-/-}$ brain.

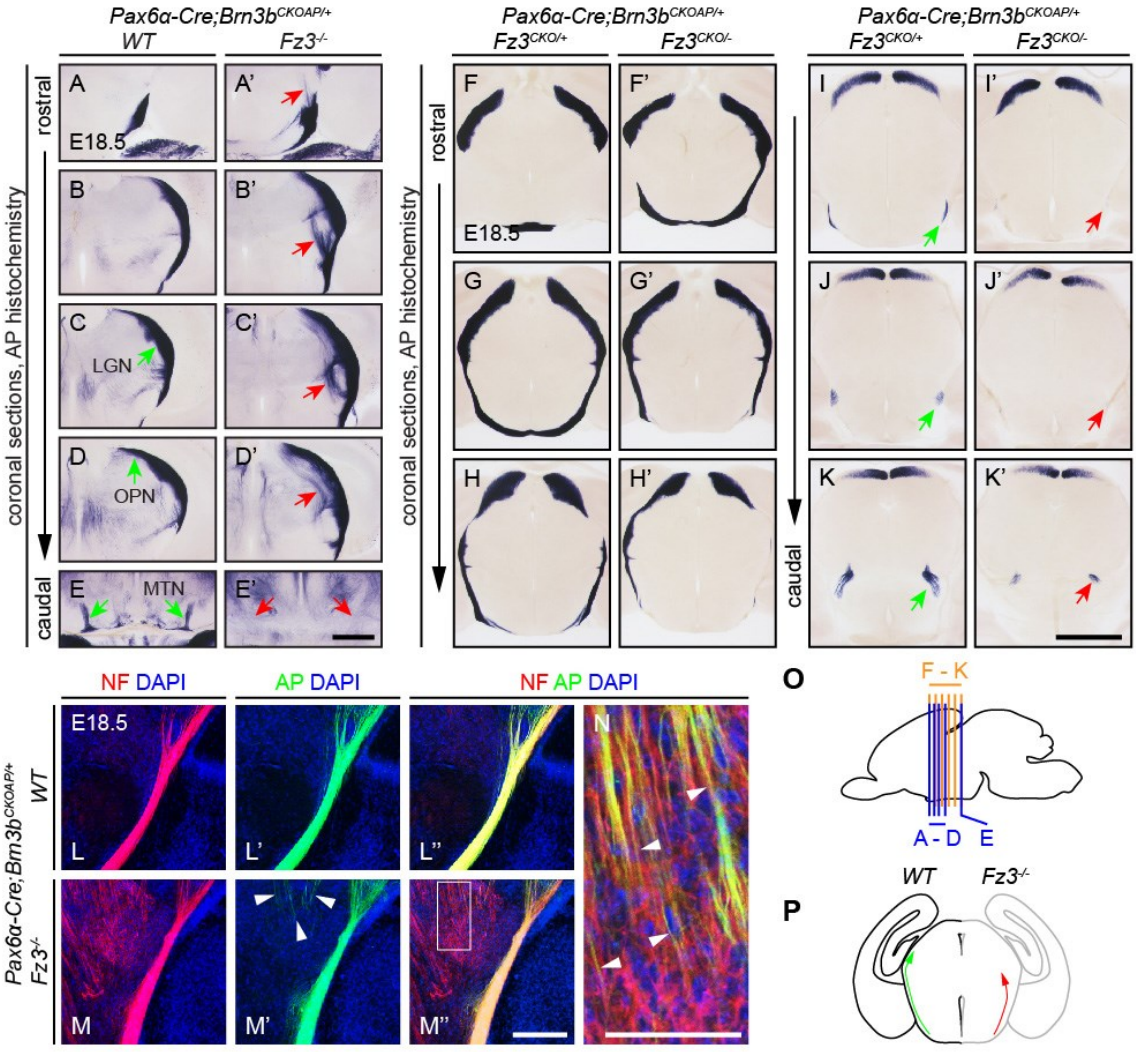
Pax6α-Cre;Brn3b^CKOAP/+
WT
Fz3-/-
Fz3^CKO/+
Fz3^CKO/-
rostral
caudal
coronal sections, AP histochemistry
A
A'
B
B'
C
C'
D
D'
E
E'
E18.5
LGN
OPN
MTN
F
F'
G
G'
H
H'
I
I'
J
J'
K
K'
NF DAPI
AP DAPI
NF AP DAPI
L
L'
L''
M
M'
M''
N
O
F - K
A - D
E
P
WT
Fz3-/-

Figure 8. Normal inner retinal neurite arborization in the *Six3-Cre;Fz3*$^{CKO/-}$ retina

(A-E') Calbindin^{+} cells (A and A'), Calretinin^{+} cells (B and B'), cholinergic amacrine cells (C and C'), GABAergic amacrine cells (D and D'), and dopaminergic amacrine cells (E and E') stratify within the correct lamina in the retina with *Fz3* inactivated by the *Six3-Cre* transgene. Scale bar, 50 μm.

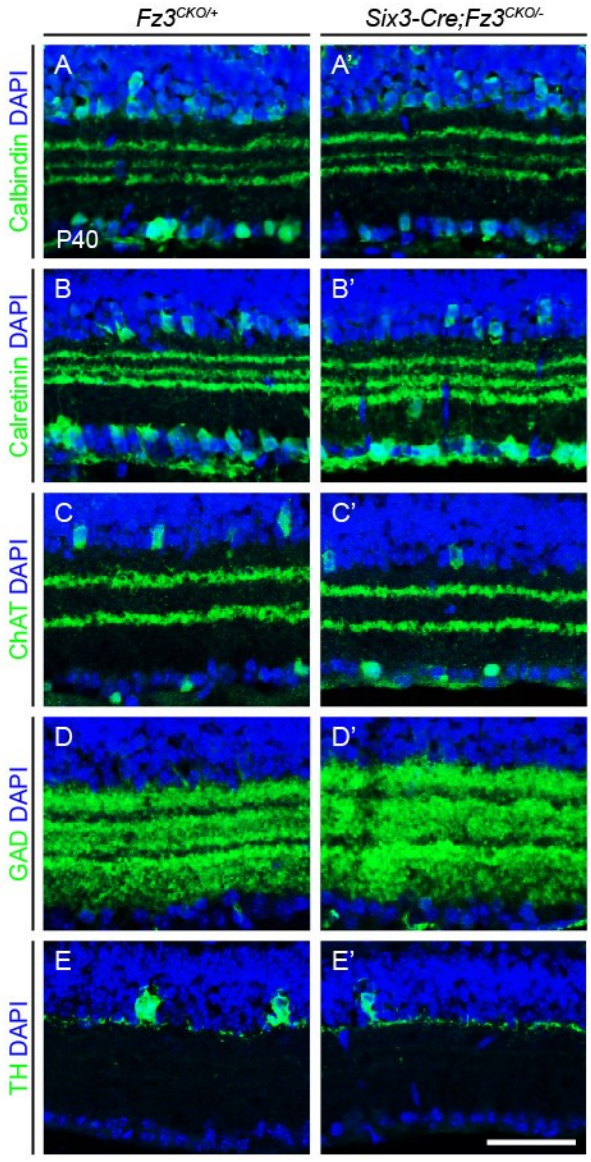

E. Axon guidance of neurons comprising major modulatory systems in the midbrain and brainstem is disrupted by loss of *Fz3*

The reticular formation is composed of systems of neurons that are essential for sensory awareness, motor responses, and arousal to behavioral state transition. These neuronal systems – referred to as "modulatory systems of the brain" – are characterized by their long projections ascending to the forebrain or descending to the spinal cord and are categorized by the kind of neurotransmitters they secrete. Major modulatory systems include noradrenergic, adrenergic, dopaminergic, cholinergic, serotonergic, and histaminergic cells and they all project axons to the forebrain (Kandel et al., 2000). In light of the result that dopaminergic neurons fail to innervate the striatum by E18 in $Fz3^{-/-}$ brains (Wang et al., 2002), we asked whether loss of *Fz3* affects axon guidance of other modulatory neurons.

Since Choline acetyltransferase (ChAT) immunostaining proved inefficient on prenatal brain sections, we adopted the AP histochemistry strategy – generating *WT* and $Fz3^{-/-}$ embryos carrying *ChAT-IRES-Cre* and *R26iAP* alleles – to study cholinergic projections (Hua et al., 2013). The activation of the hPLAP by the *ChAT-IRES-Cre* specifically labels cholinergic neurons in the basal forebrain and cranial and spinal motor neurons at E18.5 (Figure 16, 17 and 18). Yet this method only faintly labels cholinergic cell bodies in the laterodorsal and pedunculopontine tegmental nuclei, and axons from these neurons could not be traced (Figure 17I). In addition, immunostaining with a histamine antibody only worked on adult brain sections but not on prenatal brain sections. The low accumulation of histamine as well as ChAT has prevented an in-depth analysis

of whether histaminergic and cholinergic projections in the brainstem are disrupted in *Fz3*$^{-/-}$ embryos.

Immunostaining detecting Tyrosine hydroxylase (TH), which is the first enzyme in the reaction chain for the synthesis of dopamine, norepinephrine, and epinephrine – neurotransmitters synthesized by dopaminergic, adrenergic and noradrenergic neurons, shows that TH^{+} axons in the midbrain have reached the basal forebrain by E13.5 and are readily detectable in the striatum at E18.5 in *WT* brains. In contrast, in the *Fz3*$^{-/-}$ brain these TH^{+} axons fail to innervate the forebrain by E13.5 and form tight fasciculi descending to the spinal cord by E18.5 (Figure 9A-O'). Further AP staining on brain sections from *DAT1-Cre;R26iAP;Fz3*$^{-/-}$ embryos, in which the recombination of the *R26iAP* allele by *DAT1-Cre* – a Cre knock-in at the dopamine transporter locus (Zhuang et al., 2005), shows that the striatum is devoid of AP histochemical reactivity and the majority of dopaminergic axons form tight fiber tracts descending to the spinal cord (Figure 9P-Q' and 10). Similarly, Serotonin (5-hydroxytryptamine, 5-HT) immunostaining shows that serotonergic axons in the brainstem fail to ascend to the basal forebrain by E13.5 and instead descend to the spinal cord by E18.5 in *Fz3*$^{-/-}$ embryos (Figure 11). In sum, these results demonstrate that *Fz3* loss-of-function impairs axon guidance of dopaminergic, adrenergic, noradrenergic, and serotonergic neurons in the brain.

Figure 9. TH^+ axons in the midbrain form tight fasciculi descending to the spinal cord and fail to innervate the forebrain in *Fz3*$^{-/-}$ embryos

(A-K) In the *Fz3*$^{-/-}$ brain TH^+ axons fail to ascend to the basal forebrain (white vs. red arrows), while generation of this neuronal population is not affected (arrowheads), revealed by TH immunostaining of consecutive E13.5 brain sections. K, diagrams showing planes of sections in A-J' (top) and innervation defect of TH^+ neurons in the *Fz3*$^{-/-}$ midbrain (middle and bottom). Scale bar, 1 mm.

(L-O') NF and TH co-immunostaining of E18.5 sagittal brain sections showing that in the *Fz3*$^{-/-}$ brain the striatum is devoid of TH^+ axons (green arrows in M vs. M'), the majority of TH^+ axons in the substantia nigra descend to the spinal cord (red arrows in O') instead of projecting rostrally (green vs. red arrows in N and N'). M-O' are enlarged view of boxed regions in L and L'. M-O' show only the anti-TH signal, with the intensity inverted. Background staining is seen in the vasculature. Scale bars: L', 1 mm; O', 500 μm.

(P-Q') In the *DAT1-Cre;R26iAP;Fz3*$^{-/-}$ brain, dopaminergic axons labelled by AP histochemistry fail to innervate the striatum (green vs. red arrows in P and P') and form tight fasciculi descending to the spinal cord (two red arrows at right in Q'). Scale bar, 1 mm.

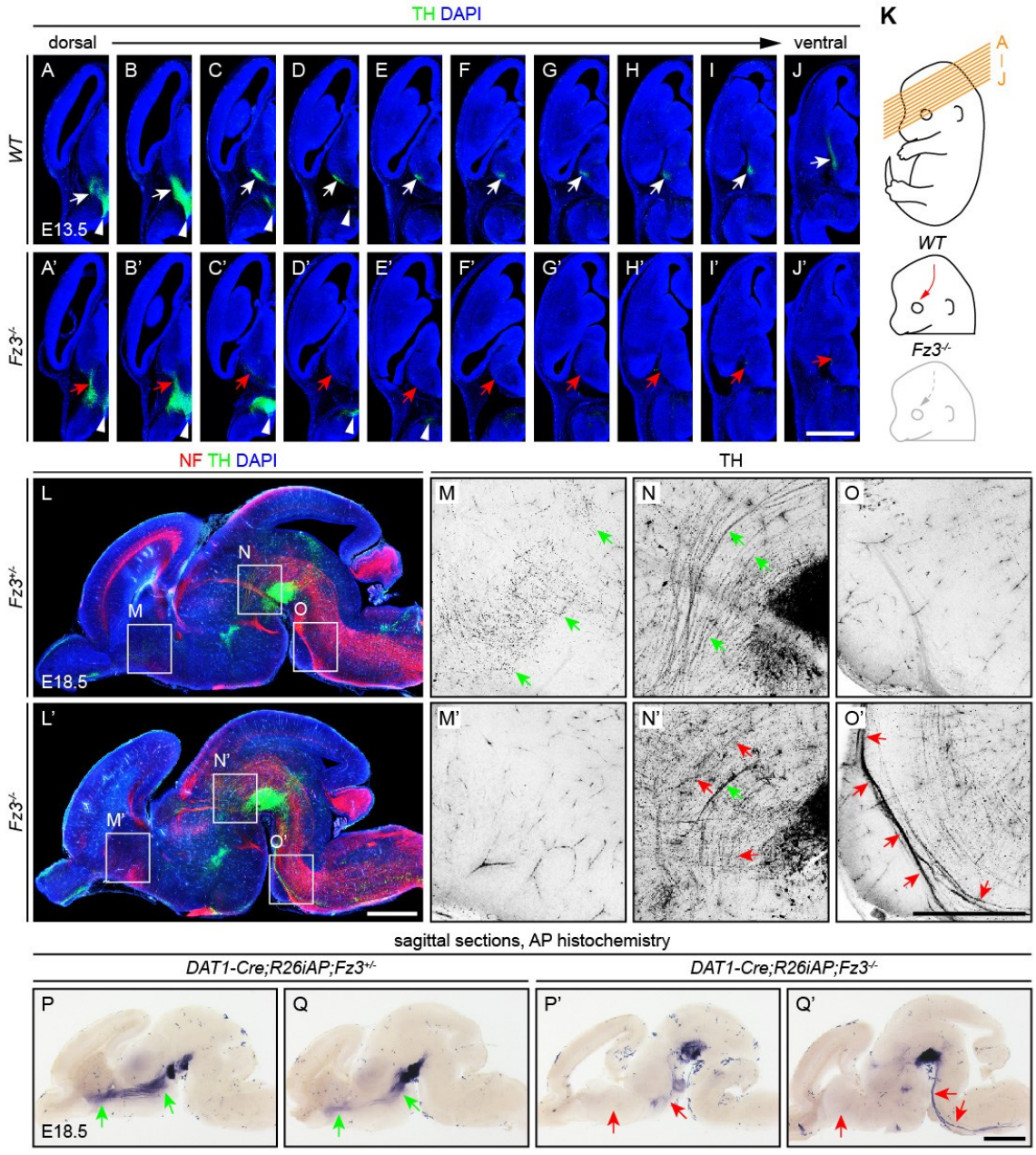
TH DAPI
dorsal
ventral
K
A
I
J
WT
Fz3-/-
E13.5
NF TH DAPI
TH
Fz3+/-
Fz3-/-
E18.5
sagittal sections, AP histochemistry
DAT1-Cre;R26iAP;Fz3+/-
DAT1-Cre;R26iAP;Fz3-/-

Figure 10. Dopaminergic neurons in the substantia nigra fail to innervate the striatum in the *Fz3*$^{-/-}$ brain

(A-R') AP staining of consecutive coronal brain sections with hPLAP activated by *DAT1-Cre* shows dopaminergic axons in the substantia nigra fail to project rostrally to the striatum in the *Fz3*$^{-/-}$ brain (green vs. red arrows). Scale bar, 1 mm.

(S) Diagrams showing planes of sections in A-R' (top), drawing the trajectory of dopaminergic axons from the substantia nigra to the striatum in *WT* brains (middle), and describing the absence of dopaminergic fiber tracts in *Fz3*$^{-/-}$ brains (bottom).

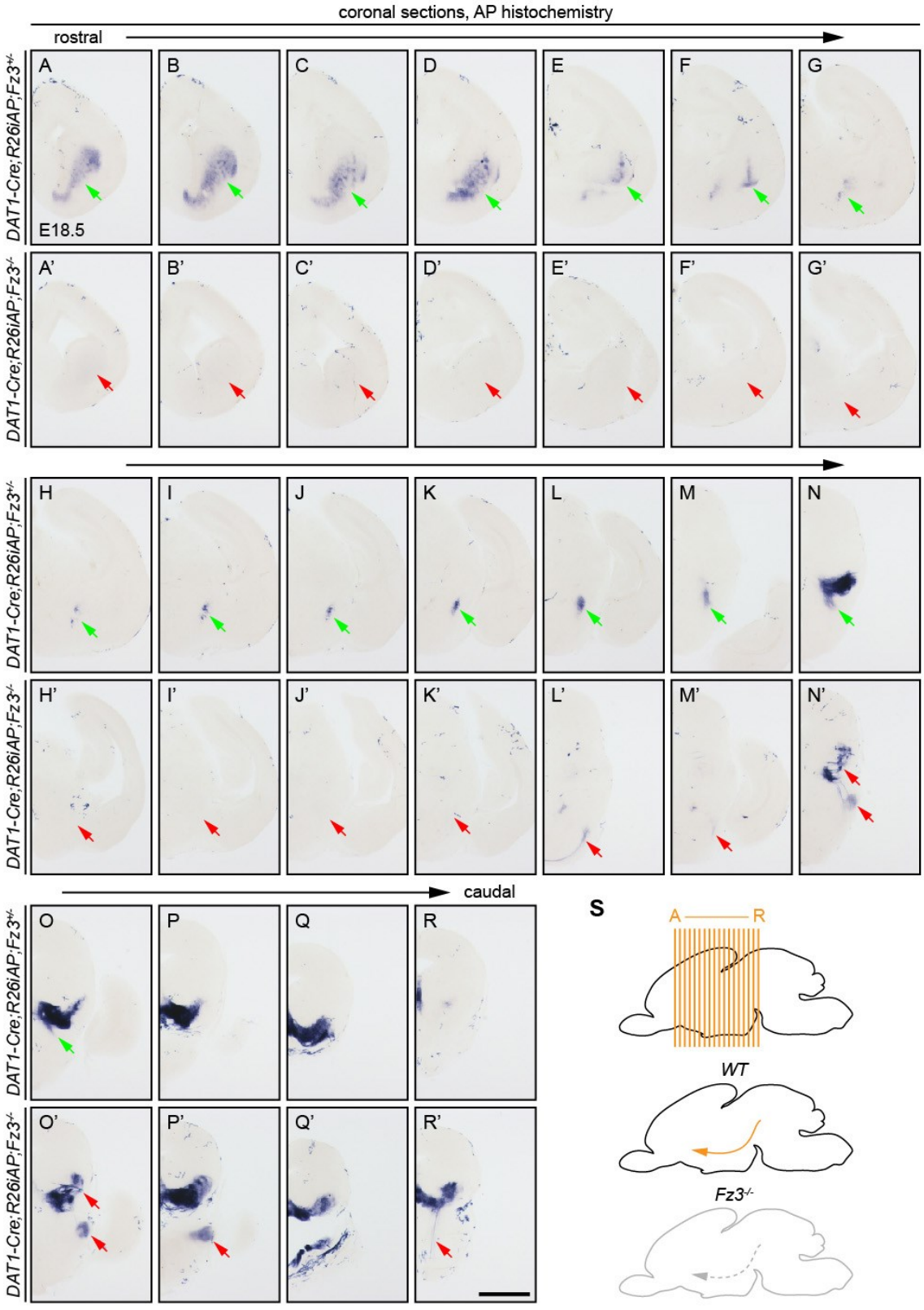
coronal sections, AP histochemistry
rostral
caudal
DAT1-Cre;R26iAP;Fz3+/-
DAT1-Cre;R26iAP;Fz3-/-
E18.5
A
B
C
D
E
F
G
A'
B'
C'
D'
E'
F'
G'
H
I
J
K
L
M
N
H'
I'
J'
K'
L'
M'
N'
O
P
Q
R
O'
P'
Q'
R'
S
A
R
WT
Fz3-/-

Figure 11. Serotonergic axons in the brainstem descend to the spinal cord and fail to innervate the forebrain in *Fz3*$^{-/-}$ embryos

(A-K) In the *Fz3*$^{-/-}$ brain, serotonergic neurons are normally generated (arrowheads), yet their axons fail to innervate the basal forebrain (white vs. red arrows), shown by 5-HT immunostaining of consecutive E13.5 brain sections. K, diagrams showing planes of sections in A-J' (top) and innervation defect of serotonergic neurons in the *Fz3*$^{-/-}$ brain (middle and bottom). Scale bar, 1 mm.

(L-O') NF and 5-HT co-immunostaining of E16.5 sagittal brain sections showing that in the *Fz3*$^{-/-}$ brain the cerebral cortex and the striatum are devoid of serotonergic axons (arrows in M and N vs. M' and N'), and serotonergic axons descend along the ventral medulla (arrows in O'). M-O' are enlarged view of boxed regions in L and L'. M-O' show only the anti-5-HT signal, with the intensity inverted. Arrows in L and L' point to the tegmentum. Scale bars: L', 1 mm; N' and O', 500 μm.

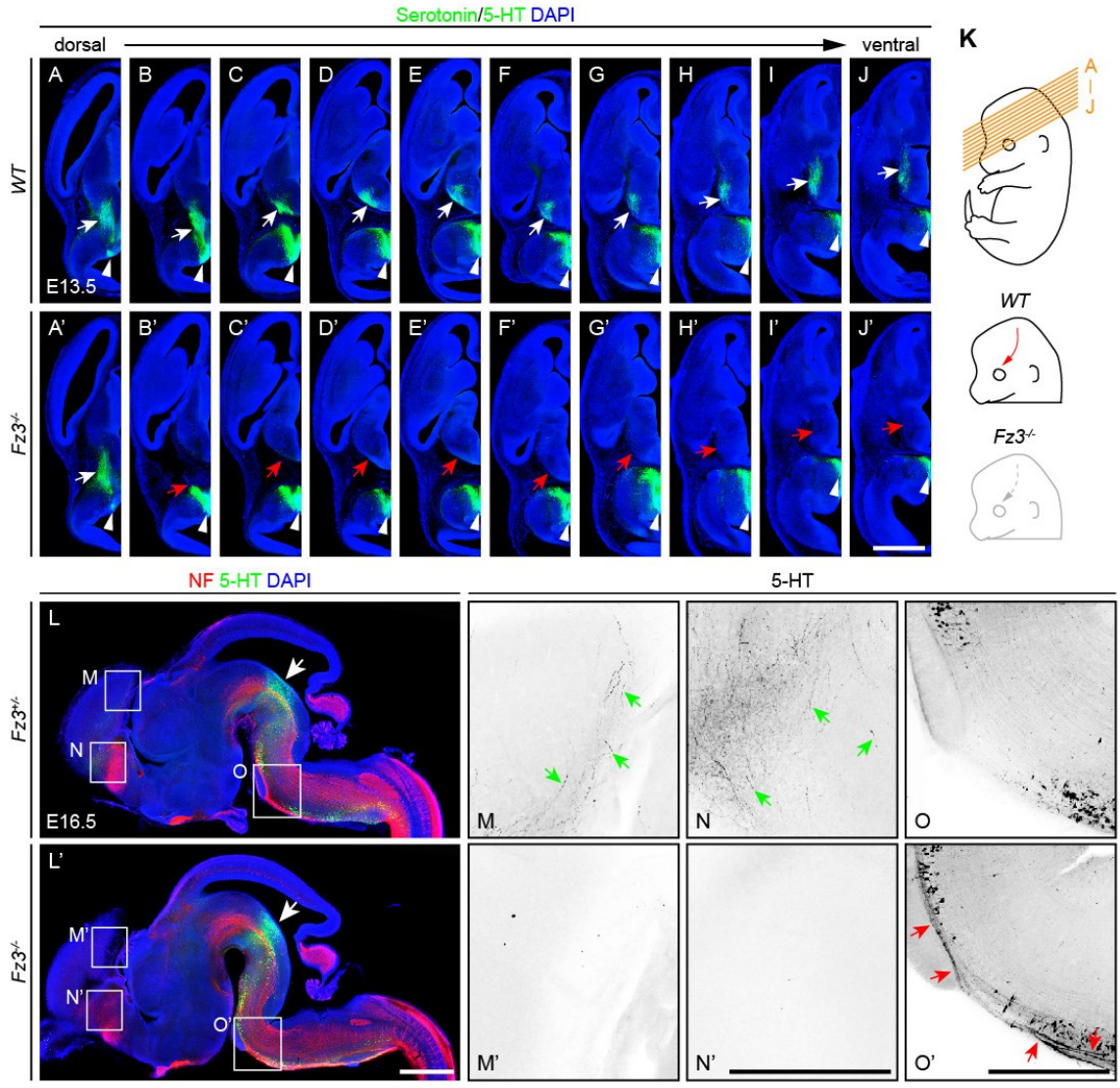
Serotonin/5-HT DAPI
dorsal
ventral
WT
Fz3-/-
E13.5
K
A
I
J
WT
Fz3-/-
NF 5-HT DAPI
5-HT
Fz3+/-
Fz3-/-
E16.5

F. Ascending fiber tracts from the spinal cord to the brain are missing in *Fz3*$^{-/-}$ embryos

In the periphery, loss of *Fz3* impairs axon growth in distinct cranial and spinal motor nerves, the guidance and growth of enteric neuronal projections, and the development of sympathetic chain ganglia and target innervation of sympathetic chains (Armstrong et al., 2011; Hua et al., 2013; Sasselli et al., 2013). However, so far it has not been robustly investigated whether *Fz3* plays any role in the development of sensory neurons. To thoroughly address this question, we generated *WT* and *Fz3*$^{-/-}$ mice carrying the *Brn3a*^{AP} allele, which expresses the *hPLAP* at the *Brn3a* locus – a pan-sensory neuron marker (Badea et al., 2009a; Eng et al., 2001). AP staining of horizontal sections from E15.5 *Brn3a*$^{AP/+}$*;Fz3*$^{+/-}$ and *Brn3a*$^{AP/+}$*;Fz3*$^{-/-}$ embryos does not reveal any abnormality in sensory nerve development and target innervation (Figure 12A-H'), further suggesting that Fz3 functions very specifically in distinct neuronal populations in the periphery during early embryonic development.

We next asked whether *Fz3* knockout affects the spinal cord circuits responsible for translating sensory stimuli into the brain. In mice and human beings, somatosensory information is perceived by primary sensory neurons whose cell bodies reside in the dorsal root ganglia (DRG) and cranial sensory ganglia and then is conveyed from the spinal cord to the brain through second-order neurons and multiple ascending fiber tracts in the spinal cord (Abraira and Ginty, 2013). To visualize these ascending fiber tracts, we recombined the *R26iAP* reporter with the *Cdx1-Cre* transgene, which efficiently recombines target alleles in all tissues caudal to the upper thorax before midgestation

(Hierholzer and Kemler, 2009; Hua et al., 2013), and performed AP staining on *WT* and *Fz3*$^{-/-}$ brain sections. AP histochemistry shows nearly completely dark staining of the spinal cord caudal to C2 and sparsely labelled blood vessel cells in the brain rostral to the nucleus abducens, consistent with previously reported expression pattern of this transgene (Figure 13A-K) (Hierholzer and Kemler, 2009). Multiple ascending spinal fiber tracts innervating various brain targets are labelled in *WT* embryos, but these fibers are diminutive and fail to innervate the thalamus in *Fz3*$^{-/-}$ brains (Figure 13A-M). Together, these data demonstrate that sensory innervation of peripheral targets is Fz3-independent, yet Fz3 signaling is required for conveying sensory information from the spinal cord to the brain.

The above results show that *Fz3*$^{-/-}$ mice have defects in sensory perception and suggest that these mice might be unable to respond to environmental stimuli. However, so far the neonatal death of *Fz3*$^{-/-}$ mice has prevented tests to examine the behavioral consequence of *Fz3* loss-of-function on sensory perception. To circumvent this problem, we generated viable *Cdx1-Cre;Fz3*$^{CKO/-}$ mice with the intention that the inactivation of *Fz3* by the *Cdx1-Cre* transgene shall present similar or nearly identical defects in ascending spinal fiber tracts as seen in *Fz3*$^{-/-}$ embryos (Hua et al., 2013). We then performed two-temperature (32^0C vs. 38^0C) and two-texture (60 grain/rough vs. 400 grain/smooth) preference assays and tested the occupancy of *WT* and *Cdx1-Cre;Fz3*$^{CKO/-}$ mice under these conditions during a 1-hour test period (Figure 14). As shown in Figure 13N and O, while *WT* littermates show clear preference for 32^0C and smooth surface after 30 minutes, *Cdx1-Cre;Fz3*$^{CKO/-}$ mice do not exhibit preference for these conditions,

suggesting that mutant mice are unable to respond to temperature and texture stimuli delivered to their feet – consistent with the anatomical defects revealed in *Fz3*$^{-/-}$ mice by AP histochemistry (Figure 13A-M).

Figure 12. Sensory innervation of peripheral targets is largely unaffected in *Fz3*$^{-/-}$ mice

(A-H') Sensory neurons and nerves with *hPLAP* expression at the *Brn3a* locus are labelled by AP histochemisty and are largely unaffected by loss of *Fz3*. Scale bar, 1 mm. (I) Planes of sections in A-H'.

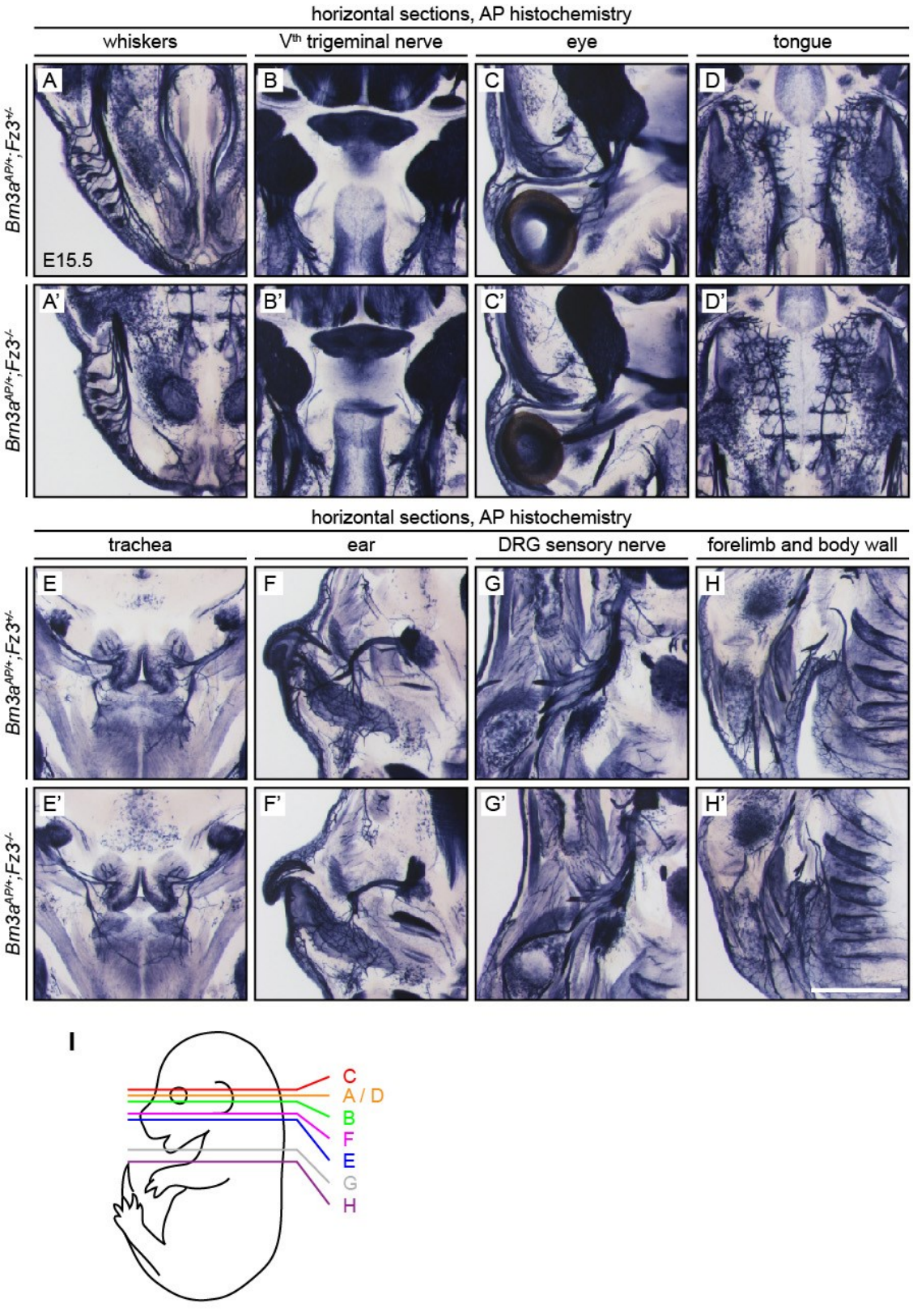
horizontal sections, AP histochemistry
whiskers
Vth trigeminal nerve
eye
tongue
A
B
C
D
E15.5
A'
B'
C'
D'
Bm3aAP/+;Fz3+/-
Bm3aAP/+;Fz3-/-
horizontal sections, AP histochemistry
trachea
ear
DRG sensory nerve
forelimb and body wall
E
F
G
H
E'
F'
G'
H'
I
C
A / D
B
F
E
G
H

Figure 13. Ascending spinal fiber tracts fail to innervate the brain in *Fz3*$^{-/-}$ embryos, and *Cdx1-Cre;Fz3*$^{CKO/-}$ mice exhibit impaired responses to texture and temperature stimuli delivered to their feet

(A-K') Ascending fiber tracts from the spinal cord to the brain are labelled by AP histochemistry of E16.5 coronal (A-I') and E18.5 sagittal (J-K') brain sections from embryos carrying the *R26iAP* reporter recombined by the *Cdx1-Cre* transgene (green arrows in A-G, J, and K). These fibers are absent in *Fz3*$^{-/-}$ brains (red arrows in A'-G', J', and K'). Scale bars, 1 mm.

(L) Planes of sections in A-I'.

(M) Diagrams showing planes of sections in J-K'(top) and absence of ascending spinal fiber tracts in the *Fz3*$^{-/-}$ brain (bottom).

(N) Behavior tests comparing occupancy of *WT* (blue line) and *Cdx1-Cre;Fz3*$^{CKO/-}$ (red line) mice on smooth surface (400 grain) over 60 minutes [mean ± standard error of the mean (SEM)]. Each *WT* mouse was tested twice and each *Cdx1-Cre;Fz3*$^{CKO/-}$ mouse was tested three times. *WT* mice show strong preference for smooth surface over time, while *Cdx1-Cre;Fz3*$^{CKO/-}$ mice do not. The occupancy of each mouse on smooth surface in the first and second 30-minute is separately listed in the middle and right chart, respectively [mean ± standard deviation (SD)].

(O) Thermal preference behavior of *WT* (blue line) and *Cdx1-Cre;Fz3*$^{CKO/-}$ (red line) mice in a two-temperature selection task over 60 minutes (mean ± SEM). Each *WT* mouse was tested twice and each *Cdx1-Cre;Fz3*$^{CKO/-}$ mouse was tested three times. *WT* mice show strong preference for 32^{0}C over time, while on the contrary *Cdx1-Cre;Fz3*$^{CKO/-}$ mice show slight preference for 38^{0}C. The occupancy of each mouse at 32^{0}C in the first and

second 30-minute is separately listed in the middle and right chart, respectively (mean ± SD).

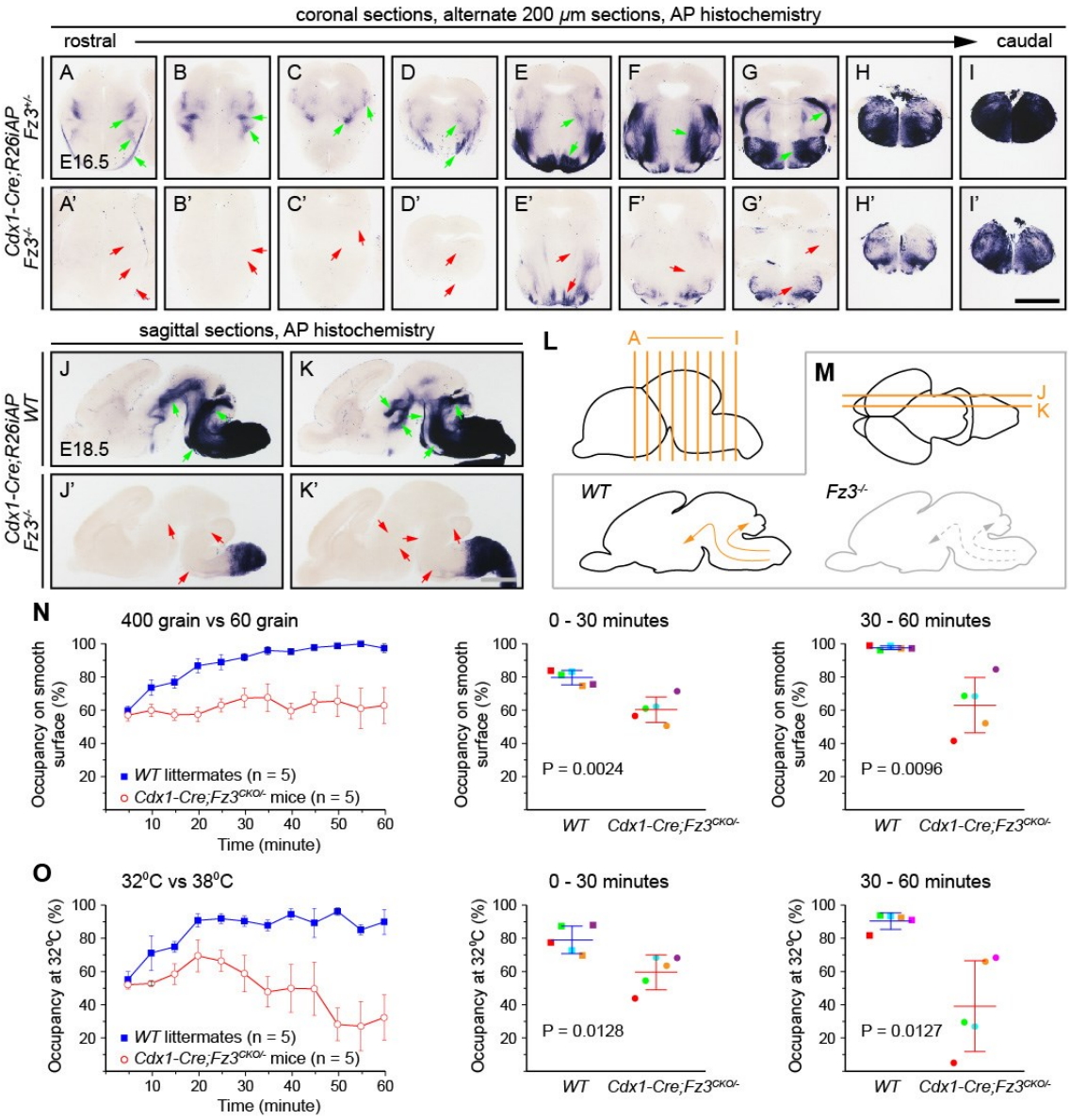

Figure 14. Behavioral tests on *WT* and *Cdx1-Cre;Fz3*$^{CKO/-}$ mice

(A) Diagram showing the equipment setup for animal behavioral tests.

(B) Setting of the four blocks in the chamber. Each diagonally opposed block pair was maintained at the same temperature or glued with the same type of sandpaper, and the configuration was reversed every 2 to 3 mice.

(C) Texture-preference assay. Occupancy of each mouse on smooth surface over 60 minutes is presented in single charts.

(D) Temperature-preference assay. Occupancy of each mouse at 32^{0}C over 60 minutes is presented in single charts.

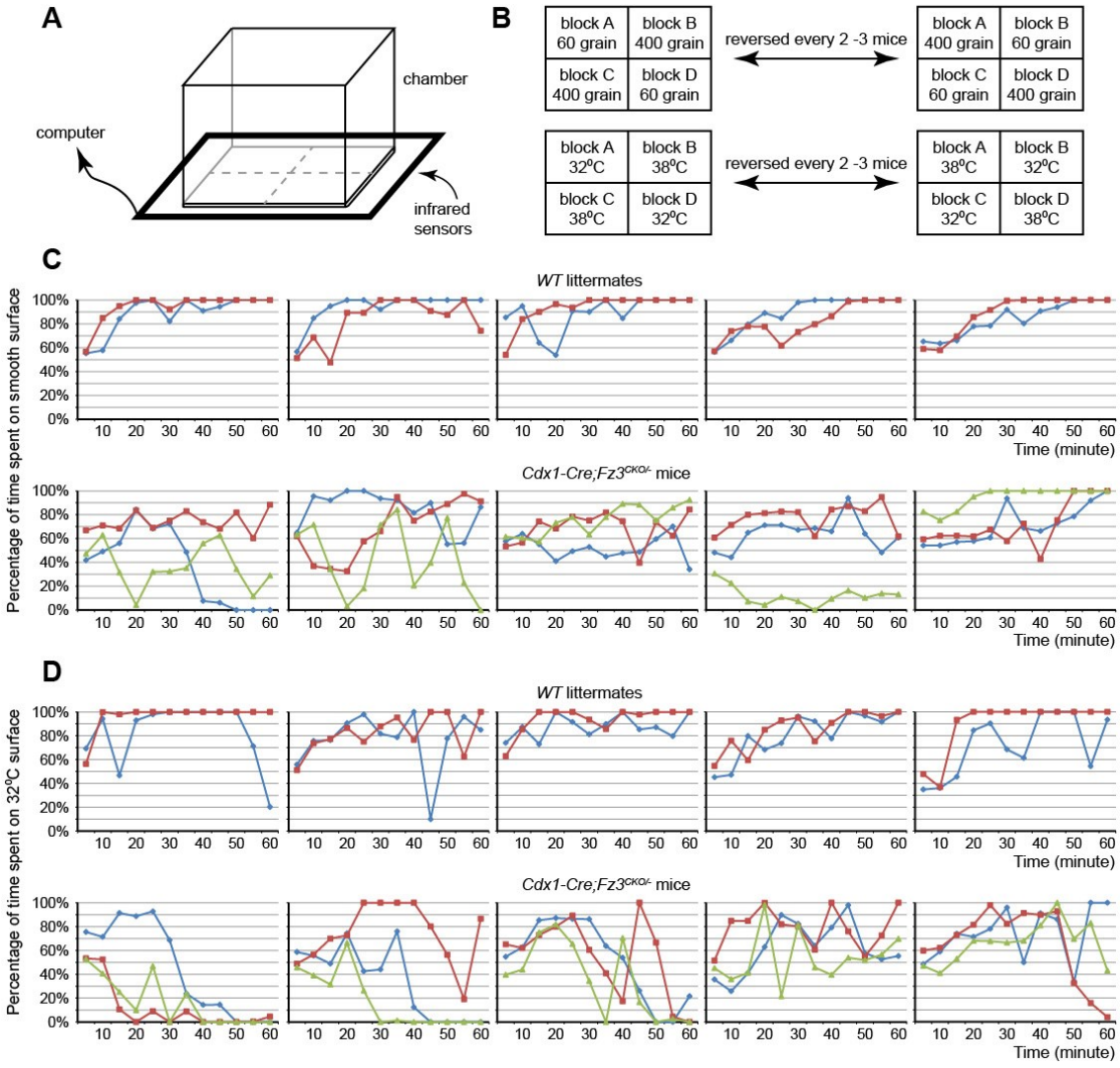
A
chamber
computer
infrared sensors
B
block A 60 grain
block B 400 grain
block C 400 grain
block D 60 grain
reversed every 2 -3 mice
block A 400 grain
block B 60 grain
block C 60 grain
block D 400 grain
block A 32°C
block B 38°C
block C 38°C
block D 32°C
reversed every 2 -3 mice
block A 38°C
block B 32°C
block C 32°C
block D 38°C
C
WT littermates
Cdx1-Cre;Fz3CKO/- mice
Percentage of time spent on smooth surface
Time (minute)
D
WT littermates
Cdx1-Cre;Fz3CKO/- mice
Percentage of time spent on 32°C surface
Time (minute)

Chapter IV: Role of *Fz3* in Motor Neurons

A. A systematic survey of peripheral nerve defects in *Fz3*$^{-/-}$ embryos

The wide expression of *Fz3* as well as the profound role of *Fz3* in the development of major fiber tracts in the mouse CNS made us wonder whether *Fz3* plays any role in the development of peripheral nerves. To address this question, we initially adopted NF immunostaining of whole-mount tissues (e.g. embryos and limbs). Following NF immunostaining, samples were cleared by benzyl benzoate and benzyl alcohol and then imaged by confocal microscopy (Sakhalkar et al., 2007). This method is particularly valuable for systematical searching for axonal development defects in mutant mice with minimal artifacts caused by sample preparation and manual side-by-side comparison. NF immunostaining on whole-mount E11.5 embryos shows a thinning of the hypoglossal (XIIth) cranial motor nerve, the phrenic nerve, and the nerves innervating the dorsal forelimb and hindlimb (Figure 15A-C'').

Since NF immunostaining on whole-mount tissues revealed specific phenotypes in *Fz3*$^{-/-}$ motor nerves, we therefore focused on motor neurons and developed two primary methods to distinctly label motor neurons and axons. We first introduced the *Hb9-EGFP* transgene to *Fz3* mutants to visualize spinal motor axons, including the phrenic nerve, and a subset of cranial motor axons, including the abducens (VIth) and XIIth motor nerves (Huettl and Huber, 2011; Wichterle et al., 2002).

Respiration is a bilaterally synchronous activity that is essential for all terrestrial vertebrates. The respiratory rhythm is primarily controlled by the pre-Bötzinger complex in the brainstem coordinating the activation of neurons in the phrenic motor column (PMC), which is the sole source of diaphragm innervation (Allan and Greer, 1997). The PMC spans approximately the 3rd to the 6th segment of the cervical spinal cord. Motor axons from this region enter the brachial plexus with most of them projecting laterally to innervate the forelimb. PMC axons that form the phrenic nerve continue to extend caudally through the thoracic cavity and eventually contact and innervate the primordial diaphragm. At the initial contacting point, the phrenic nerve branches into three primary trunks, with two of them innervating the dorsal and ventral diaphragm and the other one innervating the crus of the diaphragm (Allan and Greer, 1997; Burgess et al., 2006). Since NF immunostaining showed a marked thinning of the phrenic nerve in *Fz3*$^{-/-}$ embryos, we stained GFP and nicotinic acetylcholine receptors on flat-mount *Hb9-EGFP;WT* and *Hb9-EGFP;Fz3*$^{-/-}$ diaphragms to further probe this defect (Figure 15D-H'').

In the *WT* diaphragm, the phrenic nerve ramifies the entire diaphragm, and axonal terminals are well co-localized with neuromuscular junctions (Figure 15D-D''). In all *Fz3*$^{-/-}$ diaphragms examined, the phrenic nerve is thinned and exhibits less elaborate terminal structures, and the innervation of the diaphragm displays defects to various extents (Figure 15E-H''). In more than half of *Fz3*$^{-/-}$ diaphragms, the ventral part is not innervated (Figure 15F-F''). In more severe cases, the crura of the diaphragm are not innervated (Figure 15G-G''). In the most severe scenario, the phrenic nerve is nearly

completely absent, and acetylcholine receptors are dispersed along muscle fibers in the diaphragm (Figure 15H-H’’).

Figure 15. Axon growth defects in the XIIth cranial and phrenic nerves in *Fz3*$^{-/-}$ embryos

(A-C') NF immunostaining shows thinned XIIth and phrenic nerves (green arrows in B and C vs. red arrowheads in B' and C') in E11.5 *Fz3*$^{-/-}$ embryos. The nerve roots and the proximal segment of the XIIth nerve appear to be unaffected by loss of *Fz3*. Images in B-C' are maximum intensity projections from consecutive *Z* stacks covering the individual nerves. Scale bars: A', 1 mm; B' and C', 200 μm.

(D-H') Flat-mounts of the diaphragm show variably defective motor innervation in E18.5 *Hb9-EGFP;Fz3*$^{-/-}$ embryos. Panels D-H show half of a diaphragm with the midline at the top. D'-H' and D''-H'' show enlargements of the lateral and ventral regions, respectively, boxed in D-H. D, dorsal; V, ventral; M, medial; L, lateral. E-H show examples of mild, moderate, severe, and complete phenotypes, with the fraction of embryos in each class shown in parentheses. Scale bars: H, 1 mm; H'', 100 μm.

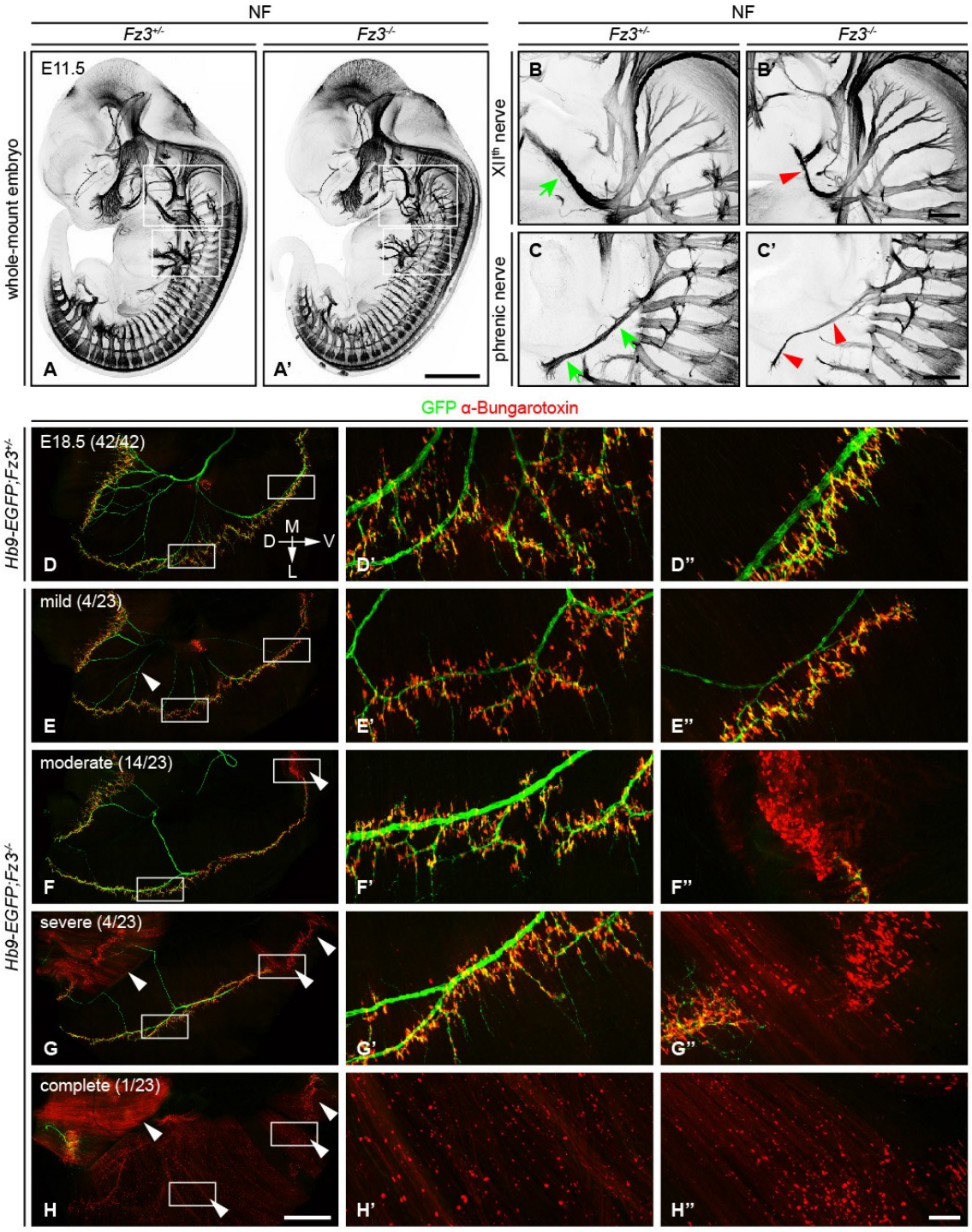
NF
NF
Fz3+/-
Fz3-/-
Fz3+/-
Fz3-/-
whole-mount embryo
E11.5
A
A'
XIIth nerve
phrenic nerve
B
B'
C
C'
GFP α-Bungarotoxin
Hb9-EGFP;Fz3+/-
Hb9-EGFP;Fz3-/-
E18.5 (42/42)
M
D
V
L
D
D'
D''
mild (4/23)
E
E'
E''
moderate (14/23)
F
F'
F''
severe (4/23)
G
G'
G''
complete (1/23)
H
H'
H''

B. *Fz3*$^{-/-}$ cholinergic neurons in the basal forebrain fail to innervate the thalamus

The second method we developed to specifically label motor neurons and axons was AP histochemistry of sections from *WT* and *Fz3*$^{-/-}$ embryos carrying both *ChAT-IRES-Cre* and *R26iAP* alleles. The *ChAT-IRES-Cre* allele expresses *Cre* recombinase under the endogenous *ChAT* promoter and thus in all cholinergic neurons, and the *R26iAP* reporter ubiquitously produces an inactive hPLAP, which can be transformed into an active form upon Cre-mediated recombination (Badea et al., 2009b). As a result and in fact, the combination of *ChAT-IRES-Cre* and *R26iAP* allows us to faithfully label cholinergic neurons and axons in prenatal embryos.

Cholinergic neurons in the mouse telencephalon can be divided into two major groups based on their anatomical locations, those in the striatal compartment of the basal ganglia and others in the basal forebrain. While cholinergic neurons of striatal structures are interneurons communicating with local cells, those in the basal forebrain innervate a variety of targets, including the cerebral cortex, the hippocampus, and the thalamus (Woolf, 1991). As seen in Figure 16B, AP staining of consecutive coronal sections from E18.5 *WT* brains clearly captures the cholinergic innervation of the thalamus. In the *WT* brain, cholinergic processes extend from the basal forebrain to the internal capsule, and finally enter the thalamus. In contrast, upon loss of *Fz3*, cholinergic axons in the basal forebrain wander around the globus pallidus, form aberrant fiber tracts, and fail to innervate the thalamus (Figure 16B).

Notably in *Fz3*$^{-/-}$ brains, the cerebral cortex and the thalamus are completely disconnected, and the internal capsule is defective (Wang et al., 2002). As the internal capsule starts to form at E13.5 when the development of ChAT-immunoreactive cells just begins, it is very likely that the axonal projection of cholinergic neurons in the basal forebrain relies on the intact internal capsule (Metin and Godement, 1996; Schambra et al., 1989). On the other hand, the failure of visualizing cholinergic innervation of other brain structures at E18.5 by this approach might simply reflect the relatively late development of such processes and/or insufficient accumulation of AP proteins in these processes.

Figure 16. Diverse defects in cholinergic neurons shown by AP histochemisty in *ChAT-IRES-Cre;R26iAP;Fz3*$^{-/-}$ embryos

(A) Diagrams showing the planes of sections from E18.5 heads in B-O'.

(B) Forebrain cholinergic neurons in consecutive coronal sections. The major cholinergic fiber tract passing through the striatum is missing in the *Fz3*$^{-/-}$ forebrain (green arrows in f and g vs. red arrowheads in f' and g'). GP, globus pallidus. Scale bar, 1 mm.

(C) The VIIth motor nucleus (arrows) and nerve (arrowheads) in consecutive coronal sections. The majority of *Fz3*$^{-/-}$ VIIth motor neurons fail to migrate cadually to rhombomere 6. Scale bar, 1 mm.

(D-E') The dorsal motor nucleus of the Xth nerve (blue and orange arrows), the motor nucleus of the XIIth nerve (green and red arrows), and axons from these nuclei (arrowheads, same color scheme) in consecutive coronal (D) and sagittal (E and E') sections. Scale bars, 1 mm.

(F-H') Innervation of facial muscles by the VIIth nerve in sagittal (F-G') and coronal (H and H') sections. In *Fz3*$^{-/-}$ heads, facial muscles are not innervated (green arrows in F-H vs. red arrows in F'-H'). Scale bars, 1 mm.

(I-K') Cholinergic axons within the retro-orbital and palatal regions in sagittal (I and I') and coronal (J-K') sections. In *Fz3*$^{-/-}$ embryos, the number of axons is reduced (green arrows in I-K vs. red arrows in I'-K'). Scale bars, 1 mm.

(L-M') Innervation of tongue musculature by the XIIth nerve in sagittal (L and L') and coronal (M and M') tongue sections. In *Fz3*$^{-/-}$ embryos, the number of axons is reduced (green arrows in L and M vs. red arrows in L' and M'). Scale bars, 1 mm.

(N-O') Cholinergic neurons in the vomeronasal organ in coronal head sections. In *Fz3*$^{-/-}$ embryos, these neurons are markedly reduced (green arrows in N and O vs. red arrows in N' and O'). Scale bars: N', 1 mm; O', 200 μm.

(P-S') Innervation of the diaphragm by the phrenic nerve visualized by AP histochemistry on flat-mount diaphragms. Q, R, and S, enlarged view of boxed regions in P; Q', R', and S', enlarged view of boxed regions in P'. Branching is diminished and number of motor terminals is reduced in the moderately affected *Fz3*$^{-/-}$ diaphragm. D, dorsal; V, ventral. Scale bars, 1 mm.

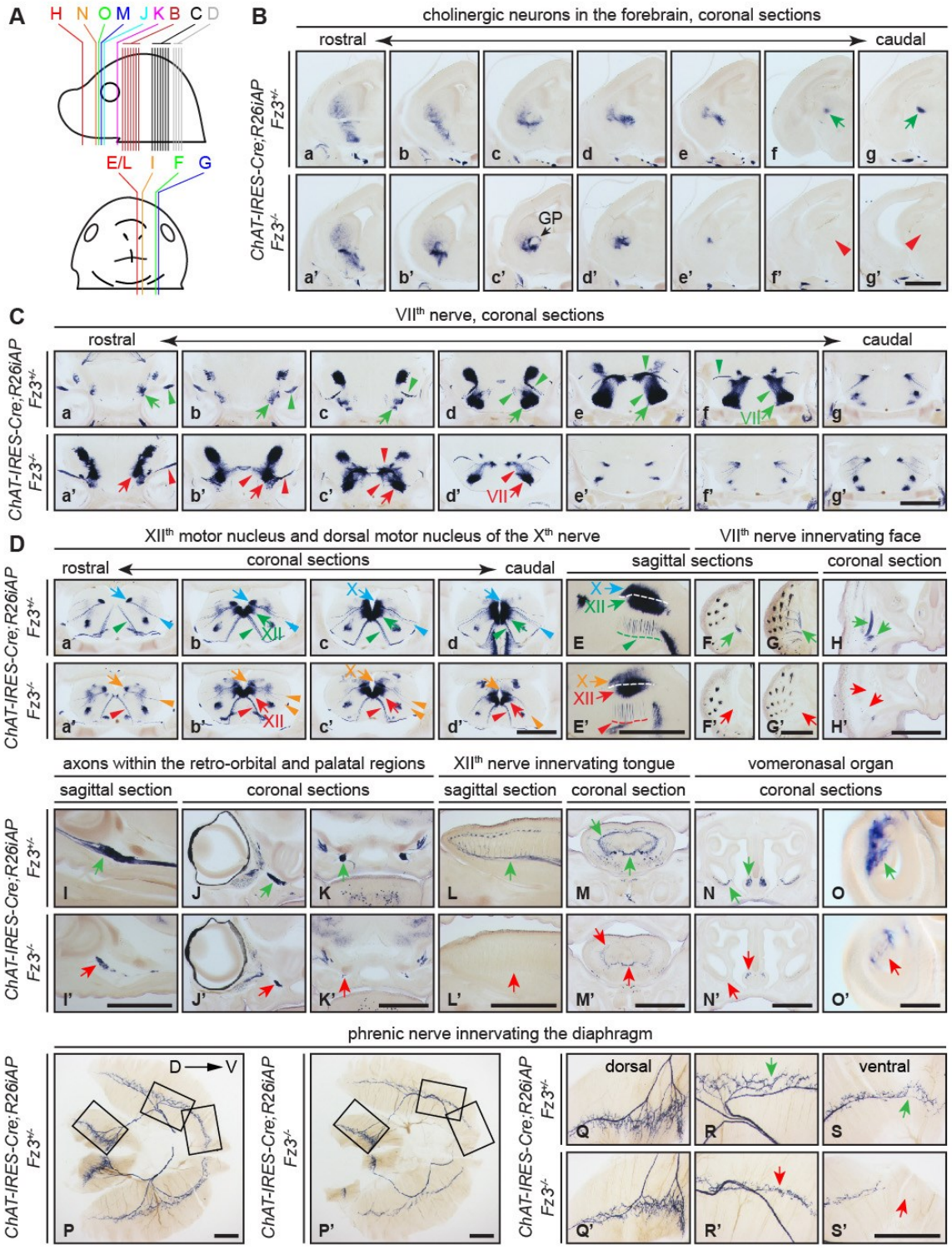
A
H N O M J K B C D
E/L I F G
B
cholinergic neurons in the forebrain, coronal sections
rostral
caudal
ChAT-IRES-Cre;R26iAP Fz3+/-
ChAT-IRES-Cre;R26iAP Fz3-/-
GP
C
VIIth nerve, coronal sections
rostral
caudal
VII
D
XIIth motor nucleus and dorsal motor nucleus of the Xth nerve
VIIth nerve innervating face
rostral
coronal sections
caudal
sagittal sections
coronal section
X
XII
axons within the retro-orbital and palatal regions
XIIth nerve innervating tongue
vomeronasal organ
sagittal section
coronal sections
sagittal section
coronal section
coronal sections
phrenic nerve innervating the diaphragm
D → V
dorsal
ventral

Figure 17. The IIIrd, IVth, and VIth cranial nerves and their target innervation are not affected by loss of *Fz3*

(A-L') The IIIrd and IVth cranial motor nuclei and nerves visualized by AP staining of consecutive coronal sections from E18.5 *ChAT-IRES-Cre;R26iAP;Fz3*$^{+/-}$ and *ChAT-IRES-Cre;R26iAP;Fz3*$^{-/-}$ heads. Motor nuclei and axon tracts or nerves are indicated by arrows and arrowheads, respectively. Panels E and F, and E' and F' are vertically offset as indicated by the red arrows. Planes of sections in Figure 17 are shown schematically in Figure 18J. Scale bar, 1 mm.

(M-R') Innervation of extraocular muscles by the IIIrd, IVth, and VIth nerves visualized by AP staining of consecutive coronal sections from E18.5 *ChAT-IRES-Cre;R26iAP;Fz3*$^{+/-}$ and *ChAT-IRES-Cre;R26iAP;Fz3*$^{-/-}$ heads. Scale bar, 1 mm.

(S and S') IIIrd and IVth nerves visualized in lateral views of NF-immunostained whole-mount E11.5 *Fz3*$^{+/-}$ and *Fz3*$^{-/-}$ embryos. Scale bar, 500 μm.

(T and T') The VIth nerve visualized by NF and GFP co-immunostaining of 100 μm-thick horizontal sections from E12.5 *Hb9-EGFP;Fz3*$^{+/-}$ and *Hb9-EGFP;Fz3*$^{-/-}$ heads. Scale bar, 500 μm.

(U and U') The VIth nerve visualized by GFP immunostaining of 700 μm-thick horizontal sections from E13.5 *Hb9-EGFP;Fz3*$^{+/-}$ and *Hb9-EGFP;Fz3*$^{-/-}$ embryos. Scale bar, 500 μm.

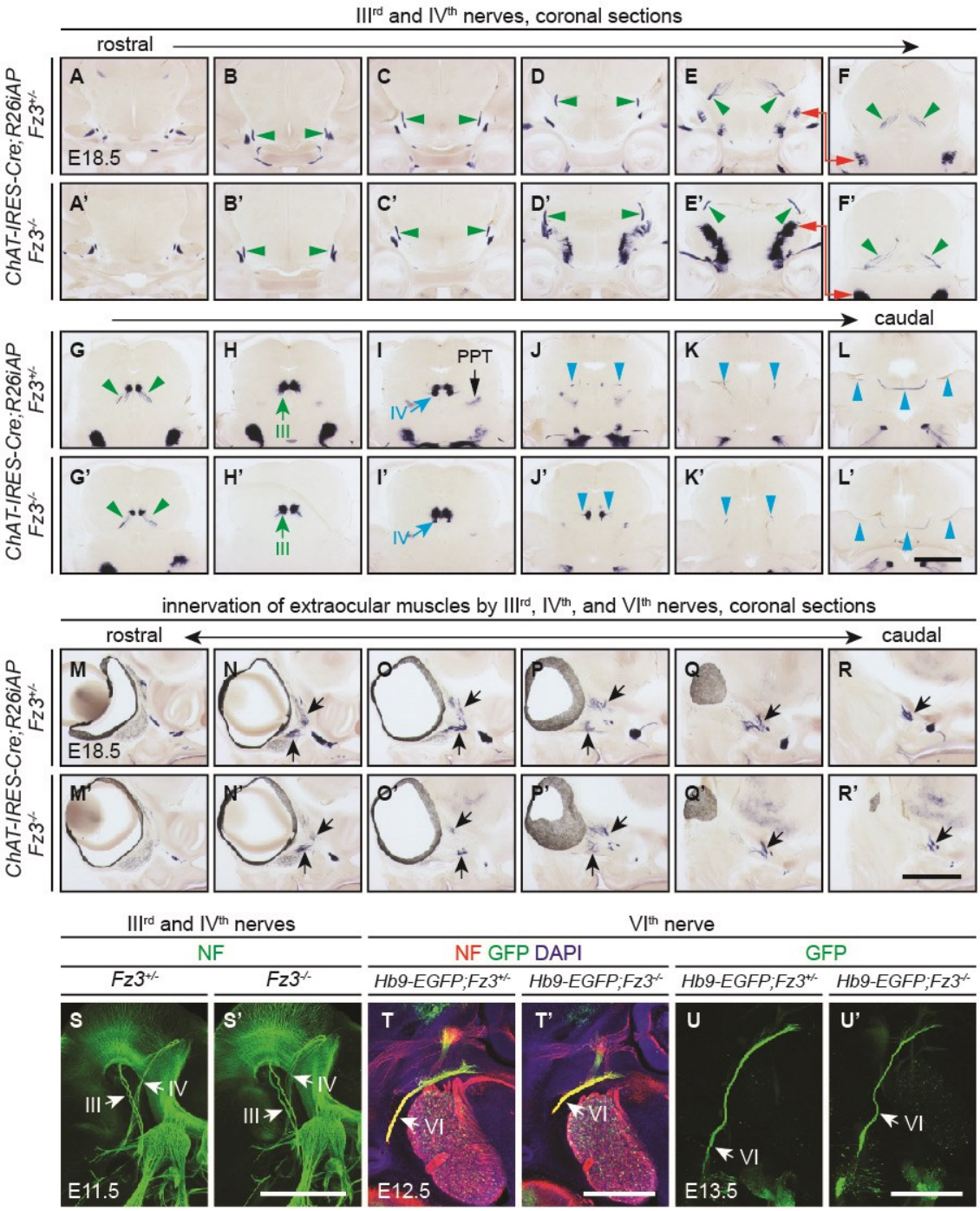
IIIrd and IVth nerves, coronal sections
rostral
caudal
ChAT-IRES-Cre;R26iAP Fz3+/-
ChAT-IRES-Cre;R26iAP Fz3-/-
A
B
C
D
E
F
A'
B'
C'
D'
E'
F'
E18.5
G
H
I
J
K
L
G'
H'
I'
J'
K'
L'
PPT
III
IV
innervation of extraocular muscles by IIIrd, IVth, and VIth nerves, coronal sections
M
N
O
P
Q
R
M'
N'
O'
P'
Q'
R'
IIIrd and IVth nerves
VIth nerve
NF
NF GFP DAPI
GFP
Fz3+/-
Fz3-/-
Hb9-EGFP;Fz3+/-
Hb9-EGFP;Fz3-/-
S
S'
T
T'
U
U'
VI
E11.5
E12.5
E13.5

Figure 18. The Vth cranial motor nerve is not affected by loss of *Fz3*

(A-G') The Vth motor nucleus and nerve visualized by AP staining of continuous coronal sections from E18.5 *ChAT-IRES-Cre;R26iAP;Fz3*$^{+/-}$ and *ChAT-IRES-Cre;R26iAP;Fz3*$^{-/-}$ heads. The Vth motor nucleus and axon tract/nerve are indicated by arrows and arrowheads, respectively. Scale bar, 1 mm.

(H-I') Innervation of mastication muscles by the Vth nerve visualized by AP histochemistry of coronal sections from E18.5 *ChAT-IRES-Cre;R26iAP;Fz3*$^{+/-}$ and *ChAT-IRES-Cre;R26iAP;Fz3*$^{-/-}$ heads. Scale bar, 1 mm.

(J and K) Diagrams showing planes of sections in Figures 17 (J) and Figure 18 (K).

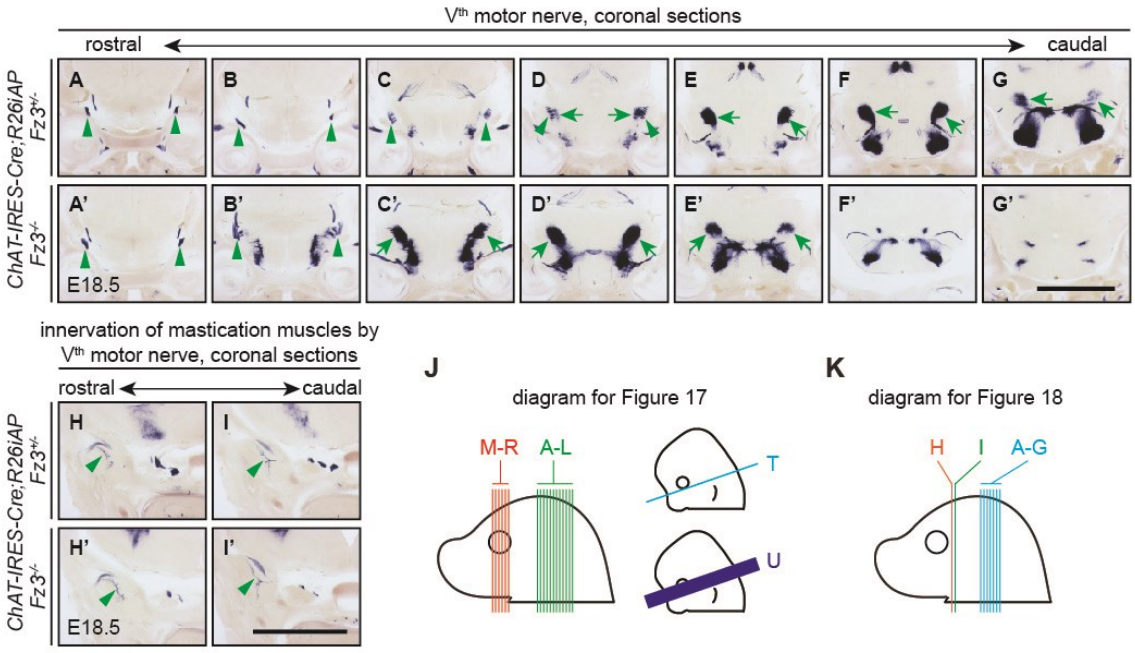

C. *Fz3* is required for tangential migration and target innervation of facial branchiomotor neurons

In addition to cholinergic neurons in the forebrain, AP histochemistry also faithfully marks individual cranial motor nuclei and nerves, thereby allowing us to dissect whether *Fz3* plays any role in the development of cranial motor neurons. The oculomotor (III^{th}) and trochlear (IV^{th}) motor nerves could be unambiguously identified by AP staining of consecutive E18.5 brain sections as well as NF immunostaining on whole-mount E11.5 embryos, and the VI^{th} motor nerve is decorated by *GFP* expression in embryos carrying the *Hb9-EGFP* reporter (Figure 17). These motor nerves together control eye movements by innervating extraocular muscles, and *Fz3* inactivation has no or minimal effects on these nerves (Figure 17). In addition, loss of *Fz3* does not affect the trigeminal (V^{th}) motor nerve. The V^{th} motor nerve in $Fz3^{-/-}$ embryos is intact and innervates lateral pterygoid muscles required for mastication normally (Figure 18).

Facial branchiomotor (FBM, VII^{th}) neurons are generated in rhombomere 4 (r4), and their cell bodies undergo tangential migration from r4 to r6 while leaving their axons behind. FBM axons initially extend mediodorsally, then make a sharp U-turn projecting rostroventrally to exit the brain, and finally innervate muscles of facial expression, tear glands, and salivary glands (Song et al., 2006). Our AP histochemistry successfully represents this biological process. As shown by AP staining of consecutive coronal brain sections in Figure 16C, FBM neurons in the *WT* brain form tight nuclei in the brainstem, and their axons initially extend mediodorsally, then make a sharp turn looping around the VI^{th} nucleus, and finally exit the brain. In the $Fz3^{-/-}$ brain, FBM neuron cell bodies are not

well separated from the V^{th} motor nucleus located in r2 and are scattered all the way from r2 to r6 where the final destination of this tangential migration lies, suggesting some mutant FBM neurons migrate rostrally while most of them fail to migrate all the way to r6. In addition, facial innervation of FBM neurons is completely absent in *Fz3*$^{-/-}$ embryos (Figure 16F-H'). Taken together, these data demonstrate that *Fz3* is required for the migration and facial innervation of FBM neurons.

No obvious abnormality is observed in the dorsal motor nucleus of the X^{th} nerve and the initial segments of the XII^{th} nerve (Figure 16D-E'). AP histochemistry shows a clear pattern in the innervation of tongue muscles by the XII^{th} nerve in *WT* embryos. In contrast, such innervation is largely diminished in *Fz3*$^{-/-}$ animals, consistent with the thinning defect in this nerve revealed by NF immunostaining of whole-mount E11.5 embryos (Figure 16L-M', and 15B and B'). In addition, AP staining also reveals diminished staining of cholinergic nerves within the retro-orbital and palatal regions, a nearly complete loss of cholinergic cells in the vomeronasal organ, and decreased innervation of the diaphragm by the phrenic nerve – consistent with the thinning defect in this nerve visualized by NF immunostaining of whole-mount E11.5 embryos, in *Fz3*$^{-/-}$ embryos (Figure 16I-K', 16N-S', and 15C and C').

D. *Fz3* loss-of-function results in severe thinning of dorsal limb motor nerves

In light of the essential role of *Fz3* in the development of the VIIth and XIIth cranial motor nerves, we then evaluated whether *Fz3* is required for the development of limb-innervating motor neurons (Bonanomi and Pfaff, 2010; De Marco Garcia and Jessell, 2008). By NF immunostaining of whole-mount E13.5 limbs, we found that in all *Fz3*$^{-/-}$ forelimbs and hindlimbs, spinal nerves innervating the dorsal forelimb and hindlimb are significantly thinned (Figure 19A-H', 20, and 21). In *Fz3*$^{-/-}$ forelimbs, the diameter of the spinal nerve innervating the dorsal limb is reduced by approximately 40% (Figure 19B-C' and 20). In *Fz3*$^{-/-}$ hindlimbs, the degree of reduction in the diameter of the deep peroneal nerve varies and can be grouped into two categories: moderate and severe (Figure 19D-F' and 21). About half of *Fz3*$^{-/-}$ hindlimbs show moderate defect, in which the dorsal nerve is thinned yet still visible along its distal trajectories (Figure 19E and E'). The other half of *Fz3*$^{-/-}$ hindlimbs have severe defect, in which the deep peroneal nerve is nearly completely absent (Figure 19F and F'). In addition, to confirm the sensory vs. motor identity of these dorsal limb-innervating nerves affected by *Fz3* knockout, we crossed the *Hb9-EGFP* transgene to *Fz3* mutant mice to selectively label motor axons. As verified by *GFP* expression, these defective nerves in *Fz3*$^{-/-}$ limbs are motor nerves (Figure 19I-L'').

Close examination of spinal nerves from the ventral spinal cord to the developing digits reveals that such thinning defects occur after LMC axons separate into two major nerves innervating either dorsal or ventral limb at the plexus region, and at the specific locus where the dorsal nerve further branches, as illustrated in Figure 19M. The major branch turns toward the distal dorsal limb region and carries this thinning defect in *Fz3*$^{-/-}$

embryos, while other branches are indistinguishable from their counterparts in *WT* mice. Therefore, it appears that LMC_L axons stall at particular loci in *Fz3*$^{-/-}$ forelimbs and hindlimbs. To further confirm this finding, we measured the diameter of dorsal nerves immediately proximal or distal to the branching (stalling) loci and the diameter of ventral nerves in both forelimbs and hindlimbs (Figure 19M). We found that in *Fz3*$^{-/-}$ limbs the diameter of dorsal nerves is comparable to that of *WT* nerves before branching and is markedly reduced after branching, indicating these motor nerves indeed stall at specific loci (Figure 19N). Moreover, the diameter of ventral nerves is slightly reduced, suggesting that *Fz3*$^{-/-}$ LMC_L axons do not mis-route to the ventral limb and further consolidate the stalling phenotype (Figure 19N).

In *Fz3*$^{-/-}$ embryos, medial motor column (MMC) and hypaxial motor column (HMC) axons appear intact and normally innervate axial muscles and body wall muscles, respectively (Figure 22). Therefore, although *Fz3* is wildly expressed in the mouse CNS, it is only required for the development of distinct motor neuron populations.

Figure 19. Dorsal limb-innervating motor nerves are markedly thinned in *Fz3*$^{-/-}$ mice

(A) Diagrams summarizing the innervation pattern of spinal motor nerves in *WT* (top) and *Fz3*$^{-/-}$ (bottom) limbs. SC, spinal cord; D, dorsal; V, ventral.

(B-F') NF immunostaining of whole-mount forelimbs and hindlimbs from E13.5 *Fz3*$^{+/-}$ and *Fz3*$^{-/-}$ embryos, with depth within the *Z*-stack along the dorsoventral axis color-coded from red to blue. B'-F' are magnified view of the enclosed box in B-F. The asterisk indicates the stalling point. Scale bars: F, 500 μm; F', 100 μm.

(G-H') NF immunostaining of 1 mm-thick cross sections flanking either forelimbs or hindlimbs from E12.5 *Fz3*$^{+/-}$ and *Fz3*$^{-/-}$ embryos, with the rostrocaudal axis coded by colors. The asterisk indicates the stalling point. P, proximal; D, distal. Scale bars, 500 μm.

(I-L'') The motor identity of the spinal nerve affected by *Fz3* loss-of-function is revealed by GFP and NF co-immunostaining of whole-mount forelimbs and hindlimbs from E12.5 *Hb9-EGFP* and *Hb9-EGFP;Fz3*$^{-/-}$ embryos. I'-L' are magnified view of the NF channel with depth coded by colors of the enclosed region in I-L. Similarly, I''-L'' are magnified view of the GFP channel with depth coded by colors of the enclosed region in I-L. P, proximal; D, distal; d, dorsal; i, intermediate; v, ventral. Scale bars: J and L, 500 μm; J'' and L'', 100 μm.

(M) Diagrams showing the designated loci where the diameter of nerves is measured. Schematic drawing of nerve innervation patterns in the forelimb (top) and hindlimb (bottom) are traced from B' and D', respectively. The locations of two dorsal nerve measurements (D_{Distal}, dorsal nerve diameter measured immediately distal to the stalling

point; $D_{Proximal}$, dorsal nerve diameter measured immediately proximal to the stalling point) and one ventral nerve measurement (V) are shown. Scale bar, 100 μm.
(N) Quantification of the diameter of nerves at designated loci in forelimbs (top) and hindlimbs (bottom) from three litters. *P* values are shown for the indicated pair-wise comparisons (student's t-test).

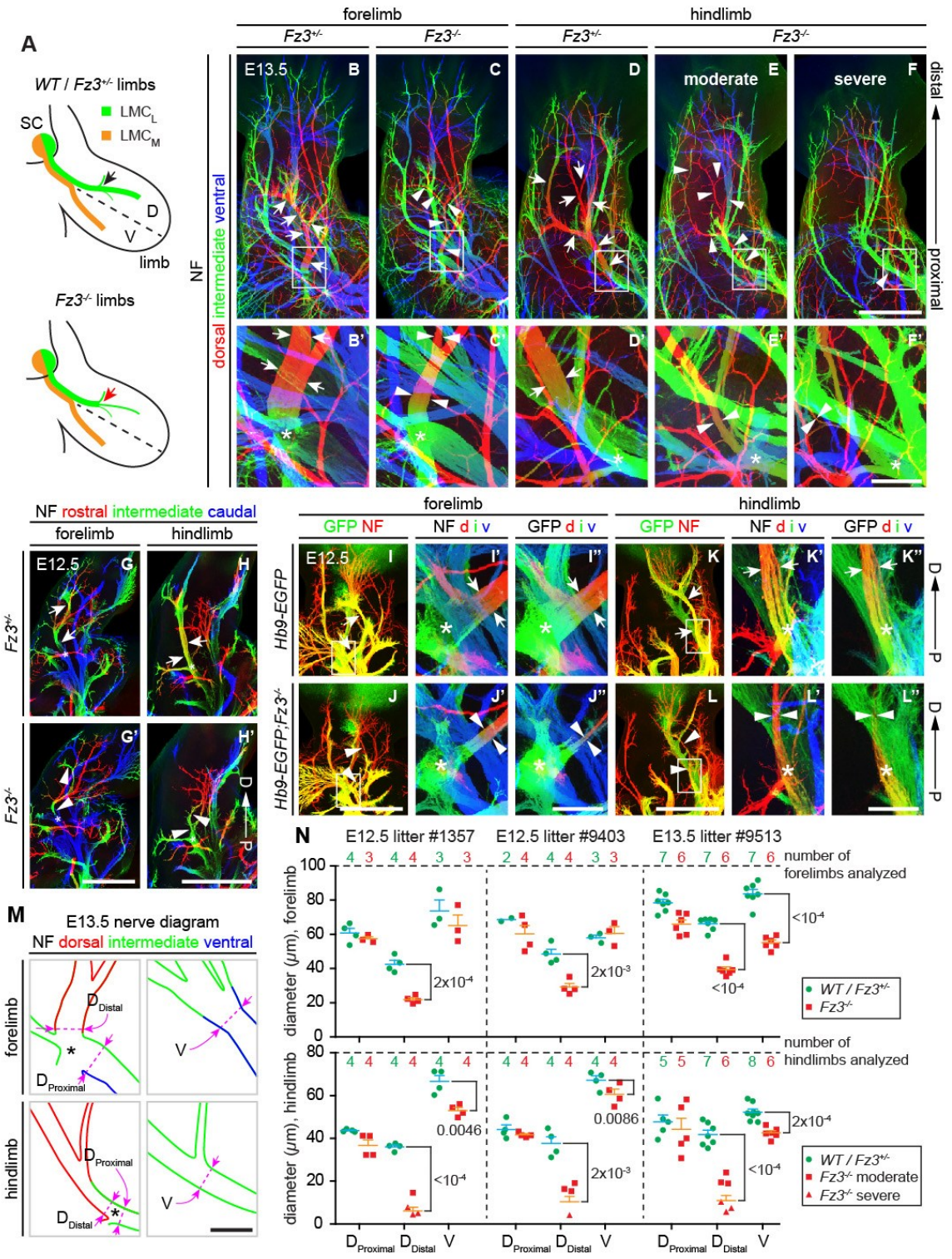
A
WT / Fz3+/- limbs
SC
LMCL
LMCM
D
V
limb
Fz3-/- limbs
forelimb
hindlimb
Fz3+/-
Fz3-/-
NF
dorsal intermediate ventral
E13.5
moderate
severe
distal
proximal
NF rostral intermediate caudal
E12.5
Hb9-EGFP
Hb9-EGFP;Fz3-/-
GFP NF
NF d i v
GFP d i v
M
E13.5 nerve diagram
NF dorsal intermediate ventral
N
E12.5 litter #1357
E12.5 litter #9403
E13.5 litter #9513
number of forelimbs analyzed
number of hindlimbs analyzed
diameter (μm), forelimb
diameter (μm), hindlimb
2x10-4
2x10-3
<10-4
0.0046
0.0086
WT / Fz3+/-
Fz3-/-
Fz3-/- moderate
Fz3-/- severe
DProximal
DDistal
V

Figure 20. Thinning of spinal motor nerves innervating the dorsal forelimb

(A-L') NF immunostaining of whole-mount forelimbs from E13.5 *WT* and *Fz3*$^{-/-}$ embryos, with depth coded by colors. A'-L' are magnified view of the enclosed box in A-L. Scale bars: F and L, 500 μm; F' and L', 100 μm.

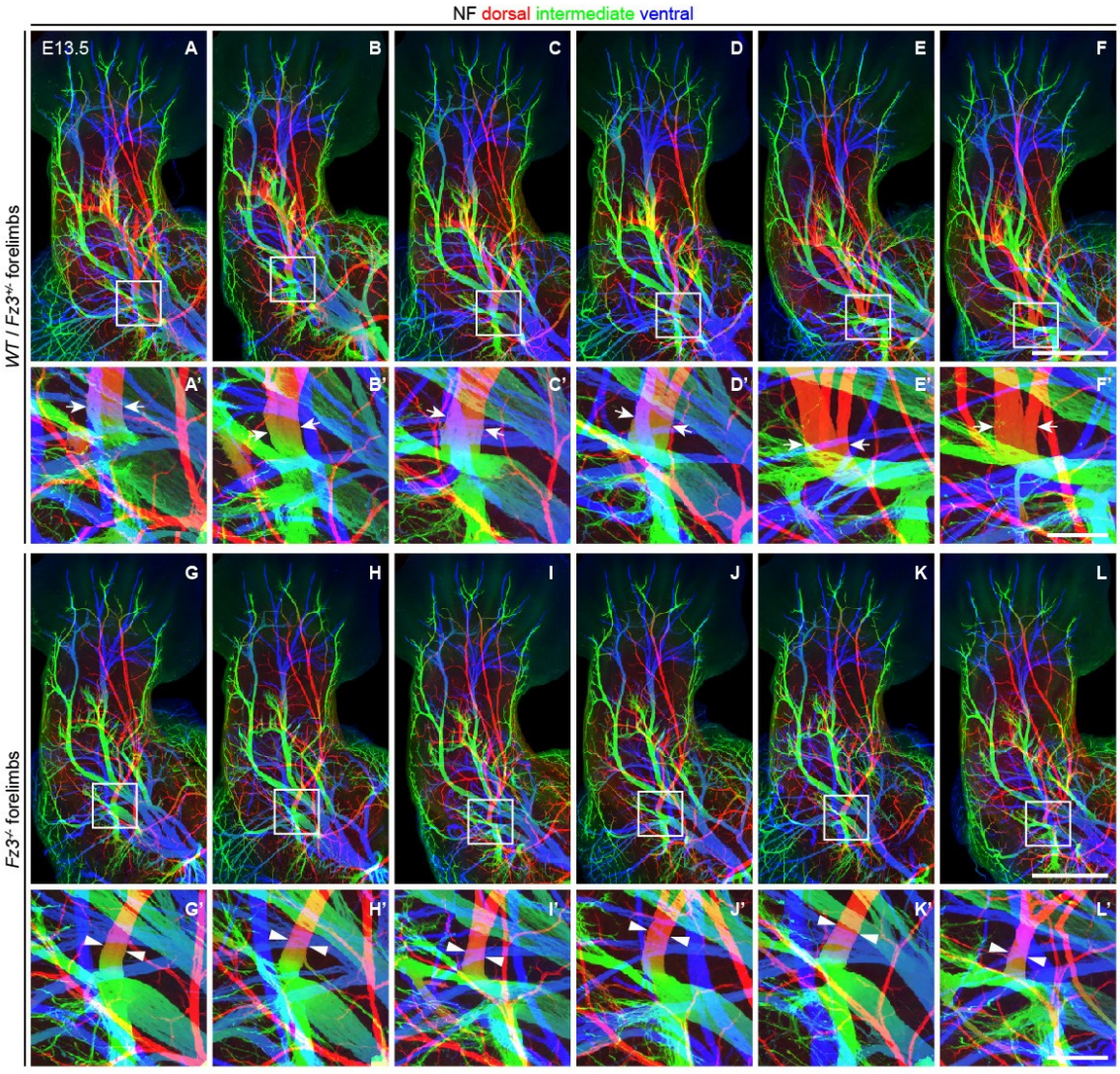

Figure 21. Thinning of spinal motor nerves innervating the dorsal hindlimb

(A-L') NF immunostaining of whole-mount hindlimbs from E13.5 *WT* and *Fz3*$^{-/-}$ embryos, with depth coded by colors. A'-L' are magnified view of the enclosed box in A-L. Scale bars: F and L, 500 μm; F' and L', 100 μm.

(M) Number and percentage of dorsal limb nerves within different categories of phenotypes in *WT* and *Fz3*$^{-/-}$ embryos.

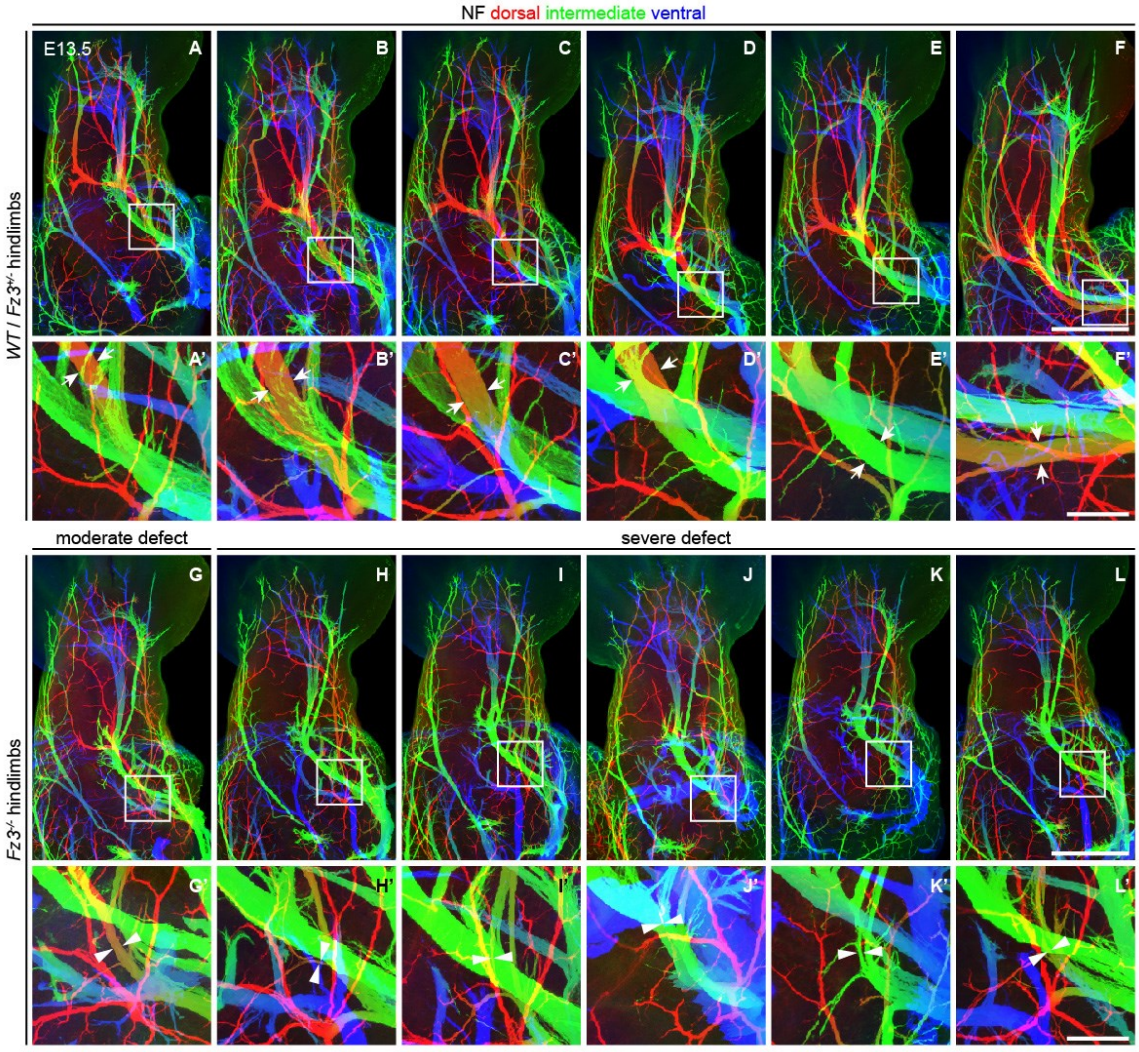

M

genotype	*WT* / *Fz3*$^{+/-}$	*Fz3*$^{-/-}$ (%)
forelimb with defect	0/32	22/22 (100%)
hindlimb with moderate defect	0/36	13/27 (48%)
hindlimb with severe defect	0/36	14/27 (52%)

Figure 22. *Fz3* knockout does not affect MMC neurons innervating axial muscles or HMC neurons innervating body wall muscles

(A and A') NF immunostaining of whole-mount thoracic pleura and abdominal peritoneum from E13.5 *WT* and *Fz3*$^{-/-}$ embryos. Scale bar, 1mm.

(B-E') NF and GFP co-immunostaining of 700 μm-thick horizontal sections from E12.5 *Hb9-EGFP;Fz3*$^{+/-}$ and *Hb9-EGFP;Fz3*$^{-/-}$ embryos. Boxed regions in B and C are enlarged in D, E, D', and E'. Scale bars, 500 μm.

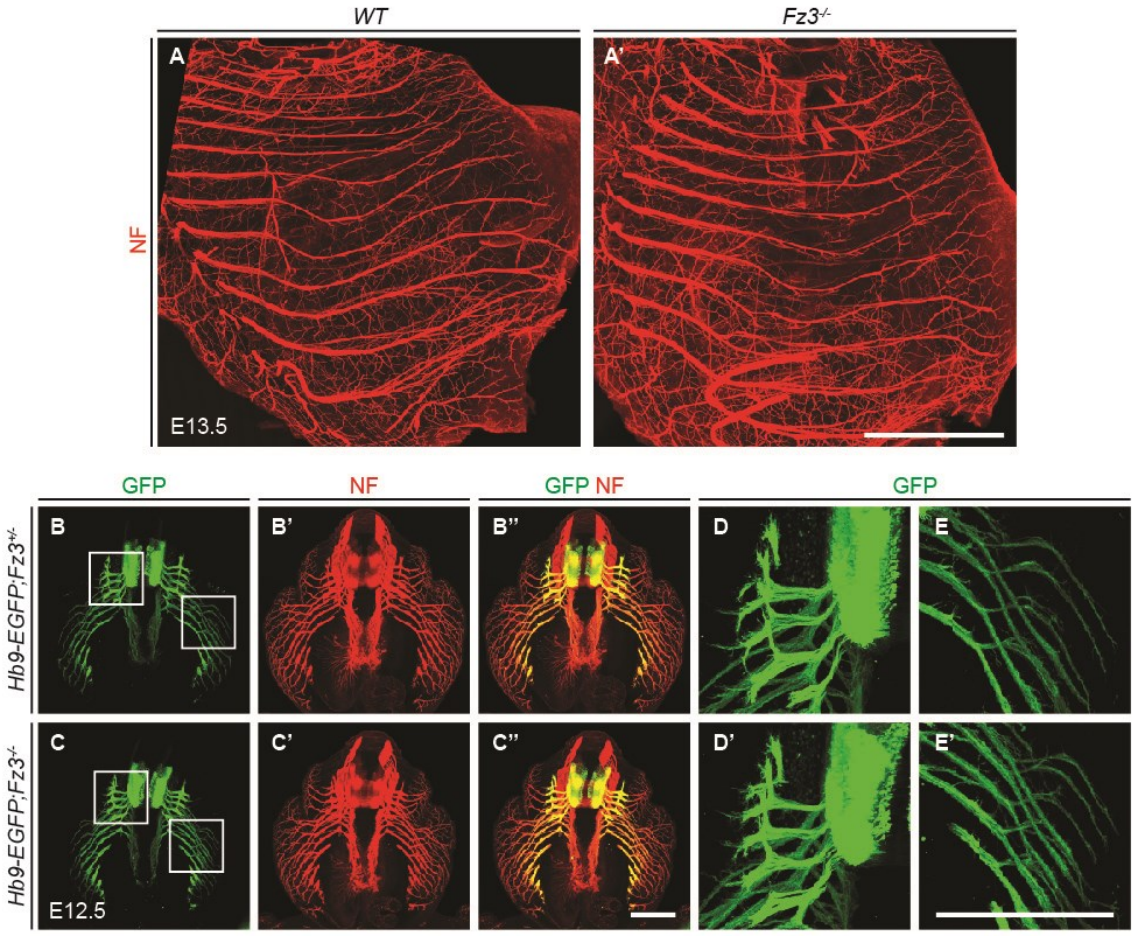

E. *Fz3* controls axon growth of LMC_L motor neurons

We next asked whether the severe thinning of the XII^{th} cranial, the phrenic, and dorsal limb-innervating motor nerves in *Fz3*$^{-/-}$ mice is due to defects in motor neuron differentiation, motor neuron survival, and axon guidance and/or growth. Since no straying motor axons were observed in *Fz3*$^{-/-}$ embryos, we therefore excluded the possibility of defective axon guidance as the primary effect of *Fz3* loss-of-function on motor neuron development. To distinguish among the remaining possibilities, we then focused on dorsal limb-innervating LMC_L motor neurons, as these neurons can be unambiguously identified by their expression of certain transcription factors and their axons can be clearly traced from the spinal cord to the limb.

In the developing mouse spinal cord, generation of cervical post-mitotic motor neurons is first detected at E9-E9.5 and is complete at E10.5-E11 (Arber et al., 1999). Motor neurons are divided into several pools positioned at stereotypical locations along the rostrocaudal and ventrodorsal axes of the spinal cord. Each motor pool innervates distinct peripheral targets and can be characterized by the expression pattern of various transcription factors. For example, the LIM homeodomain proteins Islet1 and Lhx1 are expressed by LMC_M and LMC_L motor neurons, respectively, while Islet2 and the forkhead domain transcription factor Foxp1 are pan-LMC markers. We performed Islet1 and Foxp1 immunostaining on cross sections from E11.5 lumbar spinal cords, and found that the LMC_L division identified as Foxp1^{+}/Islet1^{-} is still present in *Fz3*$^{-/-}$ mice (Figure 23B and B'). This result demonstrates that *Fz3* is not required for the differentiation of LMC_L motor neurons.

To understand the genesis of motor neurons in the context of *Fz3* knockout quantitatively, we then counted the number of LMC_L motor neurons on cross sections from E12.5 lumbar spinal cords following Islet1 and Foxp1 immunostaining. The advantage of targeting this pair of transcription factors is that the number of both LMC_M and LMC_L motor neurons can be quantified on the same section, thereby allowing the number of LMC_M neurons to serve as the internal control. As shown in Figure 23C and C', in the caudal half of the *Fz3*$^{-/-}$ lumbar spinal cord spanning the hindlimb, the number of LMC_L motor neurons is significantly decreased, while the number of LMC_M motor neurons is comparable to that of *WT* animals. In contrast, the number of both LMC_M and LMC_L motor neurons in the rostral half of the lumbar spinal cord does not show any reduction upon *Fz3* loss-of-function.

Since LMC_L motor neurons are normally specified in *Fz3*$^{-/-}$ embryos, the decrease in the number of LMC_L motor neurons suggests that *Fz3* inactivation might lead to LMC_L motor neuron death. To test this hypothesis, we performed cleaved Caspase3 immunostaining on spinal cord sections from E11.5 and E12.5 embryos when naturally occurring motor neuron death in the spinal cord has not yet begun (Oppenheim et al., 2000). As expected, very few apoptotic neurons are present in *WT* lumbar spinal cord sections. On the contrary, starting from late E11.5 and persisting to E12.5, massive cell death is detected in the caudal ~300 μm of the lumbar spinal cord as well as the brachial spinal cord in *Fz3*$^{-/-}$ embryos (Figure 23D-E'' and 24A-D''). In addition, the volume of the *Fz3*$^{-/-}$ LMC in the lumbar spinal cord appears much smaller than its counterpart in *WT*

littermates (Figure 23F-G''). Given that the anatomical location of apoptotic LMC neurons completely overlaps the place where the number of LMC_L motor neurons is decreased, these results clearly suggest that *Fz3* knockout results in apoptosis of LMC_L motor neurons. Moreover, loss of *Fz3* also markedly induces cell death in the cranial motor nuclei where axon projection and innervation are affected (Figure 23H-L). Therefore, cell death in selective motor neuron populations is a common consequence of *Fz3* loss-of-function.

Our results thus far indicate that the primary consequence of *Fz3* inactivation could be either a direct effect or an indirect effect via axon growth defects on LMC_L motor neuron survival. To distinguish these two possibilities, we took advantage of the *Bax* knockout mice, in which loss of the pro-apoptotic gene *Bax* can eliminate motor neuron apoptosis in the spinal cord (White et al., 1998), generated $Bax^{-/-};Fz3^{-/-}$ mice, and asked whether inhibition of motor neuron death could rescue the thinning defect of dorsal limb-innervating motor nerves. Although knockout of *Bax* indeed successfully inhibits early motor neuron death induced by *Fz3* loss-of-function, it does not rescue the thinning of dorsal motor nerves in $Fz3^{-/-}$ forelimbs and hindlimbs (Figure 23M-R' and 24E-G'''). Taken together, these data suggest that *Fz3* knockout directly causes defective growth of LMC_L axons, which subsequently leads to apoptosis of affected motor neurons.

Figure 23. Differentiation, quantification, and apoptosis of LMC_L motor neurons in *Fz3*$^{-/-}$ embryos, and the effect of suppressing motor neuron apoptosis

(A) Schematic diagram showing the expression pattern of transcription factors in LMC_L and LMC_M motor neurons. SC, spinal cord; D, dorsal; V, ventral.

(B and B') LMC_L and LMC_M motor neurons are identified as Foxp1$^+$/Islet1$^-$ and Foxp1$^+$/Islet1$^+$ populations, respectively, by immunostaining of cross sections from E11.5 *Fz3*$^{+/-}$ and *Fz3*$^{-/-}$ lumbar spinal cords. Continuous white line delineates lateral edge of the spinal cord, and the broken white line encircles LMC_M motor neurons. L, lateral; M, medial. Scale bar, 100 μm.

(C and C') The number of LMC_L and LMC_M motor neurons on cross sections of E12.5 *Fz3*$^{+/-}$ and *Fz3*$^{-/-}$ lumbar spinal cords. Motor neurons were counted and averaged from 12 serial sections from each of three pairs of embryos, with adjacent counted sections separated by four uncounted sections.

(D-E'') Cell death in the LMC is visualized by Islet1/2 and cleaved Caspase3 co-immunostaining of cross sections from E11.5 *Fz3*$^{+/-}$ and *Fz3*$^{-/-}$ lumbar spinal cords. Scale bar, 500 μm.

(F-G'') Reduced LMC volume as a result of cell death in the *Fz3*$^{-/-}$ spinal cord is revealed by Islet1/2 and Foxp1 co-immunostaining of cross sections from E12.5 *Fz3*$^{+/-}$ and *Fz3*$^{-/-}$ lumbar spinal cords. Scale bar, 500 μm.

(H-L) Cell death in the VIIth and XIIth cranial motor nuclei is revealed by cleaved Caspase3 and NF co-immunostaining of horizontal sections from E12.5 *Fz3*$^{+/-}$ and *Fz3*$^{-/-}$ brainstems. L illustrates the anatomical location of sections presented in H-K'. Scale bar, 100 μm.

(M-R') NF immunostaining of whole-mount forelimbs and hindlimbs from E13.5 *Bax*$^{+/-}$, *Fz3*$^{-/-}$;*Bax*$^{-/-}$, and *Fz3*$^{-/-}$;*Bax*$^{+/-}$ embryos, with depth coded by colors. M'-R' are magnified view of the enclosed box in M-R. Scale bars: R, 500 μm; R', 100 μm.

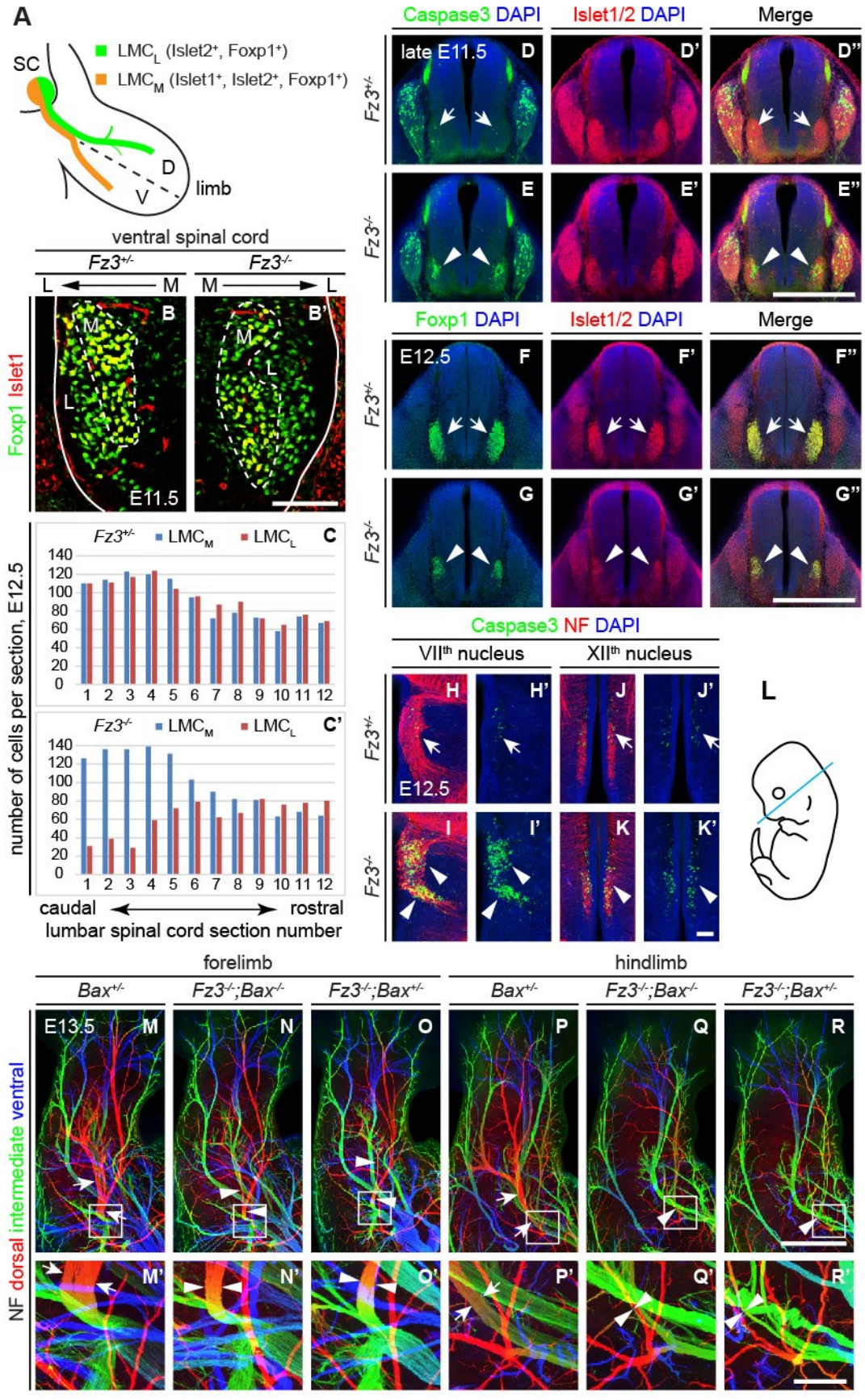
A
SC
LMC$_L$ (Islet2$^+$, Foxp1$^+$)
LMC$_M$ (Islet1$^+$, Islet2$^+$, Foxp1$^+$)
D
V
limb
ventral spinal cord
Fz3$^{+/-}$
Fz3$^{-/-}$
L
M
Foxp1 Islet1
B
B'
E11.5
C
C'
number of cells per section, E12.5
caudal
rostral
lumbar spinal cord section number
Caspase3 DAPI
Islet1/2 DAPI
Merge
late E11.5
D
D'
D''
E
E'
E''
Foxp1 DAPI
E12.5
F
F'
F''
G
G'
G''
Caspase3 NF DAPI
VIIth nucleus
XIIth nucleus
H
H'
J
J'
I
I'
K
K'
L
forelimb
hindlimb
Bax$^{+/-}$
Fz3$^{-/-}$;Bax$^{-/-}$
Fz3$^{-/-}$;Bax$^{+/-}$
E13.5
M
N
O
P
Q
R
M'
N'
O'
P'
Q'
R'
NF dorsal intermediate ventral

Figure 24. Precocious LMC_L motor neuron death in *Fz3*$^{-/-}$ embryos is suppressed by loss of *Bax*

(A-B'') Cell death in ventral spinal cord at brachial level is visualized by cleaved Caspase3 and NF co-immunostaining of cross sections from E11.5 *Fz3*$^{+/-}$ and *Fz3*$^{-/-}$ embryos. Scale bar, 500 μm.

(C-D'') Cell death in ventral spinal cord at lumbar level is visualized by cleaved Caspase3 and NF co-immunostaining of cross sections from E12.5 *Fz3*$^{+/-}$ and *Fz3*$^{-/-}$ embryos. Scale bar, 500 μm.

(E-G''') *Fz3* inactivation-induced motor neuron death is suppressed by *Bax* knockout, demonstrated by cleaved Caspase3 and Islet1/2 co-immunostaining of cross sections from E12.5 *Fz3*$^{+/-}$, *Fz3*$^{-/-}$, and *Fz3*$^{-/-}$;*Bax*$^{-/-}$ lumbar spinal cords. Boxed regions in E-G are enlarged in E'''-G'''. Scale bars: G, 500 μm; G''', 100 μm.

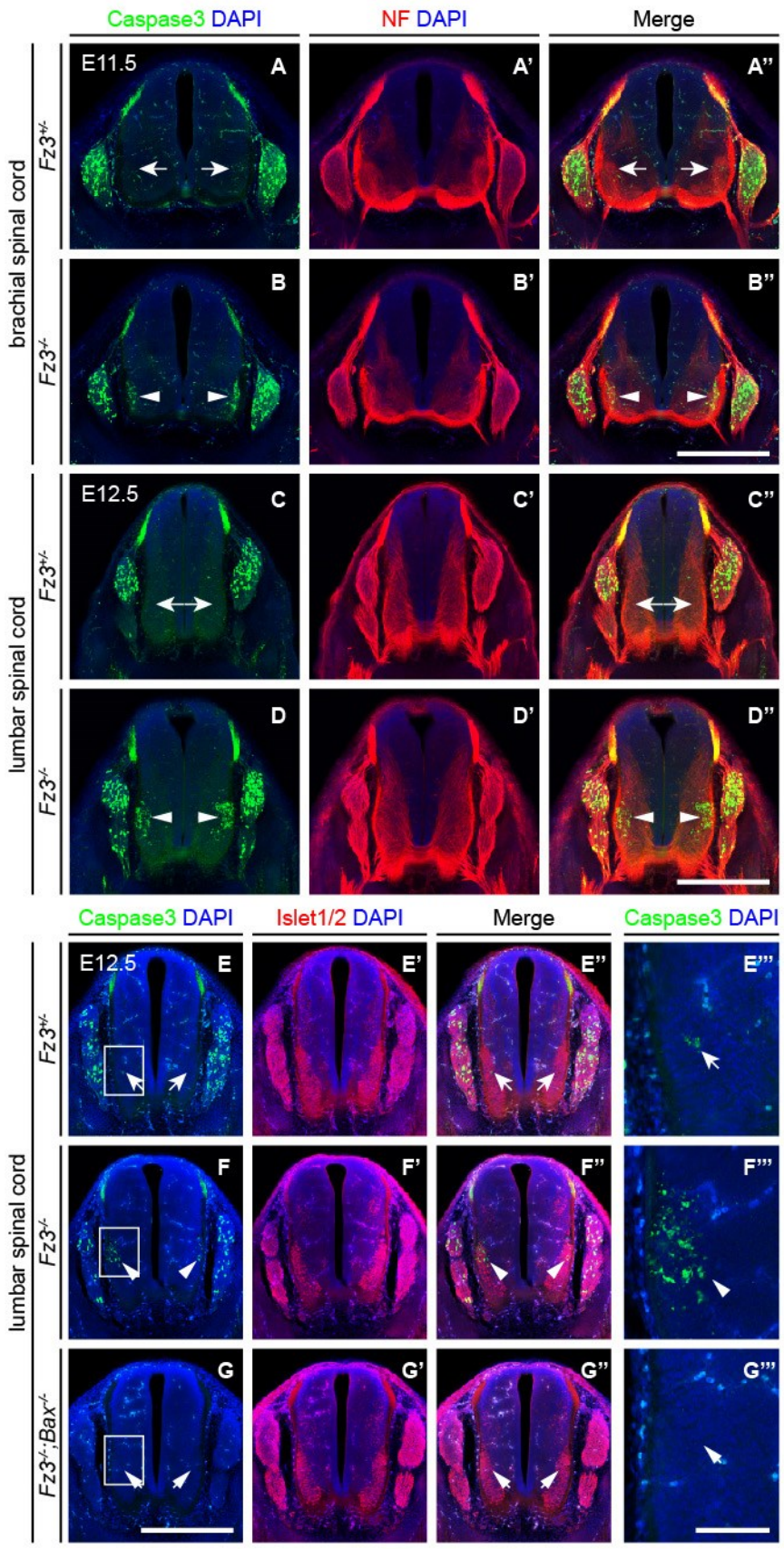
Caspase3 DAPI
NF DAPI
Merge
E11.5
A
A'
A''
B
B'
B''
E12.5
C
C'
C''
D
D'
D''
brachial spinal cord
lumbar spinal cord
Fz3+/-
Fz3-/-
Caspase3 DAPI
Islet1/2 DAPI
Merge
Caspase3 DAPI
E12.5
E
E'
E''
E'''
F
F'
F''
F'''
G
G'
G''
G'''
lumbar spinal cord
Fz3+/-
Fz3-/-
Fz3-/-;Bax-/-

F. *Fz3* functions autonomously in motor neurons to control axon growth

We next explored whether axonal development defects described above in *Fz3*$^{-/-}$ embryos reflect a cell-autonomous function of Fz3 in motor neurons. To selectively eliminate *Fz3* expression in certain cell populations, we generated a conditional *Fz3* allele (*Fz3*^{CKO}), in which the largest exon of *Fz3*, the third exon, can be flipped out in a Cre recombinase-mediated fashion (Figure 26A and B). The recombined *Fz3*^{CKO} behaves as a null, as mice homozygous for this recombined allele die after birth with a curled tail (data not shown). We ablated *Fz3* expression in motor neurons by the *Olig2-Cre* and found *Olig2-Cre;Fz3*$^{CKO/-}$ mice exhibit the complete spectrum of motor neuron phenotypes shown in *Fz3*$^{-/-}$ mice (Dessaud et al., 2007). First, FBM axons in the *Olig2-Cre;Fz3*$^{CKO/-}$ hindbrain do not form the well-defined C-shaped tracts looping around the VIth nucleus (Figure 25A and A'). Second, the XIIth nerve is markedly thinned and fails to innervate the tongue by E13.5 in *Olig2-Cre;Fz3*$^{CKO/-}$ embryos (Figure 25B-C'). Third, the phrenic nerve in mutant mice is significantly reduced in caliber (Figure 25D and D'). Last, dorsal limb-innervating motor nerves within both forelimbs and hindlimbs are markedly thinned in *Olig2-Cre;Fz3*$^{CKO/-}$ mice. In contrast, when *Fz3* is inactivated in sensory neurons by the *Wnt1-Cre* transgene, LMC_L motor axons are intact (Figure 26C-D') (Danielian et al., 1998). In sum, above results demonstrate that *Fz3* is required autonomously in motor neurons to control axon growth.

Figure 25. Fz3 functions autonomously in motor neurons to control axon growth

(A and A') VIIth axons are visualized by NF immunostaining of horizontal sections from E12.5 *Olig2-Cre;Fz3*$^{CKO/+}$ and *Olig2-Cre;Fz3*$^{CKO/-}$ brainstems. Mutant axons fail to loop around the VIth motor nucleus. R, rostral; C, caudal. Scale bar, 500 μm.

(B and B') The XIIth nerve is visualized by NF immunostaining of whole-mount E11.5 *Olig2-Cre;Fz3*$^{CKO/+}$ and *Olig2-Cre;Fz3*$^{CKO/-}$ embryos. The mutant nerve is significantly thinned. Scale bar, 500 μm.

(C and C') Innervation of tongue muscles by the XIIth cranial nerve is revealed by GFP immunostaining of coronal sections from early E13.5 *Hb9-EGFP;Olig2-Cre;Fz3*$^{CKO/+}$ and *Hb9-EGFP;Olig2-Cre;Fz3*$^{CKO/-}$ tongues. The mutant nerve fails to innerve the tongue at this embryonic stage. A, apical; B, basal. Scale bar, 500 μm.

(D and D') The phrenic nerve is visualized by NF immunostaining of whole-mount E11.5 *Olig2-Cre;Fz3*$^{CKO/+}$ and *Olig2-Cre;Fz3*$^{CKO/-}$ embryos. The mutant nerve is markedly thinned. Scale bar, 500 μm.

(E-H') NF immunostaining of whole-mount forelimbs and hindlimbs from early E13.5 *Fz3*$^{CKO/-}$ and *Olig2-Cre;Fz3*$^{CKO/-}$ embryos, with depth coded by colors. E'-H' are magnified view of the enclosed box in E-H. Scale bars: H, 500 μm; H', 100 μm.

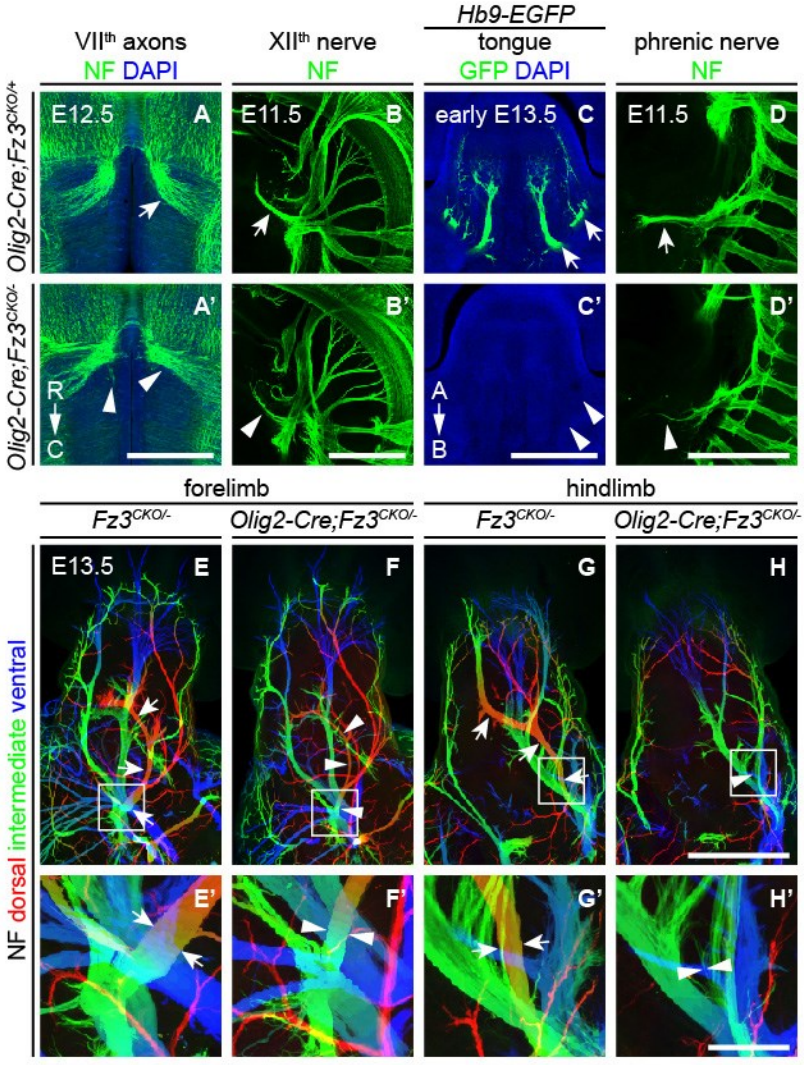
VII^th axons
NF DAPI
XII^th nerve
NF
Hb9-EGFP
tongue
GFP DAPI
phrenic nerve
NF
Olig2-Cre;Fz3^CKO/+
Olig2-Cre;Fz3^CKO/-
E12.5
A
E11.5
B
early E13.5
C
E11.5
D
A'
B'
C'
D'
R
C
A
B
forelimb
hindlimb
Fz3^CKO/-
Olig2-Cre;Fz3^CKO/-
Fz3^CKO/-
Olig2-Cre;Fz3^CKO/-
E13.5
E
F
G
H
E'
F'
G'
H'
NF dorsal intermediate ventral

Figure 26. Design of the *Fz3*^{CKO} allele, limb innervation in *Wnt1-Cre;Fz3*$^{CKO/-}$ mice, and comparison of dorsal nerve anatomy in forelimbs with various combinations of *Fz3* and *Ret* loss-of-function alleles

(A) Structure of the *Fz3*^{CKO} allele. Top, partial genomic map of the third *Fz3* coding exon. The exon is indicated by a filled rectangle, and cutting sites of endonucleases *EcoR* I and *EcoR* V are shown. Middle, structure of the *Fz3*^{CKO} targeting construct. A HA epitode is inserted to replace the linker region in this exon, which is followed by the *neomycin phosphotransferase* selection marker with two flanking *frp* sites. *LoxP* sites are placed upstream of the third exon and downstream of the *neomycin phosphotransferase* expression cassette, and two *EcoR* I sites are introduced close to *loxP* sites for further Southern blotting. Bottom, map of the allele after homologous recombination and locations of Southern blot hybridization probes.

(B) Genotyping of *WT* and *Fz3*$^{CKO/+}$ mice by Southern blotting with external 5' and 3' probes shown in A after *EcoR* I digestion, the size of genomic fragments generated by *WT* and targeted alleles is indicated.

(C-D') NF immunostaining of whole-mount forelimbs and hindlimbs from E12 *Fz3*$^{CKO/+}$ and *Wnt1-Cre;Fz3*$^{CKO/-}$ embryos, with depth coded by colors. Scale bar, 500 μm.

(E-G') NF immunostaining of whole-mount forelimbs from E13.5 *Fz3*$^{+/-}$*;Ret*$^{+/-}$, *Ret*$^{-/-}$, and *Fz3*$^{-/-}$*;Ret*$^{+/-}$ embryos, with depth coded by colors. E'-G' are magnified view of the boxed regions in E-G. Scale bars: G, 500 μm; G', 100 μm.

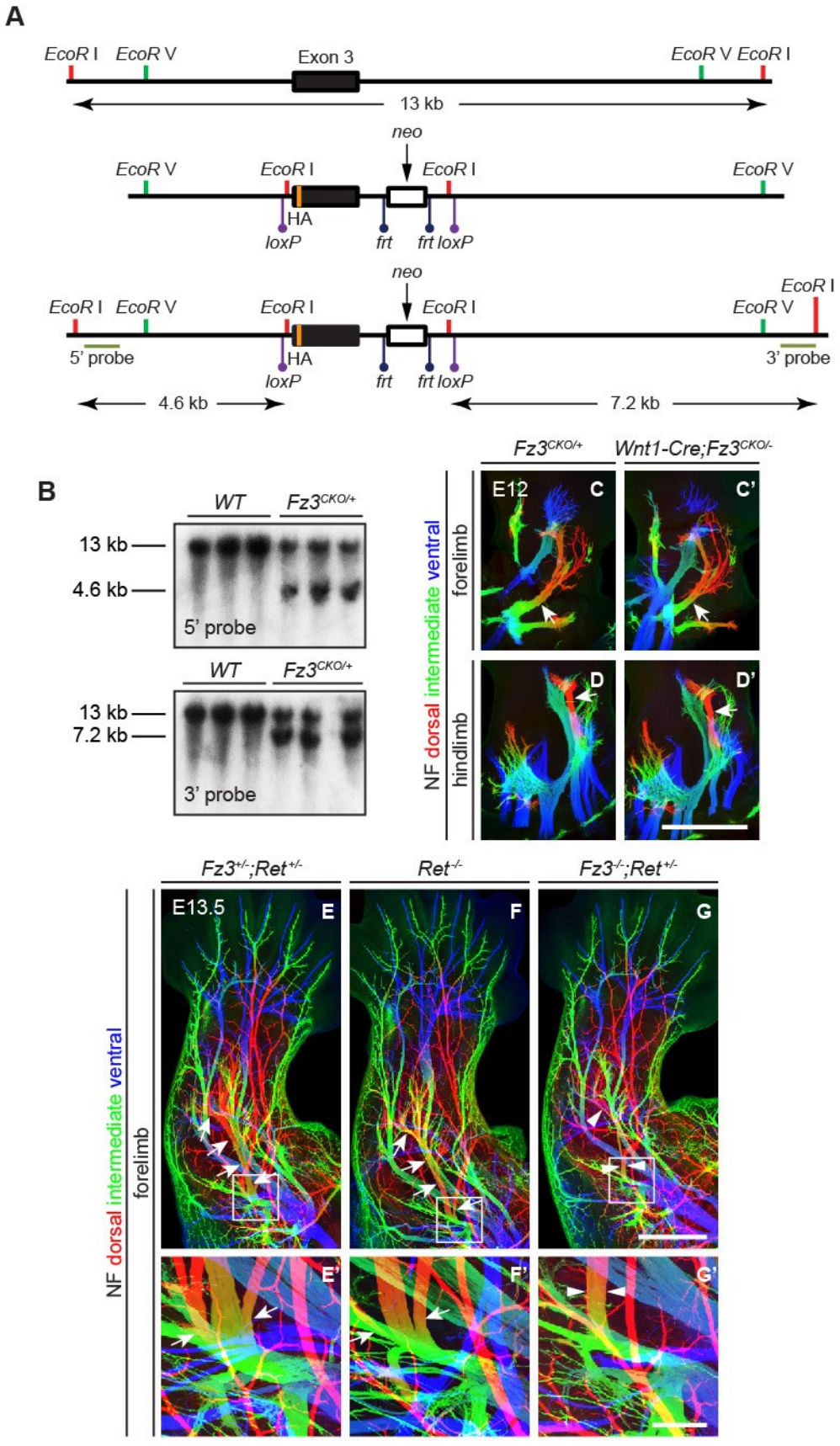
A
EcoR I
EcoR V
Exon 3
EcoR V
EcoR I
13 kb
neo
HA
loxP
frt
frt loxP
5' probe
3' probe
4.6 kb
7.2 kb
B
WT
Fz3CKO/+
13 kb
4.6 kb
5' probe
13 kb
7.2 kb
3' probe
Wnt1-Cre;Fz3CKO/-
E12
C
C'
D
D'
forelimb
hindlimb
NF dorsal intermediate ventral
Fz3+/-;Ret+/-
Ret-/-
Fz3-/-;Ret+/-
E13.5
E
F
G
E'
F'
G'

G. Defective motor innervation in the hindlimb due to *Fz3* knockout leads to muscle atrophy

The early postnatal death of *Fz3*$^{-/-}$ mice has prevented us from analyzing further consequences of defective motor axon growth resulted from loss of *Fz3*. To circumvent this problem, we used the *Cdx1-Cre* transgene to knockout *Fz3* in the caudal half of the mouse with the intention that inactivation of *Fz3* by this transgene might be able to present spinal motor nerve defects shown in *Fz3*$^{-/-}$ mice and meanwhile does not affect mice's postnatal viability (Hierholzer and Kemler, 2009). We found that *Cdx1-Cre;Fz3*$^{CKO/-}$ mice are viable and exhibit abnormally positioned hindlimbs and a curled tail, suggesting *Cdx1-Cre* efficiently recombines the *Fz3*^{CKO} allele during very early embryonic development while the function of *Fz3* critical for survival (i.e. breathing and feeding) is not disrupted (Figure 27A). In *Cdx1-Cre;Fz3*$^{CKO/-}$ mice, the dorsal limb-innervating motor nerves within both forelimbs and hindlimbs completely resemble their counterparts in *Fz3*$^{-/-}$ mice (Figure 27B-E'). *Cdx1-Cre;Fz3*$^{CKO/-}$ mice are able to ambulate in the cage with their forelimbs appearing normal, indicating that the mild thinning of the dorsal nerve in the forelimb does not affect voluntary motor behaviors.

In various mouse models and human motor neuron diseases, such as Amyotrophic Lateral Sclerosis (ALS), degeneration of motor neurons generally results in the atrophy of selective muscles (Hardiman et al., 2011). We therefore asked whether the defective motor innervation of the hindlimb by the peroneal nerve causes atrophy of its muscular targets, and performed magnetic resonance imaging (MRI) of hindlimbs from P70 *Cdx1-Cre;Fz3*$^{CKO/-}$ and *WT* littermates. While muscles in the anterior compartment of the distal

hindlimb, which are targets of dorsal motor nerves, have been normally developed in *Cdx1-Cre;Fz3*$^{CKO/-}$ mice by E15.5, these muscles are completely atrophied in adult mutant mice (Figure 27F-G'). Therefore, defective axon growth in LMC_L motor neurons caused by *Fz3* inactivation leads to muscle atrophy in the anterior compartment of the distal hindlimb.

Figure 27. Selective hindlimb muscle atrophy in response to the failure of motor innervation in *Fz3*$^{-/-}$ mice, and comparison of LMC_L axon guidance and growth defects in various knockout mice

(A) Picture of a P11 *Cdx1-Cre;Fz3*$^{CKO/-}$ mouse with stiff hindlimbs (arrows) and a curled tail (arrow head).

(B-E') NF immunostaining of whole-mount forelimbs and hindlimbs from E12.5 *Fz3*$^{CKO/+}$ and *Cdx1-Cre;Fz3*$^{CKO/-}$ embryos, with depth coded by colors. B'-E' are magnified view of the enclosed box in B-E. Scale bars: E, 500 μm; E', 100 μm.

(F and F') GFP immunostaining with DAPI counter staining of cross sections from E15.5 *Hb9-EGFP;Fz3*$^{CKO/-}$ and *Hb9-EGFP;Cdx1-Cre;Fz3*$^{CKO/-}$ hindlimbs. The anterior compartment musculature (delineated by solid white lines) is extensively innervated in *Hb9-EGFP;Fz3*$^{CKO/-}$ mice, but is not innervated in *Hb9-EGFP;Cdx1-Cre;Fz3*$^{CKO/-}$ mice. F, fibula; T, tibia. Scale bar, 500 μm.

(G and G') Cross-sectional magnetic resonance images of P70 *Cdx1-Cre;Fz3*$^{CKO/+}$ and *Cdx1-Cre;Fz3*$^{CKO/-}$ hindlimbs show nearly complete degeneration and fibrosis of the anterior compartment musculature in the *Cdx1-Cre;Fz3*$^{CKO/-}$ distal hindlimb. The anterior muscle compartment is delimited by a red border. The large and small dark territories are the tibia and fibula, respectively.

(H-J') NF immunostaining of whole-mount hindlimbs from E13.5 *Fz3*$^{+/-}$*;Ret*$^{+/-}$, *Fz3*$^{-/-}$*;Ret*$^{+/-}$, and *Ret*$^{-/-}$ embryos. Boxed regions in H-J are enlarged in H'-J'. In H-J, white arrows and arrowheads indicate the dorsal nerve. Arrow and arrowhead colors in H-J': magenta indicates the dorsal nerve diameter proximal and white indicates the dorsal

nerve diameter distal to the point where axons stall in *Fz3*$^{-/-}$ limbs (asterisks). Depth is color coded. Scale bars: J, 500 μm; J', 100 μm.

(K) Comparison of LMC_L axon growth and guidance defects in different knockout lines. In *Fz3*$^{-/-}$ embryos, many dorsal motor axons fail to grow beyond a proximal branching point, whereas in *EphA4*$^{-/-}$, *Gdnf*$^{-/-}$, and *Ret*$^{-/-}$ embryos, dorsal axons are mis-routed to the ventral limb.

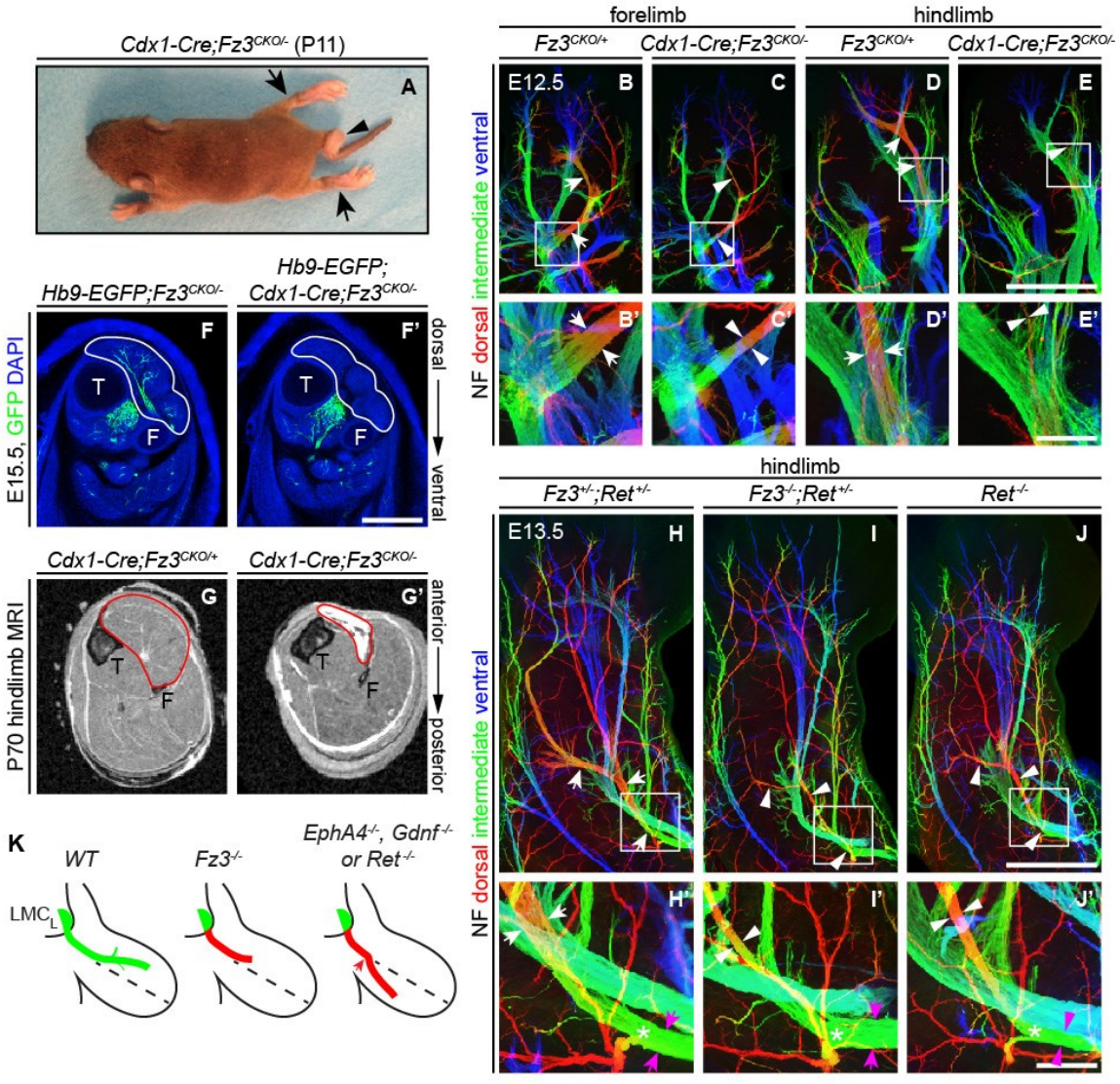

Chapter V: Role of *Fz3* in Neural Crest Cells

By NF immunohistochemistry on whole-mount E11 embryos, Wang et al. (2006b) initially observed a series of discrete NF-rich clusters along the caudal half of the *Fz3*$^{-/-}$ spinal cord that appear to represent ectopic neurons (Figure 28A and A'). Based on the anatomical location of these clusters, we hypothesized that they might arise from local neural crest (NC) cells that had failed to migrate away from the dorsal aspect of the neural tube.

The NC is a transient cell population that undergoes a succession of events guided by a gene regulatory network during embryonic development (Sauka-Spengler and Bronner-Fraser, 2008). The NC is initially induced at the border between future neural and non-neural ectoderm and then resides at the dorsal aspect of the neural tube. Finally NC cells migrate extensively and differentiate into a diverse array of cell and tissue types. To test our hypothesis, we performed immunostaining to address whether cells in these clusters express certain NC lineage-specific transcription factors. For example, *Sox10* expression is detected in migrating NC cells and persists in neurons and melanocytes, and *Brn3a* and *Islet1/2* are expressed in postmigratory DRG sensory neurons (Bhatt et al., 2013; Sauka-Spengler and Bronner-Fraser, 2008). As shown in Figure 28B-C', a large portion of cells in the NF-rich clusters express *Sox10*, *Brn3a*, or *Islet1/2*, indicating they are originally from the NC lineage. Of note, the expression of *Sox10* and *Brn3a* or *Islet1/2* is mutually exclusive, suggesting NC progenitors with migration defects are able to differentiate to committed lineages and such differentiation might be largely dependent

on intrinsic signals. Hence, our *Fz3* knockout mouse is also a uniquely useful model to dissect extrinsic vs. intrinsic influences on NC cell specification.

We further noticed that both the average size and the number of these clusters decrease from E11.5 to E12.5 and they completely disappear ~E14.5. These phenomena suggest cells in these ectopic clusters might undergo programmed cell death. To test this idea, we performed cleaved Caspase3 immunostaining on spinal cord sections containing such clusters. As shown in Figure 28D-F', at E11.5 many cells are apoptotic, and apoptotic cells appear to be mainly more differentiated DRG-like NF^{+}/$Sox10^{-}$ neurons.

Interestingly, there are fewer apoptotic neurons in *Fz3*$^{-/-}$ DRGs at early E11.5 (Figure 28D-E'). In the vertebrate peripheral nervous system (PNS), sensory neurons are generated from NC cells in a number greater than that required for a complete innervation of peripheral targets. Some of them then undergo apoptosis due to the limited amount of target-derived neurotrophic factors, and the final number of sensory neurons that survive is determined by the size of their targets. In the DRGs associated with the caudal half of the *Fz3*$^{-/-}$ spinal cord, it is very likely that initially fewer neurons are present and compete for neurotrophic factors owing to the defective migration of some NC cells, and subsequently fewer neurons are susceptible to apoptosis.

Figure 28. Migration defect of neural crest cells in *Fz3*$^{-/-}$ mice

(A and A') NF-rich clusters along the caudal half of the *Fz3*$^{-/-}$ spinal cord are visualized by NF immunohistochemistry of whole-mount E11 *WT* and *Fz3*$^{-/-}$ embryos. Scale bar, 500 μm.

(B-C'') Expression of NC-lineage transcription factors Islet1/2, Brn3a, and Sox10 in cells within NF-rich clusters is shown by immunostaining of cross sections from E12.5 *Fz3*$^{-/-}$ spinal cords. Scale bars, 100 μm.

(D-F'') Expression of NF, cleaved Caspase3, and Sox10 on cross spinal cord sections is revealed by immunostaining. The boxed region in E, E', and E'' are enlarged in F, F', and F'', respectively. Scale bars: E'', 200 μm; F'', 100 μm.

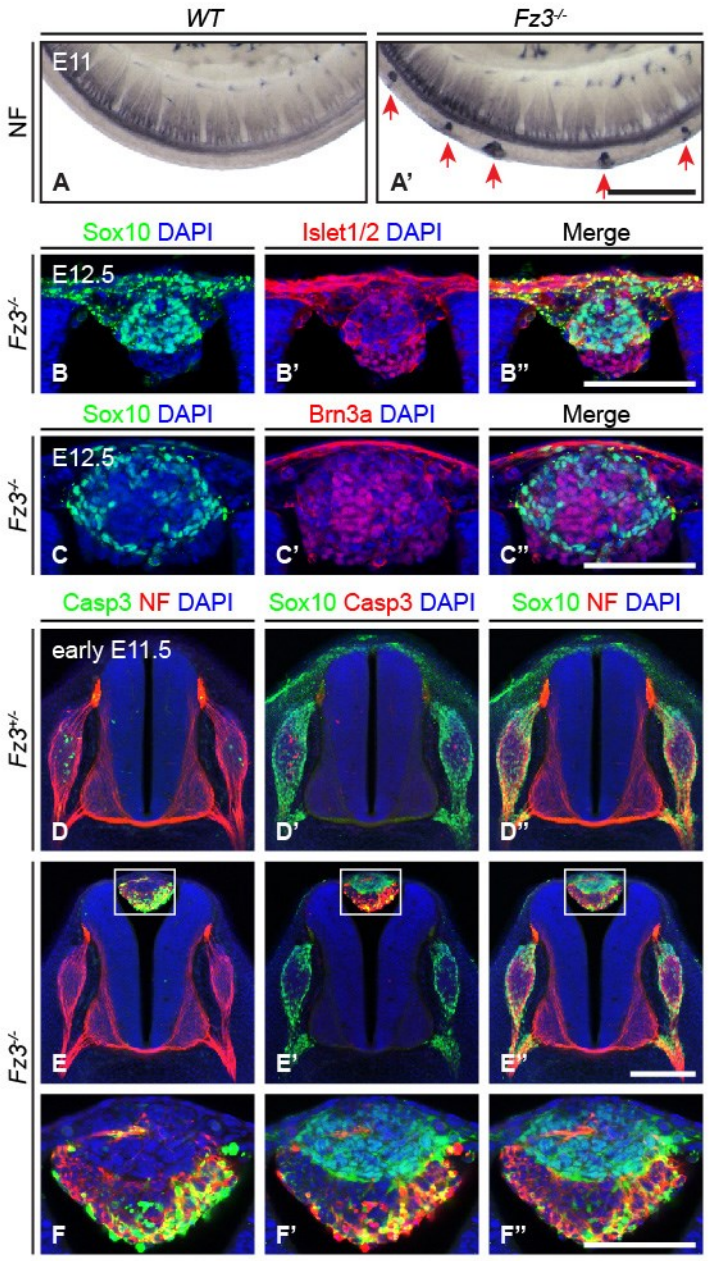
WT
Fz3-/-
NF
E11
A
A'
Sox10 DAPI
Islet1/2 DAPI
Merge
Fz3-/-
E12.5
B
B'
B''
Sox10 DAPI
Brn3a DAPI
Merge
Fz3-/-
E12.5
C
C'
C''
Casp3 NF DAPI
Sox10 Casp3 DAPI
Sox10 NF DAPI
Fz3+/-
early E11.5
D
D'
D''
Fz3-/-
E
E'
E''
F
F'
F''

Chapter VI: Conclusions and Discussion

A. PCP signaling in axon growth and guidance in the mouse nervous system

Although *Fz3* is not detectably expressed in the skin and *Fz3*$^{-/-}$ mice do not exhibit any hair follicle orientation defect, it has been generally accepted that Fz3 functions through the PCP signaling pathway due to the following observations: (1) *Fz6* is a definite PCP gene, and *Fz3* and *Fz6* constitute a distinct branch within the mammalian *Frizzled* family based on their homologous DNA and amino acid sequences (Yu et al., 2010); (2) *Fz3* and *Fz6* are functionally redundant in certain developmental processes, including neural tube closure and the orientation of stereociliary bundles in inner ear sensory hair cells (Wang et al., 2006a); and (3) mice that are missing other canonical PCP genes, such as *Celsr2* and *Celsr3*, exhibit nearly identical *Fz3*$^{-/-}$ phenotypes in the nervous system, including axon guidance defects in major fiber tracts in the rostral brain (Tissir et al., 2005), migration defects in the VIIth cranial motor neurons (Qu et al., 2010), and defects in the anterior-posterior organization of monoaminergic axons in the brainstem (Fenstermaker et al., 2010).

By taking advantage of various genetic and immunohistochemical approaches, we systematically explored *Fz3*$^{-/-}$ phenotypes in the nervous system and found that *Fz3* is required for axon guidance of several fiber tracts in the CNS and axon growth of distinct motor neuron populations. In the CNS, loss of *Fz3* results in major axon tracts following aberrant trajectories. For example, commissural sensory axons in the spinal cord fail to turn rostrally after midline crossing (Lyuksyutova et al., 2003) and innervate the brain, thalamocortical axons form an intra-thalamic U-shaped fiber tract and fail to enter the

internal capsule, dopaminergic and serotonergic axons in the brain form tight fasciculi descending to the spinal cord and fail to ascend to the forebrain. The mis-routing of these axon tracts clearly indicates a role of Fz3 in controlling axon guidance. On the other hand, in peripheral motor nerves, *Fz3* loss-of-function leads to stalling of motor axons at specific loci. For example, in *Fz3*$^{-/-}$ embryos, the XIIth nerve is markedly thinned immediately after making a rostral turn toward the tongue, and dorsal limb motor nerves become thinned after they branch in the nerve plexus at the base of limbs, suggesting axons in these nerves are unable to grow beyond certain stalling points (Hua et al., 2013).

Of note is that the *Fz3* loss-of-function mutations produces phenotypes in distinct populations of cranial and spinal motor neurons. In contrast, *Fz3* is widely expressed in the mouse CNS (Wang et al., 2002). The lack of a phenotype in other motor neuron populations in *Fz3*$^{-/-}$ mice can be potentially explained by several possibilities: (1) activated Fz3 signaling is not required for the normal development of these motor neurons; (2) one or more components in the Fz3 signaling pathway are not present and therefore Fz3 signaling is inactive in these motor neurons, although *Fz3* is expressed; and (3) other Frizzled receptors play redundant roles with Fz3. In the future, it would be interesting to test these possibilities.

Although *Fz3*$^{-/-}$ phenotypes have been extensively examined in this study, there are still many open questions awaiting future research. These include but are not limited to: (1) does *Fz3* loss-of-function affect lamination patterns and circuits in the spinal cord? (2) does the loss of ascending spinal sensory tracts impact brain development? (3)

reciprocally, does the loss of descending corticospinal tract affect spinal cord development and functions? (4) does *Fz3* inactivation affect the innervation of the suprachiasmatic nucleus, which controls circadian rhythms? (5) does *Fz3* knockout affect midline-crossing commissures located at the level of the pre-Bötzinger complex, which paces inspirations? and (6) does *Fz3* play any role in the migration of newly generated neurons in the subventricular zone in adult mice? While it remains technically challenging to unambiguously label distinct neuronal populations and their axons, addressing the above questions will shed new light on the role of PCP signaling in mouse neural development.

B. Autonomous and non-autonomous roles of Fz3 signaling in axon growth and guidance

The elimination of *Fz3* expression by the *Olig2-Cre* in *Olig2-Cre;Fz3*$^{CKO/-}$ embryos produces the full spectrum of *Fz3*$^{-/-}$ defects in the motor system, together with the absence of similar phenotypes in *Wnt1-Cre;Fz3*$^{CKO/-}$ mice, indicating that Fz3 functions autonomously in motor neurons to control axon growth. In addition, Fz3 is also autonomously required in a subset of RGCs for the inferior fasciculus of the accessory optic tract to innervate the MTN.

In the brain, ablation of *Fz3* expression in the cerebral cortex by *Emx1-IRES-Cre* or in the dorsal thalamus by *RORα-IRES-Cre* does not affect the entry of cortical and thalamic axons into the internal capsule. Although the inability of these *Cre* lines to produce any obvious phenotype can be potentially explained if *Cre* expression is

relatively late and/or at low level, axon guidance defects observed in *Dlx5/6-Cre;Fz3*$^{CKO/-}$ mice clearly demonstrate that *Fz3* expression is required in ventral telencephalic neurons for the guidance of cortical and thalamic axons and further suggest that Fz3 is most likely not autonomously required in cortical pyramidal and dorsal thalamic neurons.

While the autonomous requirement of Fz3 signaling in motor neurons is relatively comprehensible from the aspect of classic axon guidance and growth mechanisms, the role of Fz3 in ventral telencephalic neurons in guiding cortical and thalamic axons is intriguing. We have shown that *Fz3* loss-of-function affects the distribution of corridor cells in the striatum. However, it is not known whether the aberrant localization of corridor cells is irrelevant to, is a consequence of, or plays a causal role in the mis-routing of thalamocortical axons. In addition, while it is not likely that *Fz3* inactivation affects neuronal specification, it is still largely unexplored whether in the *Fz3*$^{-/-}$ ventral telencephalon, the migration and distribution of other neuron populations are similarly affected as these corridor cells. On the other hand, other than neuronal migration and distribution, it is also not known whether *Fz3* controls axonal development of ventral telencephalic neurons, which may or may not further play a role in the guidance of cortical and thalamic axons.

C. A novel aspect of motor axon growth controlled by PCP signaling

LMC motor neurons constitute a wonderful system for studying axon guidance partly because of the development of whole-mount limb immunostaining techniques, which can unambiguously reveal individual nerves and meanwhile make forward genetic

screenings less labor-intensive. It has been shown that several signaling pathways participate in the navigation of motor axons into the limb. For example, loss-of-function mutations in *Sema3F*, *Npn2*, *ephrin-B2*, and *EphB1* result in mis-routing of ventral axons to the dorsal limb, while mutations in *EphA*, *Gdnf*, and *Ret* lead to mis-routing of dorsal axons to the ventral limb (Bonanomi and Pfaff, 2010).

To compare one example of this class of mutants side-by-side with $Fz3^{-/-}$ and to examine the possibility of a genetic interaction between the Fz3 and the GDNF/Ret signaling pathways, we examined limb innervation phenotypes in $Ret^{-/-}$, $Fz3^{+/-};Ret^{+/-}$, and $Fz3^{-/-};Ret^{+/-}$ embryos (Figure 27H-J'). This analysis provides no evidence for a genetic interaction between *Fz3* and *Ret*, as $Fz3^{+/-};Ret^{+/-}$ hindlimb innervation is indistinguishable from *WT*, and $Fz3^{-/-};Ret^{+/-}$ hindlimb innervation is indistinguishable from $Fz3^{-/-}$. Our analysis of $Ret^{-/-}$ forelimb and hindlimb innervation fully confirms previous descriptions (Kramer et al., 2006) and shows that in $Ret^{-/-}$ hindlimbs the dorsal nerve is thinned to a similar extent both proximal and distal to the point at which $Fz3^{-/-}$ dorsal motor axons stall (asterisks in Figure 27H'-J') and the ventral nerve is thicker than its counterpart in *WT* littermates, consistent with a re-routing of dorsal motor axons to the ventral nerve. These experiments confirm that the $Fz3^{-/-}$ dorsal motor axon phenotype is anatomically distinct from the phenotypes described in $EphA4^{-/-}$, $Gdnf^{-/-}$, and $Ret^{-/-}$ limbs (Figure 27K). Therefore, our study here reveals a novel aspect of motor axon growth controlled by PCP signaling. In the future, it would be interesting to apply forward genetic screens to identify novel components in this developmental process.

D. Molecular mechanism underlying PCP signaling in the nervous system

As noted in Chapter I, it is generally believed that the asymmetric localization of PCP proteins establishes and maintains the planar polarity across the epithelial sheet. At the junctions between adjacent cells, the large cadherin-containing Stan/Fmi/Celsr proteins accumulate at the plasma membranes of both cells and are presumed to form homophilic adhesive interactions. By contrast, Frizzled proteins accumulate at the plasma membrane of one cell and Vang/Stan/Vangl proteins accumulate at the plasma membrane of the opposing cell. This model appears well suited to explain how polarity information is transmitted within the relatively stable epithelial system.

However, it appears that such a conceptual framework can hardly be applied to axon growth and guidance. In developing neurons, the well-defined anterior-posterior or proximal-distal axis in the skin does not apply. In the context of axon growth and guidance, PCP signaling is believed to be active at growth cones (Zou, 2012). It has been suggested that Fz3 undergoes Wnt5a-mediated endocytosis at filopodia tips (Onishi et al., 2013). While such Wnt5a/ligand-Fz3/receptor interaction appears sound from the aspect of classic axon guidance mechanisms to explain axonal development defects in PCP mutants, *Wnt5a*$^{-/-}$ embryos do not exhibit the *Fz3*$^{-/-}$ phenotypes (our unpublished data).

Moreover, the dynamic nature of axon growth and guidance imposes challenges for studying the molecular mechanism underlying PCP signaling in these scenarios. First, it is technically challenging to establish an *in vitro* system to specifically recapitulate the unique *in vivo* PCP phenotypes. Second, our work demonstrates essential roles of *Fz3* in

axon growth and guidance, which are related yet different events – defects in the former results in axon stalling and defects in the later leads to axon mis-routing. It is not known whether defects in these two events in *Fz3*$^{-/-}$ embryos reflect different mechanisms at the molecular level employed by Fz3 or different *in vivo* environment encountered by Fz3 signaling. Last but not least, so far the subcellular location of endogenous PCP proteins in developing neurons has not been determined. Although Fz3 and Celsr3 are believed to function in the same pathway to control axon growth in distinct motor nerves and axon guidance in multiple CNS fiber tracts, the potential interaction between Fz3 and Celsr3 – in the way that their paralogs, Fz6 and Celsr1, respectively, interacts (Devenport and Fuchs, 2008) – has not been investigated at all. If Fz3 and Celsr3 do interact with each other, then how do such interactions engage with potential extracellular cues to control axon growth and guidance?

The work presented here has explored an important component of PCP signaling, Fz3, in the development of the mouse nervous system. On the one hand, this body of work adopted, improved, and developed various methods to study axon growth and guidance, and these methods are very valuable to the developmental neuroscience field. On the other hand, the role of *Fz3*, as revealed here, also sheds light on the molecular mechanism underlying PCP signaling in the mouse nervous system. First, *Fz3*$^{-/-}$ and *Celsr*$^{-/-}$ mice exhibit essentially identical axon guidance defects in multiple fiber tracts in the brain and axon growth defects in the peroneal nerve in the hindlimb [Hua et al. (2013); Tissir et al. (2005); Wang et al. (2002); and unpublished data from Fadel Tissir, André Goffinet and colleagues], suggesting PCP signaling is largely unified in the skin and the

nervous system from the aspect of employing similar PCP components. Second, it has been suggested that *Vangl1* and *Vangl2* – core PCP genes in the epithelial system – are not required for the same aspects controlled by *Fz3* and *Celsr3* in the brain and hindlimb (unpublished data from Fadel Tissir, André Goffinet and colleagues). In addition, while Fz3 and Fz6 likely act in a conserved manner in different contexts, they are not completely functionally equivalent (our unpublished data). Taken together, these data suggest that PCP signaling in the nervous system might be slightly different from that in the epithelial system in terms of employing different components and quantitatively activating downstream effectors. Last but not least, loss of *Linx*, which is a member of the leucine-rich repeat and immunoglobulin family and encodes a transmembrane protein, exhibits nearly identical phenotypes in the brain and the motor system [Mandai et al. (2009), and our unpublished data], indicating that Linx might function with Fz3 and Celsr3 in the same pathway. In the future, it would be of great interest for neuroscientists to tackle how PCP signaling controls axon growth and guidance at the molecular level.

References

Abbott, L.C., and Jacobowitz, D.M. (1999). Developmental expression of calretinin-immunoreactivity in the thalamic eminence of the fetal mouse. Int J Dev Neurosci *17*, 331-345.

Abraira, V.E., and Ginty, D.D. (2013). The sensory neurons of touch. Neuron *79*, 618-639.

Allan, D.W., and Greer, J.J. (1997). Development of phrenic motoneuron morphology in the fetal rat. J Comp Neurol *382*, 469-479.

Araujo, S.J., and Tear, G. (2003). Axon guidance mechanisms and molecules: lessons from invertebrates. Nat Rev Neurosci *4*, 910-922.

Arber, S., Han, B., Mendelsohn, M., Smith, M., Jessell, T.M., and Sockanathan, S. (1999). Requirement for the homeobox gene Hb9 in the consolidation of motor neuron identity. Neuron *23*, 659-674.

Armstrong, A., Ryu, Y.K., Chieco, D., and Kuruvilla, R. (2011). Frizzled3 is required for neurogenesis and target innervation during sympathetic nervous system development. J Neurosci *31*, 2371-2381.

Badea, T.C., Cahill, H., Ecker, J., Hattar, S., and Nathans, J. (2009a). Distinct roles of transcription factors brn3a and brn3b in controlling the development, morphology, and function of retinal ganglion cells. Neuron *61*, 852-864.

Badea, T.C., Hua, Z.L., Smallwood, P.M., Williams, J., Rotolo, T., Ye, X., and Nathans, J. (2009b). New mouse lines for the analysis of neuronal morphology using CreER(T)/loxP-directed sparse labeling. PLoS One *4*, e7859.

Badea, T.C., Wang, Y., and Nathans, J. (2003). A noninvasive genetic/pharmacologic strategy for visualizing cell morphology and clonal relationships in the mouse. J Neurosci *23*, 2314-2322.

Bashaw, G.J., and Klein, R. (2010). Signaling from axon guidance receptors. Cold Spring Harb Perspect Biol *2*, a001941.

Bhatt, S., Diaz, R., and Trainor, P.A. (2013). Signals and switches in Mammalian neural crest cell differentiation. Cold Spring Harb Perspect Biol *5*, a008326.

Bonanomi, D., Chivatakarn, O., Bai, G., Abdesselem, H., Lettieri, K., Marquardt, T., Pierchala, B.A., and Pfaff, S.L. (2012). Ret is a multifunctional coreceptor that integrates diffusible- and contact-axon guidance signals. Cell *148*, 568-582.

Bonanomi, D., and Pfaff, S.L. (2010). Motor axon pathfinding. Cold Spring Harb Perspect Biol *2*, a001735.

Burgess, R.W., Jucius, T.J., and Ackerman, S.L. (2006). Motor axon guidance of the mammalian trochlear and phrenic nerves: dependence on the netrin receptor Unc5c and modifier loci. J Neurosci *26*, 5756-5766.

Chang, H., and Nathans, J. (2013). Responses of hair follicle-associated structures to loss of planar cell polarity signaling. Proc Natl Acad Sci U S A *110*, E908-917.

Chedotal, A., and Richards, L.J. (2010). Wiring the brain: the biology of neuronal guidance. Cold Spring Harb Perspect Biol *2*, a001917.

Chisholm, A., and Tessier-Lavigne, M. (1999). Conservation and divergence of axon guidance mechanisms. Curr Opin Neurobiol *9*, 603-615.

Danielian, P.S., Muccino, D., Rowitch, D.H., Michael, S.K., and McMahon, A.P. (1998). Modification of gene activity in mouse embryos in utero by a tamoxifen-inducible form of Cre recombinase. Curr Biol *8*, 1323-1326.

De Marco Garcia, N.V., and Jessell, T.M. (2008). Early motor neuron pool identity and muscle nerve trajectory defined by postmitotic restrictions in Nkx6.1 activity. Neuron *57*, 217-231.

Dessaud, E., Yang, L.L., Hill, K., Cox, B., Ulloa, F., Ribeiro, A., Mynett, A., Novitch, B.G., and Briscoe, J. (2007). Interpretation of the sonic hedgehog morphogen gradient by a temporal adaptation mechanism. Nature *450*, 717-720.

Devenport, D., and Fuchs, E. (2008). Planar polarization in embryonic epidermis orchestrates global asymmetric morphogenesis of hair follicles. Nat Cell Biol *10*, 1257-1268.

Dickson, B.J. (2002). Molecular mechanisms of axon guidance. Science *298*, 1959-1964.

Eng, S.R., Gratwick, K., Rhee, J.M., Fedtsova, N., Gan, L., and Turner, E.E. (2001). Defects in sensory axon growth precede neuronal death in Brn3a-deficient mice. J Neurosci *21*, 541-549.

Fenstermaker, A.G., Prasad, A.A., Bechara, A., Adolfs, Y., Tissir, F., Goffinet, A., Zou, Y., and Pasterkamp, R.J. (2010). Wnt/planar cell polarity signaling controls the anterior-posterior organization of monoaminergic axons in the brainstem. J Neurosci *30*, 16053-16064.

Furuta, Y., Lagutin, O., Hogan, B.L., and Oliver, G.C. (2000). Retina- and ventral forebrain-specific Cre recombinase activity in transgenic mice. Genesis *26*, 130-132.

Goodrich, L.V., and Strutt, D. (2011). Principles of planar polarity in animal development. Development *138*, 1877-1892.

Gorski, J.A., Talley, T., Qiu, M., Puelles, L., Rubenstein, J.L., and Jones, K.R. (2002). Cortical excitatory neurons and glia, but not GABAergic neurons, are produced in the Emx1-expressing lineage. J Neurosci *22*, 6309-6314.

Gubb, D., and Garcia-Bellido, A. (1982). A genetic analysis of the determination of cuticular polarity during development in Drosophila melanogaster. J Embryol Exp Morphol *68*, 37-57.

Guo, N., Hawkins, C., and Nathans, J. (2004). Frizzled6 controls hair patterning in mice. Proc Natl Acad Sci U S A *101*, 9277-9281.

Guthrie, S. (2007). Patterning and axon guidance of cranial motor neurons. Nat Rev Neurosci *8*, 859-871.

Hardiman, O., van den Berg, L.H., and Kiernan, M.C. (2011). Clinical diagnosis and management of amyotrophic lateral sclerosis. Nat Rev Neurol *7*, 639-649.

Hayashi, S., and McMahon, A.P. (2002). Efficient recombination in diverse tissues by a tamoxifen-inducible form of Cre: a tool for temporally regulated gene activation/inactivation in the mouse. Dev Biol *244*, 305-318.

Hebert, J.M., and McConnell, S.K. (2000). Targeting of cre to the Foxg1 (BF-1) locus mediates loxP recombination in the telencephalon and other developing head structures. Dev Biol *222*, 296-306.

Hedgecock, E.M., Culotti, J.G., and Hall, D.H. (1990). The unc-5, unc-6, and unc-40 genes guide circumferential migrations of pioneer axons and mesodermal cells on the epidermis in C. elegans. Neuron *4*, 61-85.

Hierholzer, A., and Kemler, R. (2009). Cdx1::Cre allele for gene analysis in the extraembryonic ectoderm and the three germ layers of mice at mid-gastrulation. Genesis *47*, 204-209.

Hua, Z.L., Smallwood, P.M., and Nathans, J. (2013). Frizzled3 controls axonal development in distinct populations of cranial and spinal motor neurons. eLife *2*, e01482.

Huang, S.M., Li, X., Yu, Y., Wang, J., and Caterina, M.J. (2011). TRPV3 and TRPV4 ion channels are not major contributors to mouse heat sensation. Mol Pain *7*, 37.

Huettl, R.E., and Huber, A.B. (2011). Cranial nerve fasciculation and Schwann cell migration are impaired after loss of Npn-1. Dev Biol *359*, 230-241.

Ishii, N., Wadsworth, W.G., Stern, B.D., Culotti, J.G., and Hedgecock, E.M. (1992). UNC-6, a laminin-related protein, guides cell and pioneer axon migrations in C. elegans. Neuron *9*, 873-881.

Jacobowitz, D.M., and Abbott, L.C. (1998). Chemoarchitectonic atlas of the developing mouse brain (Boca Raton: CRC Press).

Kandel, E.R., Schwartz, J.H., and Jessell, T.M. (2000). Principles of neural science, 4th edn (McGraw-Hill).

Knudson, C.M., Tung, K.S., Tourtellotte, W.G., Brown, G.A., and Korsmeyer, S.J. (1995). Bax-deficient mice with lymphoid hyperplasia and male germ cell death. Science *270*, 96-99.

Kramer, E.R., Knott, L., Su, F., Dessaud, E., Krull, C.E., Helmbacher, F., and Klein, R. (2006). Cooperation between GDNF/Ret and ephrinA/EphA4 signals for motor-axon pathway selection in the limb. Neuron *50*, 35-47.

Lieberam, I., Agalliu, D., Nagasawa, T., Ericson, J., and Jessell, T.M. (2005). A Cxcl12-CXCR4 chemokine signaling pathway defines the initial trajectory of mammalian motor axons. Neuron *47*, 667-679.

Logan, C.Y., and Nusse, R. (2004). The Wnt signaling pathway in development and disease. Annu Rev Cell Dev Biol *20*, 781-810.

Lopez-Bendito, G., Cautinat, A., Sanchez, J.A., Bielle, F., Flames, N., Garratt, A.N., Talmage, D.A., Role, L.W., Charnay, P., Marin, O.*, et al.* (2006). Tangential neuronal migration controls axon guidance: a role for neuregulin-1 in thalamocortical axon navigation. Cell *125*, 127-142.

Lopez-Bendito, G., and Molnar, Z. (2003). Thalamocortical development: how are we going to get there? Nat Rev Neurosci *4*, 276-289.

Lyuksyutova, A.I., Lu, C.C., Milanesio, N., King, L.A., Guo, N., Wang, Y., Nathans, J., Tessier-Lavigne, M., and Zou, Y. (2003). Anterior-posterior guidance of commissural axons by Wnt-frizzled signaling. Science *302*, 1984-1988.

Mandai, K., Guo, T., St Hillaire, C., Meabon, J.S., Kanning, K.C., Bothwell, M., and Ginty, D.D. (2009). LIG family receptor tyrosine kinase-associated proteins modulate growth factor signals during neural development. Neuron *63*, 614-627.

Marquardt, T., Ashery-Padan, R., Andrejewski, N., Scardigli, R., Guillemot, F., and Gruss, P. (2001). Pax6 is required for the multipotent state of retinal progenitor cells. Cell *105*, 43-55.

Metin, C., and Godement, P. (1996). The ganglionic eminence may be an intermediate target for corticofugal and thalamocortical axons. J Neurosci *16*, 3219-3235.

Molnar, Z., Garel, S., Lopez-Bendito, G., Maness, P., and Price, D.J. (2012). Mechanisms controlling the guidance of thalamocortical axons through the embryonic forebrain. Eur J Neurosci *35*, 1573-1585.

Nakagawa, Y., and O'Leary, D.D. (2003). Dynamic patterned expression of orphan nuclear receptor genes RORalpha and RORbeta in developing mouse forebrain. Dev Neurosci *25*, 234-244.

NIH Neuroscience Blueprint Cre Driver Network (2009). Cre recombinase-expressing mice generated for the NIH Neuroscience Blueprint Cre Driver Network. MGI Direct Data Submission.

Nusse, R., and Varmus, H.E. (1992). Wnt genes. Cell *69*, 1073-1087.

Onishi, K., Shafer, B., Lo, C., Tissir, F., Goffinet, A.M., and Zou, Y. (2013). Antagonistic functions of Dishevelleds regulate Frizzled3 endocytosis via filopodia tips in Wnt-mediated growth cone guidance. J Neurosci *33*, 19071-19085.

Oppenheim, R.W., Houenou, L.J., Parsadanian, A.S., Prevette, D., Snider, W.D., and Shen, L. (2000). Glial cell line-derived neurotrophic factor and developing mammalian motoneurons: regulation of programmed cell death among motoneuron subtypes. J Neurosci *20*, 5001-5011.

Qu, Y., Glasco, D.M., Zhou, L., Sawant, A., Ravni, A., Fritzsch, B., Damrau, C., Murdoch, J.N., Evans, S., Pfaff, S.L.*, et al.* (2010). Atypical cadherins Celsr1-3 differentially regulate migration of facial branchiomotor neurons in mice. J Neurosci *30*, 9392-9401.

Rodriguez, C.I., Buchholz, F., Galloway, J., Sequerra, R., Kasper, J., Ayala, R., Stewart, A.F., and Dymecki, S.M. (2000). High-efficiency deleter mice show that FLPe is an alternative to Cre-loxP. Nat Genet *25*, 139-140.

Sakhalkar, H.S., Dewhirst, M., Oliver, T., Cao, Y., and Oldham, M. (2007). Functional imaging in bulk tissue specimens using optical emission tomography: fluorescence preservation during optical clearing. Phys Med Biol *52*, 2035-2054.

Sasselli, V., Boesmans, W., Vanden Berghe, P., Tissir, F., Goffinet, A.M., and Pachnis, V. (2013). Planar cell polarity genes control the connectivity of enteric neurons. J Clin Invest *123*, 1763-1772.

Sauka-Spengler, T., and Bronner-Fraser, M. (2008). A gene regulatory network orchestrates neural crest formation. Nat Rev Mol Cell Biol *9*, 557-568.

Schambra, U.B., Sulik, K.K., Petrusz, P., and Lauder, J.M. (1989). Ontogeny of cholinergic neurons in the mouse forebrain. J Comp Neurol *288*, 101-122.

Serafini, T., Colamarino, S.A., Leonardo, E.D., Wang, H., Beddington, R., Skarnes, W.C., and Tessier-Lavigne, M. (1996). Netrin-1 is required for commissural axon guidance in the developing vertebrate nervous system. Cell *87*, 1001-1014.

Song, M.R., Shirasaki, R., Cai, C.L., Ruiz, E.C., Evans, S.M., Lee, S.K., and Pfaff, S.L. (2006). T-Box transcription factor Tbx20 regulates a genetic program for cranial motor neuron cell body migration. Development *133*, 4945-4955.

Stenman, J., Toresson, H., and Campbell, K. (2003). Identification of two distinct progenitor populations in the lateral ganglionic eminence: implications for striatal and olfactory bulb neurogenesis. J Neurosci *23*, 167-174.

Taniguchi, H., He, M., Wu, P., Kim, S., Paik, R., Sugino, K., Kvitsiani, D., Fu, Y., Lu, J., Lin, Y.*, et al.* (2011). A resource of Cre driver lines for genetic targeting of GABAergic neurons in cerebral cortex. Neuron *71*, 995-1013.

Tissir, F., Bar, I., Jossin, Y., De Backer, O., and Goffinet, A.M. (2005). Protocadherin Celsr3 is crucial in axonal tract development. Nat Neurosci *8*, 451-457.

Vladar, E.K., Bayly, R.D., Sangoram, A.M., Scott, M.P., and Axelrod, J.D. (2012). Microtubules enable the planar cell polarity of airway cilia. Curr Biol *22*, 2203-2212.

Wang, Y., Guo, N., and Nathans, J. (2006a). The role of Frizzled3 and Frizzled6 in neural tube closure and in the planar polarity of inner-ear sensory hair cells. J Neurosci *26*, 2147-2156.

Wang, Y., Macke, J.P., Abella, B.S., Andreasson, K., Worley, P., Gilbert, D.J., Copeland, N.G., Jenkins, N.A., and Nathans, J. (1996). A large family of putative transmembrane receptors homologous to the product of the Drosophila tissue polarity gene frizzled. The Journal of biological chemistry *271*, 4468-4476.

Wang, Y., Thekdi, N., Smallwood, P.M., Macke, J.P., and Nathans, J. (2002). Frizzled-3 is required for the development of major fiber tracts in the rostral CNS. J Neurosci *22*, 8563-8573.

Wang, Y., Zhang, J., Mori, S., and Nathans, J. (2006b). Axonal growth and guidance defects in Frizzled3 knock-out mice: a comparison of diffusion tensor magnetic resonance imaging, neurofilament staining, and genetically directed cell labeling. J Neurosci *26*, 355-364.

White, F.A., Keller-Peck, C.R., Knudson, C.M., Korsmeyer, S.J., and Snider, W.D. (1998). Widespread elimination of naturally occurring neuronal death in Bax-deficient mice. J Neurosci *18*, 1428-1439.

Wichterle, H., Lieberam, I., Porter, J.A., and Jessell, T.M. (2002). Directed differentiation of embryonic stem cells into motor neurons. Cell *110*, 385-397.

Woolf, N.J. (1991). Cholinergic systems in mammalian brain and spinal cord. Prog Neurobiol *37*, 475-524.

Wu, C.S., Zhu, J., Wager-Miller, J., Wang, S., O'Leary, D., Monory, K., Lutz, B., Mackie, K., and Lu, H.C. (2010). Requirement of cannabinoid CB(1) receptors in cortical pyramidal neurons for appropriate development of corticothalamic and thalamocortical projections. Eur J Neurosci *32*, 693-706.

Yu, H., Smallwood, P.M., Wang, Y., Vidaltamayo, R., Reed, R., and Nathans, J. (2010). Frizzled 1 and frizzled 2 genes function in palate, ventricular septum and neural tube closure: general implications for tissue fusion processes. Development *137*, 3707-3717.

Zhang, J., Zhang, G., Morrison, B., Mori, S., and Sheikh, K.A. (2008). Magnetic resonance imaging of mouse skeletal muscle to measure denervation atrophy. Exp Neurol *212*, 448-457.

Zhuang, X., Masson, J., Gingrich, J.A., Rayport, S., and Hen, R. (2005). Targeted gene expression in dopamine and serotonin neurons of the mouse brain. J Neurosci Methods *143*, 27-32.

Zou, Y. (2012). Does planar cell polarity signaling steer growth cones? Curr Top Dev Biol *101*, 141-160.

Curriculum Vitae

The Johns Hopkins University School of Medicine

Zhong L. Hua May 5, 2014

EDUCATIONAL HISTORY

Ph.D. expected	2014	Biochemistry, Cellular and Molecular Biology The Johns Hopkins University School of Medicine	
M.S.	2007	Cell Biology	Tsinghua University
B.S.	2004	Biotechnology	Wuhan University

HONORS AND AWARDS

2006	*Fushikang* Award for Outstanding Scientific Research Graduate School at Shenzhen, Tsinghua University
2005	Award for Outstanding Scientific Research Graduate School at Shenzhen, Tsinghua University
2004	Excellent Undergraduate Thesis of the Year Wuhan University
2003	National Scholarship Wuhan University Ministry of Education of the People's Republic of China
2002, 2001	Excellent Student of the Year Wuhan University
2002, 2001	*Renmin* Scholarship Wuhan University
2000	Scholarship for Freshman Wuhan University

PUBLICATIONS

Hua ZL, Jeon S, Caterina M, Nathans J (2014) *Frizzled3* is required for the development of multiple axon tracts in the mouse central nervous system. *Proceedings of the National Academy of Science USA*. In press.

Hua ZL*, Chang H*, Wang Y, Smallwood PM, Nathans J (2014) Partial interchangeability of *Frizzled3* and *Frizzled6* in tissue polarity signaling for epithelial orientation and axon growth and guidance. Under revision at *Development*. * equal contribution.

Hua ZL, Smallwood PM, Nathans J (2013) *Frizzled3* controls axonal development in distinct populations of cranial and spinal motor neurons. *eLife* **2**:e01482. PMCID: PMC3865743.

Badea TC, **Hua ZL**, Smallwood PM, Williams J, Rotolo T, Ye X, Nathans J (2009) New mouse lines for the analysis of neuronal morphology using CreER(T)/loxP-directed sparse labeling. *PLoS ONE* **4**:e7859. PMCID: PMC2775668.

Ye W, Lv Q, Wong C, Hu S, Fu C, **Hua Z**, Cai G, Li G, Yang BB, Zhang Y (2008) The effect of central loops in miRNA:MRE duplexes on the efficiency of miRNA-mediated gene regulation. *PLoS ONE* **3**:e1719. PMCID: PMC2248708.

Chen S, Gao G, Chen W, Lv Q, Tang S, **Hua Z**, Ye W, Gu D, Wang S, Zhang Y (2008) VEGF-specific siRNAs modified with 2'-deoxy effectively suppress VEGF expression and inhibit growth of nasopharyngeal carcinoma xenograft in a mouse model. *Science in China Series C: Life Sciences* **51**:104-10.

Gu D, Yu B, Zhao C, Ye W, Lv Q, **Hua Z**, Ma J, Zhang Y (2007) The effect of pleiotrophin signaling on adipogenesis. *FEBS Letters* **581**:382-8.

Hua Z*, Lv Q*, Ye W*, Wong C, Cai G, Gu D, Ji Y, Zhao C, Wang J, Yang BB, Zhang Y (2006) MiRNA-directed regulation of VEGF and other angiogenic factors under hypoxia. *PLoS ONE* **1**:e116. * equal contribution. PMCID: PMC1762435.

Chen X, Xu J, **Hua Z**, Huang T, Sun P (2004) Elementary investigation of East Lake on its microbial contamination. *Amino Acids & Biotic Resources* **26**:16-9.